Linear and nonlinear dynamics in stratified shear flows

Jeremy Peter Parker

Supervisor: Prof C. P. Caulfield

Advisor: Prof R. R. Kerswell

Department of Applied Mathematics and Theoretical Physics
University of Cambridge

This dissertation is submitted for the degree of
Doctor of Philosophy

Churchill College September 2020

To Poppy and Mister Ted.

Declaration

I hereby declare that except where specific reference is made to the work of others, the contents of this dissertation are original and have not been submitted in whole or in part for consideration for any other degree or qualification in this, or any other university. This dissertation is my own work and contains nothing which is the outcome of work done in collaboration with others, except as specified in the text and Acknowledgements.

Jeremy Peter Parker
September 2020

Acknowledgements

Academically speaking, I would like the thank everyone who has given me advice and assistance on my various projects, including (but almost certainly not limited to), alphabetically: David Goluskin, and everyone else at WHOI GFD; Chris Howland, for regular idea-bouncing, and being the progenitor of all the projects within the PhD; Alexis Kaminski, for inspiring and advising me, and generally being a lovely person; Jacob Page, for the collaboration in Appendix B and many other interesting discussions; Bill Smyth, for advice and assistance with his linear stability code; and the anonymous reviewers on the papers, without whom they would undoubtedly be much worse.

Of course I must acknowledge Colm and Rich, whose contrasting (and not infrequently, conflicting) perspectives on the field, on PhD studies and on life complemented one another so well, and who kept me motivated and always moving in the right direction. Colm, thank you for encouraging me to come back for the PhD in the first place, and for always having time for me despite your myriad responsibilities. Rich, thank you for serendipitously appearing in Cambridge at the right time; I did not ask to work with you, but I don't regret having done so.

For keeping me sane and entertained during my studies, I am deeply thankful to everyone in Pavillion H at DAMTP, but especially to Ben Young and Leo Middleton, who always kept me distracted when I needed to concentrate, and vice-versa. I hope I have done the same for you.

Abstract

Stably stratified shear flows, in which a less dense layer of fluid lies above and moves counter to a more dense layer below, are ubiquitous in geophysical fluid dynamics. These are often found to be unstable if the non-dimensional Richardson number Ri, quantifying the strength of stratification to shear, is sufficiently low. This is of particular importance in oceanography, where shear instabilities are conjectured to be important in the generation of turbulence in the deep ocean, an area of huge uncertainty in contemporary climate models. The Miles-Howard theorem tells us that for a steady, inviscid, parallel shear flow, if the local Richardson number is everywhere greater than one quarter, the flow is stable to infinitesimal perturbations. Though an important result, the strong restrictions in the applicability of this theorem mean care must be used when applying the criterion of $Ri > 1/4$ for stability. This thesis explores some of these limitations, beginning with an overview in chapter 1.

Chapter 2 explores the infinitesimal restriction of the Miles-Howard theorem, by asking whether finite-amplitude perturbations could lead to significant nonlinear behaviour, in a so-called subcritical instability. It is found that while the classical Kelvin-Helmholtz instability does indeed exhibit subcriticality, nonlinear steady states are found only just above $Ri = 1/4$.

Chapter 3 investigates in detail a hitherto unknown linear instability, which was discovered in chapter 2. Behaving similarly to the classic Holmboe instability, it exists for $Ri > 1/4$ when viscosity is introduced, and reveals new insights into the possible physical interpretations of stratified shear instability.

Chapter 4 revisits the results of chapter 2 but considers two cases of the Prandtl number Pr, the ratio of diffusivity of the momentum to density. When $Pr = 0.7$, as is approximately the case for air, a simple supercritical instability is found. However, for $Pr = 7$, corresponding approximately to water, strong subcritical behaviour is observed, and it is demonstrated that finite-amplitude perturbations can trigger Kelvin-Helmholtz-like behaviour well above $Ri = 1/4$.

Chapter 5 considers the time-varying, non-parallel flow of an oblique internal gravity wave incident on a shear layer. Using direct-adjoint looping, it is shown that the disturbances which maximise energy after a certain time, so-called linear optimal perturbations, can be convective-like rolls in the spanwise direction, rather than a shear instability, calling into question the relevance of the classical shear instabilities in oceanography.

Chapter 6 concludes the thesis with a discussion of the implications of the results.

Table of contents

Appendix C A sum-of-squares optimisation method for studying the double pendulum 137

Chapter 1

Introduction

Stably stratified shear flows, in which a less dense layer of fluid lies above and moves counter to a more dense layer below, are ubiquitous in geophysical fluid dynamics (GFD), being found in lakes (Preusse et al., 2010), rivers (Shi et al., 2019), the oceans (Van Haren and Gostiaux, 2010) and the atmosphere (Browning, 1971) of the Earth. The simplest example, of two distinct fluids of different densities moving at different speeds, is a classical problem, giving rise to the Kelvin-Helmholtz instability (KHI), and is universally used to teach students about hydrodynamic stability theory. Despite this, the complex nonlinear dynamics of idealised stratified shear flows, and in particular unbounded flows of the sort relevant to GFD, remain relatively unstudied compared with other model instabilities (Rayleigh-Bénard (Lohse and Xia, 2010), Taylor-Couette (Grossmann et al., 2016), pipe flow (Eckhardt et al., 2007) etc.), perhaps because of the difficulty of setting up laboratory experiments.

1.1 The Miles-Howard theorem

Arguably the most important analytic result in the mathematical theory of stratified shear instability is the Miles-Howard theorem, which will be a central focus of this thesis. In the 1950s, much evidence was pointing to the fact that stratified shear flows are stabilised when the Richardson number is greater than one quarter (Drazin, 1958; Holmboe, 1960). One non-rigorous justification for this is given by Chandrasekhar (1961), though it has been argued that this line of reasoning should really give a criterion of Richardson number one (Miles, 1986). The problem was solved in 1961 with the publication of Miles (1961), and the subsequent Howard (1961) which gave a more succinct and general proof. The statement of the theorem can be given as follows:

Theorem (Miles-Howard)**.** *A one-dimensional, stratified shear flow, as governed by the inviscid Boussinesq equations, is linearly stable so long as the gradient Richardson number* $Ri_g := -\frac{g}{\rho}\frac{\partial\rho/\partial z}{(\partial u/\partial z)^2}$ *satisfies* $Ri_g > 1/4$ *everywhere in the flow.*

To simplify application of this theorem, it is usual to define $Ri_m := \min_z Ri_g$, and so we are guaranteed stability if $Ri_m > 1/4$.

Several important restrictions are hidden within the statement of this theorem. The Boussinesq equations used to derive the theorem, governing the evolution of the momentum and density of the flow, assume that density differences are sufficiently small compared with the absolute density that they are not relevant to the inertia of the fluid, but are still relevant for the buoyancy term in the equations. Additionally implicit is the fact that we are not considering a rotational flow, so that the Coriolis force does not come in to play. Both of these assumptions are usually valid for small scale dynamics in oceanography, and we do not investigate them further.

More important are the assumptions that we are studying a perfectly steady, one dimensional shear flow, that viscosity is completely ignored and that infinitesimal perturbations (i.e. the linearised equations) are sufficient. Clearly none of these three are valid in the complex and chaotic flows which develop in the ocean, and so we must question how, when these restrictions are relaxed, they affect the Miles-Howard theorem.

1.2 The Miles-Howard criterion in oceanography

One particularly important application of the instability of stratified flows is in oceanography. Modelling of the world's oceans as a system is crucial to understanding the transfer and storage of energy, and is necessary to make predictions about the future of the climate. Energy budgets suggest that the poorly understood generation of turbulence in the oceans is a key process in closing the system (Wunsch and Ferrari, 2004). However, such turbulence occurs on scales much too fine to be captured directly though large scale numerical simulations, and this is likely to remain the case for many decades. Therefore, parameterisations of the generation of turbulence are necessary, and these remain a major area of uncertainty in ocean circulation models.

Parameterisations often employ a critical Richardson number Ri_c (Mellor and Yamada, 1982; Kunze et al., 1990), and empirically or by appeal to the Miles-Howard theorem, this is taken to be $Ri_c = 1/4$. Observations show (Polzin, 1996; Mack and Schoeberlein, 2004) that the presence of turbulence is correlated with lower measured Richardson numbers, though no clear cutoff at a particular value is detected. Of course, no discretised measurements will ever be able to accurately capture the minimum Richardson number, which may go some way to explain the lack of a distinct threshold. More recently (Thorpe and Liu, 2009; Smyth and Moum, 2013), $Ri_c = 1/4$ has been proposed as the critical value in a marginal stability process, in which, if the value drops below $1/4$, the system becomes unstable and thereby increases Ri.

These applications of a *Miles-Howard criterion*, as opposed to the *Miles-Howard theorem*, by which we mean using a value $Ri_c = 1/4$ in situations for which the theorem is not proven, are the main motivation for the work in this thesis. We examine, through numerical methods, the different ways the restrictions of the theorem, when relaxed, affect the behaviour of stratified shear flows.

1.3 Structure of the thesis

The rest of the thesis comprises of four chapters of content, two of which have been published as Parker et al. (2019, 2020) and a third which is in review, plus concluding remarks in chapter 6. Each of the chapters has its own introduction section giving background to that specific area.

Chapter 2 gives the first bifurcation analysis of Kelvin-Helmholtz instability (KHI), with the aim of investigating whether, with finite-amplitude disturbances, nonlinear effects can cause instability-like behaviour at $Ri_m > 1/4$, in violation of the Miles-Howard criterion.

Chapter 3 is a detailed study of the viscous Holmboe instability (VHI) that is discovered and briefly discussed in chapter 2. This instability, which is not present in the inviscid limit, allows us to explore the inviscid restriction of the Miles-Howard theorem. The hitherto unknown instability also sheds new light on two potential physical interpretations of stratified shear instabilities, the wave resonance argument and the wave overreflection hypothesis.

Despite substantial evidence to the importance of Pr, many numerical studies, indeed including the other chapters of this thesis, use the convenient value $Pr = 1$. This is unrealistic for atmospheric flows, for which $Pr \approx 0.7$, temperature-stratified oceanic flows, for which $Pr \approx 7$, and salt-stratified oceanic flows, for which the equivalent Schmidt number $Sc \approx 700$. The latter of these is presently computationally infeasible, but for $0.7 < Pr < 7$, we can apply the methods of chapter 2, which we do in chapter 4. We find that the water case $Pr = 7$ is substantially more complex than the air case $Pr = 0.7$.

Chapter 5 takes a step back from idealised models of stratified shear layers to the larger scale picture of a full breaking internal gravity wave. In the presence of a background shear, we investigate which disturbances actually lead to wave breaking in three dimensions, and demonstrate that an intrinsically three-dimensional, convectively driven mechanism is many orders of magnitude more energetic than a simple shear instability for the parameters studied.

There are three appendices to this thesis. Appendix A is a discussion of the DNS code which was written during the course of the PhD and was used for all computations in the main part of the thesis, with the exception of the linear stability analysis of 1D flow profiles. Appendices B and C are papers of projects in the area of computational applied mathematics that were completed during the course of the PhD but are thematically unrelated to the rest of the thesis. Appendix B, written in collaboration with Jacob Page, concerns Dynamic Mode Decomposition (Schmid, 2010; Kutz et al., 2016), a numerical machine learning method, and its analytic counterpart, Koopman analysis (Mezić, 2013). Appendix C, in collaboration with David Goluskin and others from the Geophysical Fluid Dynamics programme at Woods Hole Oceanographic Institute, discusses Sum-of-Squares optimisation (Lasserre, 2001; Parrilo, 2003), a numerical method which can be used to analyse dynamical systems without discretisation.

Chapter 2

Kelvin-Helmholtz billows above Richardson number one quarter[1]

---

[1] This chapter is a slightly modified version of Parker, J. P., Caulfield, C. P., & Kerswell, R. R. (2019), Kelvin-Helmholtz billows above Richardson number $1/4$. *Journal of Fluid Mechanics, 879*, R1.

Abstract

We study the dynamical system of a two-dimensional, forced, stratified mixing layer at finite Reynolds number *Re*, and Prandtl number $Pr = 1$. We consider a hyperbolic tangent background velocity profile in the two cases of hyperbolic tangent and uniform background buoyancy stratifications, in a domain of fixed, finite width and height. The system is forced in such a way that these background profiles are a steady solution of the governing equations. As is well-known, if the minimum gradient Richardson number of the flow, Ri_m, is less than a certain critical value Ri_c, the flow is linearly unstable to Kelvin-Helmholtz instability in both cases. Using Newton-Krylov iteration, we find steady, two-dimensional, finite-amplitude elliptical vortex structures – i.e. 'Kelvin-Helmholtz billows' – existing above Ri_c. Bifurcation diagrams are produced using branch continuation, and we explore how these diagrams change with varying *Re*. In particular, when *Re* is sufficiently high we find that finite-amplitude Kelvin-Helmholtz billows exist when $Ri_m > 1/4$ for the background flow, which is linearly stable by the Miles-Howard theorem. For the uniform background stratification, we give a simple explanation of the dynamical system, showing the dynamics can be understood on a two-dimensional manifold embedded in state space, and demonstrate the cases in which the system is bistable. In the case of a hyperbolic tangent stratification, we also describe a new, slow-growing, linear instability of the background profiles at finite *Re*, which complicates the dynamics.

2.1 Introduction

The Miles-Howard theorem (Miles, 1961; Howard, 1961) tells us that for inviscid, infinitesimal perturbations to steady, one-dimensional, parallel shear flows, the minimum gradient Richardson number Ri_m of the flow must be less than $1/4$ for such 'linear' perturbations to grow exponentially. From this, it is often argued that oceanic measurements will always find a Richardson number greater than or equal to $1/4$, otherwise turbulence will ensue (see Smyth et al., 2019, and references therein), despite the very specific restrictions on the applicability of the theorem. In this chapter we will examine two aspects of these restrictions, namely that perturbations are infinitesimal and inviscid.

With finite-amplitude perturbations, nonlinear effects can no longer be neglected. There is various evidence that for flows susceptible to Kelvin-Helmholtz instability (KHI), complex nonlinear behaviour exists when $Ri_m > 1/4$. Kaminski et al. (2017) showed that perturbations which grow transiently before decaying in the linearised setting can lead to turbulent-like irreversible mixing with $Ri_m > 1/4$ when nonlinearity is included. Howland et al. (2018) showed that as $Ri_m \to 1/4$ from below, the maximum amplitude of a saturated Kelvin-Helmoltz billow does not tend to zero, but to some finite value. One possible cause of these observations is that the pitchfork bifurcation, generically expected to occur (Strogatz, 2014) at the critical Richardson number, Ri_c, is subcritical, so that finite-amplitude states exist above Ri_c. This could mean that the system is bistable (meaning there are two stable states) in a certain range of Ri_m with $Ri_m > Ri_c$. (Note that by 'subcritical' here we mean those regions where the base flow is linearly stable, *above* Ri_c, consistent with normal dynamical systems terminology, as opposed to the occasional oceanographic usage meaning *below* Ri_c.)

Historically, the best way to determine the nature of the bifurcation has been to consider the next-order nonlinear effects, a so-called weakly nonlinear analysis. Such analysis has been performed for both of the models of a stratified shear layer we consider using critical layer theory (Maslowe, 1977; Brown et al., 1981; Churilov and Shukhman, 1987), in some cases finding subcriticality. These results have also been confirmed, in the case of the Drazin model, using direct numerical simulations to investigate the nonlinear behaviour near criticality (Lott and Teitelbaum, 1992; Mkhinini et al., 2013). However, our results suggest that the weakly nonlinear analysis can potentially be misleading, as discussed in section 2.4, since higher-order effects can quickly dominate. Critical layer theory has also been used to demonstrate the existence of nonlinear neutral modes in stratified shear flow, resembling Kelvin-Helmholtz billows, but with nonzero phase speed (Maslowe, 1973). It is inferred that such modes may exist when $Ri_m > 1/4$.

More recently, as it has become possible computationally to solve the Navier-Stokes equations directly, finding the finite-amplitude states which arise from bifurcations has emerged as an alternative. Newton's method can be used to find solutions of nonlinear problems, such as steady states, iteratively. The introduction of Newton-Krylov methods (Edwards et al., 1994), where a Krylov-subspace method such as generalised minimal residuals (GMRES) (Saad and Schultz, 1986) is used to solve the linear system inexactly at each Newton step, has allowed this to be applied to very high-dimensional systems for which it is prohibitively expensive to work with the Jacobian matrices of the flow directly (for a comprehensive review, see Dijkstra et al., 2014). It is also possible to use Newton's method to find and track bifurcation points of high-dimensional dynamical systems (Salinger et al., 2002; Haines et al., 2011). Net and Sánchez (2015) used a matrix-free bifurcation tracking technique with a Newton-Krylov method, as employed in this chapter, and further extended this to find bifurcations of periodic orbits.

In this chapter, we find the exact coherent states that bifurcate from the base flow at Ri_c, and track these as both Ri_m and Re vary, to build a picture of the dynamical system near $Ri_m = 1/4$, and, crucially, answer the question of whether the system can be bistable above Ri_c. Two different models susceptible to KHI are considered. The first, the 'Holmboe' model (Holmboe, 1962), with a hyperbolic tangent buoyancy profile, is the standard model in this field (Hazel, 1972; Klaassen and Peltier, 1985; Smyth and Peltier, 1991; Mallier, 2003). However, we demonstrate that complex behaviour arises – associated with what we believe to be a previously unreported linear instability – and dominates at long times when this model is forced onto the system at finite *Re*, obscuring the KHI. We then examine an alternative 'Drazin' model (Drazin, 1958), with a uniform stratification, which shares many of the features of the Holmboe model but does not exhibit this complex behaviour. Note that, with the parameters studied, both the Drazin and Holmboe models are only known to be susceptible to stationary KHI, and not the propagating 'Holmboe wave instability' (HWI). The chapter proceeds as follows: in section 2.2, we describe the methodology and code used. In section 2.3.1 a bifurcation diagram is presented for the Holmboe model, as well as a description of the newly discovered linear instability. In section 2.3.2, a bifurcation diagram and a full description of the dynamics is given for the Drazin model. Section 2.4 gives a brief discussion of these results.

2.2 Methodology

We consider the Boussinesq equations in two dimensions, and study the nonlinear evolution of perturbations away from a steady parallel velocity profile $U(z)$ and buoyancy stratification $B(z)$. Solving for the perturbation away from these constant-in-time profiles is equivalent to solving for the full system, with an artificial body force to counteract diffusion. In non-dimensional form, the equations are:

$$\partial_t u + (U+u)\,\partial_x u + w\partial_z (U+u) = -\partial_x p + \frac{1}{Re}\left(\partial_x^2 u + \partial_z^2 u\right), \tag{2.1}$$

$$\partial_t w + (U+u)\,\partial_x w + w\partial_z w = -\partial_z p + \frac{1}{Re}\left(\partial_x^2 w + \partial_z^2 w\right) + Ri_b b, \tag{2.2}$$

$$\partial_t b + (U+u)\,\partial_x b + w\partial_z (B+b) = \frac{1}{PrRe}\left(\partial_x^2 b + \partial_z^2 b\right), \tag{2.3}$$

$$\partial_x u + \partial_z w = 0. \tag{2.4}$$

Here u is the fluid velocity in the horizontal (x) direction, and w is the velocity in the vertical (z) direction. Buoyancy acts in the positive z direction. We impose periodic boundary conditions at $x=0$ and $x=L_x$, and at $z=\pm L_z$ we enforce no-penetration ($w=0$), stress-free ($\partial u/\partial z = 0$), and insulating ($\partial b/\partial z = 0$) boundary conditions. Given the dimensional shear layer depth, $2L$, velocity difference $2\Delta U$, density difference $2\Delta\rho$, typical density ρ^*, and diffusivities of momentum ν and density κ, the Reynolds number is defined as $Re = \frac{\Delta U L}{\nu}$, the Prandtl number $Pr = \frac{\nu}{\kappa}$, and the bulk Richardson number $Ri_b = \frac{g}{\rho^*}\frac{L\Delta\rho}{\Delta U^2}$. Throughout, we take $Pr = 1$ for simplicity. Two different choices of U and B are considered in sections 2.3.1 and 2.3.2 respectively. For both background flows studied, the minimum gradient Richardson number Ri_m, as relevant to the Miles-Howard theorem, is equal to the bulk Richardson number Ri_b.

2.2.1 Discretisation

A new solver was developed to solve the Boussinesq equations around arbitrary background flows. Time integration uses a third order Runge-Kutta-Wray scheme, and spatial derivatives are handled pseudo-spectrally in the periodic horizontal direction, and with explicitly conservative quasi-second order finite differences in the vertical, on a non-uniform staggered grid: the nth of N grid points is located at

$$z = \frac{L_z}{3}\left[2\left(\frac{2n-N-1}{N-1}\right)^3 + \left(\frac{2n-N-1}{N-1}\right)\right].$$

This ensures that there are more grid points near the shear layer at the centre of the domain than at the edges. The code was validated against DIABLO (Taylor, 2008). Further, a linearised version of the same timestepper was produced, and validated against states of very low amplitude in the full nonlinear solver. For the system studied in section 2.3.1, a grid is used with 256 equispaced points in the streamwise direction and 512 points in the vertical direction, with a greater density of points in the middle of the domain. For the system studied in section 2.3.2, 128 points are used in the streamwise direction, covering a shorter domain, and 768 vertically, in order to accurately capture behaviour at higher Re. The results are validated by reconverging certain solutions at a higher resolution of 384×768 in section 2.3.1 and 256×1024 in section 2.3.2.

2.2.2 Steady states and bifurcation points

Formally, we may describe our dynamical system as the evolution of a state X by a time t through

$$X(t_0+t) = F\left(X(t_0), t; Ri_b, Re\right), \tag{2.5}$$

where Ri_b and Re are the constant parameters at which we are considering the evolution. Finding steady states of the flow is then equivalent to finding solutions to

$$F(X, T; Ri_b, Re) - X = 0 \tag{2.6}$$

for some arbitrary fixed T. It is possible, though extremely unlikely, that this will also find a periodic orbit of period T.

Solving (2.6) is done by using Newton-GMRES (generalised minimum residual) iteration on an initial guess. Our implementation matches that employed by Chandler and Kerswell (2013), including the use of a trust region to make the algorithm globally convergent. The GMRES iteration at each Newton step is continued until the residual is less than 10^{-2}, and the Newton iteration is continued until its residual, the norm of the left-hand side of (2.6), is less than 10^{-8}. A suitable T must be chosen to optimise the GMRES method. A larger T acts to precondition the equations, since if T is small, all states will appear to be stationary. However, if T is too large, computation will be prohibitively expensive. For our system, we found $T = 11$ to be a good compromise.

Through trial and error, we converge a steady billow solution, the result of a very long time integration of equations (2.1-2.4), at $Re = 1000$ and $Ri_b = 0.2$, in both the flows studied in this chapter. Once one state is found at these particular Ri_b and Re, we converge another very close by at a different Ri_b but the same Re. We then follow the solution branch at this Re over a range of Ri_b using pseudo-arclength continuation (Keller, 1977). We examine the stability of the branch with Arnoldi iteration, using a linearised version of the same timestepping code.

The stability analysis reveals the existence of bifurcation points, where eigenvalues of the state cross a stability boundary. To continue these bifurcation points to different Re, we use the states found by stability analysis as an initial guess in a different iterative solver. The system we solve is similar to that implemented in the Library of Continuation Algorithms (Salinger et al., 2002), but we use a matrix free method, as discussed in detail in Sánchez and Net (2016). We look for solutions to

$$F(X,T;Ri_b,Re)-X=0, \tag{2.7a}$$

$$F_X(X,Y,T;Ri_b,Re)-Y=0, \tag{2.7b}$$

$$Y\cdot A-1=0, \tag{2.7c}$$

with Newton-GMRES. In this case we allow X, Y and Ri_b to be found by the iteration, but hold Re fixed. Here $F_X(X,Y,t;Ri_b,Re)$ is the linearised time evolution of a state Y about a nonlinear state X, computed using the linearised timestepper. Equation (2.7b) enforces that Y is a neutral eigenmode of the Jacobian at X. We normalise Y using (2.7c), with some fixed arbitrary state A, which we take to be the initially guessed value of Y. Once bifurcation points are found at a particular Re, they are reconverged at higher Re. We are particularly interested in how the Ri_b value of the bifurcation point varies with Re.

Equations (2.7) find bifurcation points with purely real neutral eigenmodes, i.e. pitchfork and saddle-node bifurcations. For Hopf bifurcations, a set of five equations is needed, including two different linearised time evolutions. These arise from the real and imaginary parts of the eigenvalue $e^{i\theta}$ of the time-integrated system, corresponding to the purely imaginary eigenvalue $i\theta/T$ of the Jacobian. The following are solved for the unknowns X, Y_1, Y_2, Ri_b and θ:

$$F(X,T;Ri_b,Re)-X=0, \tag{2.8a}$$

$$F_X(X,Y_1,T;Ri_b,Re)-\cos\theta\, Y_1+\sin\theta\, Y_2=0, \tag{2.8b}$$

$$F_X(X,Y_2,T;Ri_b,Re)-\sin\theta\, Y_1-\cos\theta\, Y_2=0, \tag{2.8c}$$

$$Y_1\cdot A-1=0, \tag{2.8d}$$

$$Y_2\cdot A=0. \tag{2.8e}$$

In this case we use equations (2.8d) and (2.8e) to normalise the eigenmodes. The first removes the degeneracy from the eigenproblem, with A taken to be the inital guess of Y_1, and the second enforces that Y_2 not be parallel to Y_1, in order that we find a Hopf bifurcation, otherwise equations (2.8) reduce to (2.7). The additional computational requirements of (2.8) mean that we are unable to track Hopf bifurcations to as high Reynolds numbers as pitchfork and saddle-node bifurcations.

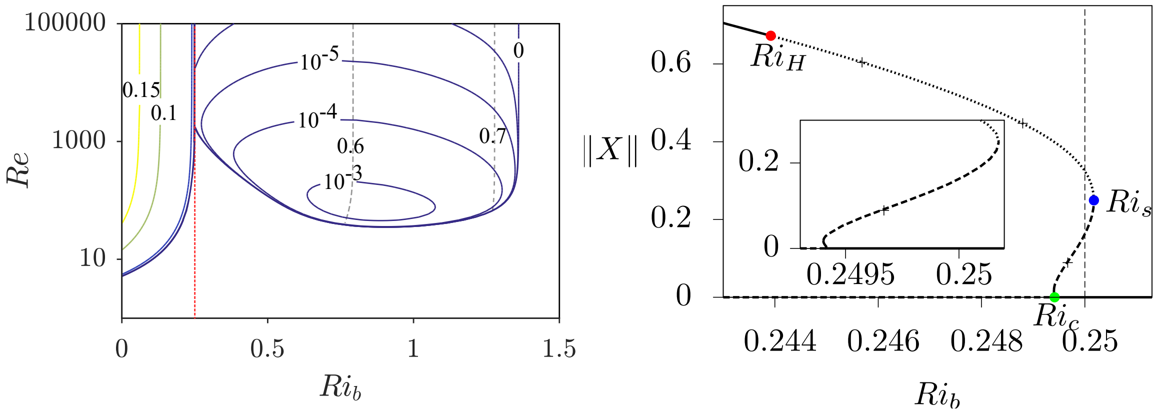

(a)

(b)

Fig. 2.1 (a) Contours of the complex growth rate $\sigma = -ikc$ where a normal mode is taken proportional to $exp(ik(x-ct)$ in a linear stability analysis of the background flow. The solid lines show the real part and the dashed grey lines show the imaginary part. For $Ri_b < 1/4$, the dominant instability mechanism is the stationary KHI, with a purely real growth rate. The newly described instability, discussed in the text, is the only one for $Ri_b > 1/4$, and has a very small growth rate, with nonzero imaginary part, so manifests as a propagating disturbance. (b) Bifurcation diagram for the flow with hyperbolic tangent background stratification, at $Re = 4000$, showing the variation of $\|X\|$ over a (very narrow) range of Ri_b. All states are unstable to the new propagating instability but beyond that, the solution branch has one further unstable eigenmode (------), two further unstable eigenmodes (⋯⋯), or is otherwise stable (——). Ri_H is plotted with a red dot, Ri_s with a blue dot and Ri_c with a green dot. The crosses mark points converged at the higher resolution of 384×768.

2.3 Results

2.3.1 Hyperbolic tangent stratification: the Holmboe model

First we consider a background profile of $U = \tanh z$, $B = \tanh z$. This is a commonly used model of a mixing layer, introduced by Holmboe (1962). It has the useful property that, at infinite Re, the linear stability analysis can be performed analytically (Miles, 1963). With this choice, we find that the minimum gradient Richardson number Ri_m is equal to Ri_b, and so the Miles-Howard theorem tells us that the flow is certainly stable for $Ri_b > 1/4$. We choose $L_x = 4\pi$, which is one wavelength of the most unstable mode at $Ri_b = 1/4$ as $Re \to \infty$, assuming a domain of infinite height vertically. For numerically expediency, we take $L_z = 10$ so that in fact Ri_c tends to a value slightly less than $1/4$ as $Re \to \infty$.

Following Howland et al. (2018) we define the energy of perturbations to be

$$E = \frac{1}{2L_x} \int_0^{L_x} \mathrm{d}x \int_{-L_z}^{L_z} \mathrm{d}z \left(u^2 + w^2 + Ri_b b^2\right). \tag{2.9}$$

State space is taken as the space of all possible incompressible perturbation flows $X = (u, w, b)$, with norm $\|X\| := \sqrt{2E}$. Note that p is not a dynamical variable as it can be calculated from a Poisson equation forced by the velocity field.

Figure 2.1b shows a bifurcation diagram at $Re = 4000$. Where the background state becomes unstable, with decreasing Ri_b, to KHI at $Ri_c \approx 0.2494$, a pitchfork bifurcation occurs (the green dot on figure 2.1b), giving rise to a branch of finite-amplitude, billow-like states. This branch is initially stable as it bifurcates – except to the unrelated instability discussed below – and decreasing in Ri_b, but there is soon a saddle-node bifurcation (see inset in figure 2.1b) and it then increases in Ri_b. As the unstable branch increases in amplitude, Ri_b increases, and we find steady, though unstable, states above $Ri_b = 1/4$. There is another saddle-node bifurcation at $Ri_s \approx 0.250175$ (blue dot), adding a second unstable direction to the branch. (If instead we take $L_z = 15$, we find $Ri_s \approx 0.250127$, so still $Ri_s > 1/4$.) The first saddle-node bifurcation was initially assumed to be a numerical artefact, but it was a consistent feature across all parameters studied in this model, at different resolutions. The branch stabilises at a Hopf bifurcation at $Ri_H \approx 0.244$ (red dot) when its two unstable eigenmodes simultaneously stabilise as a complex conjugate pair.

A very weak temporal linear instability, apparently hitherto unreported, is present in all states on the bifurcation diagram. As is conventional, we consider normal modes proportional to $\exp[ik(x - ct)]$, where the wavenumber k is required to be real, while the phase speed $c = c_r + ic_i$ is in general allowed to be complex, such that the (exponential) growth rate, generically complex, of any instability is defined to be $\sigma = -ikc$. Figure 2.1a shows the maximum growth rate of linear instability of the background state, as Ri_b and Re vary. For $Ri_b > 1/4$, the new instability is the dominant one. This has a phase speed of less than one, and manifests as counterrotating rolls, advected through the domain, above and below the interface, as shown in figure 2.2. As $Re \to \infty$, the growth rate tends to zero, as required by the Miles-Howard theorem. Close agreement of growth rates, to one part in 10^3, was found for this instability between the Arnoldi stability algorithm of our code, and a direct solution of the stratified Orr-Sommerfeld equations, using a MATLAB code by W. D. Smyth (Smyth and Carpenter, 2019). This instability, which we have termed viscous Holmboe instability (VHI), is studied and discussed in detail in chapter 3. Despite the small growth rate, at long times this instability leads to significant nonlinear behaviour in the artificially forced problem, which eventually dominates and masks the signature of KHI. A time series of this effect is shown in figure 2.3. This means we are unable to give a clean description of the dynamics on a two-dimensional manifold embedded within state space, as we do for the Drazin model in the following section.

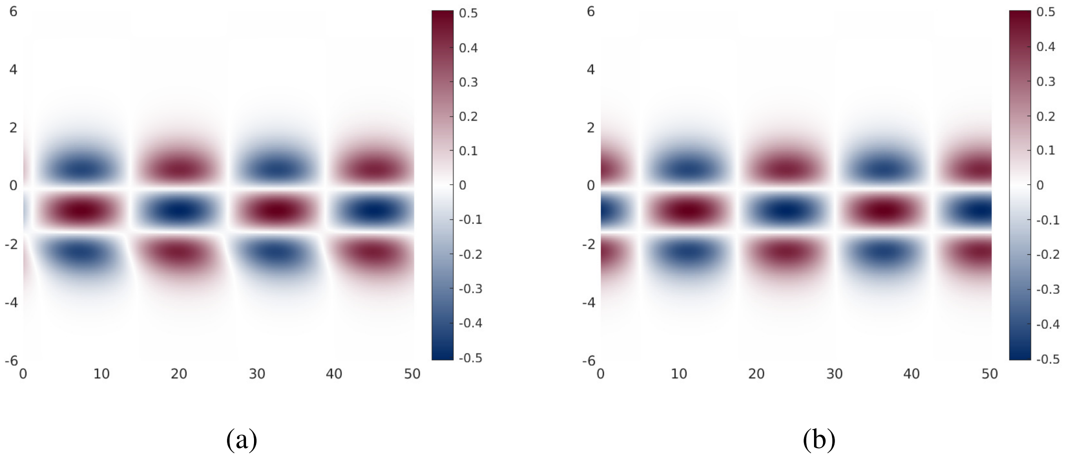
(a) (b)

Fig. 2.2 Real part of spanwise vorticity $\omega = \partial_x w - \partial_z u$ of the most unstable mode at $Ri_b = 0.25$, for a flow with (a) $Re = 4000$ and (b) $Re = 40000$. Two domain lengths are shown horizontally. The full domain is $[-10, 10]$ in the vertical direction. The growth rate $\sigma := -ikc$ of the $Re = 4000$ mode is $\sigma = 3.548 \times 10^{-6} + 0.5229i$. An equivalent mode also exists in the upper half of the domain, with growth rate $3.548 \times 10^{-6} - 0.5229i$.

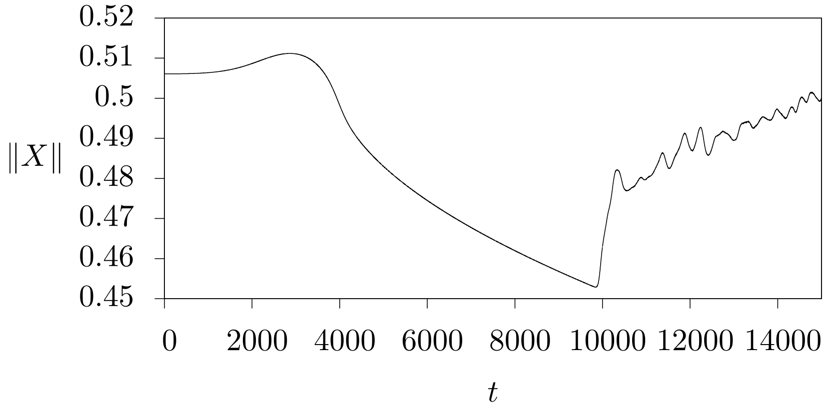

Fig. 2.3 The perturbation amplitude along a trajectory in the Holmboe model at $Re = 4000$ and $Ri_b = 0.2478$. The trajectory is started from a state very close to the unstable upper branch. It then follows a smooth path until about $t = 10000$, when the new instability has grown large enough to dominate. This then saturates and obscures the dynamics of the KHI.

2.3.2 Uniform stratification: the Drazin model

We now consider the case with a uniform background stratification, so that $U = \tanh z$ but $B = z$. This is also a commonly studied problem (Drazin, 1958; Churilov and Shukhman, 1987; Thorpe et al., 2013; Kaminski et al., 2014) as again, linear stability analysis can be performed analytically. As before, $Ri_m = Ri_b$ for this flow. Linear stability analysis on a domain of infinite height tells us we should now take $L_x = 2\sqrt{2}\pi$ to achieve $Ri_c \to 1/4$ as $Re \to \infty$. As before, $L_z = 10$. We use the same definition of energy E as in the hyperbolic tangent case.

Qualitatively, the bifurcation diagram is very similar to the tanh stratification case. Figure 2.4a shows the diagram for $Re = 4000$. The main difference from figure 2.1b is the lack of the first saddle-node bifurcation near the pitchfork. The values of the various bifurcation Richardson numbers are different; for example the Hopf bifurcation at Ri_H (shown in red) occurs at somewhat lower Ri_b than before. Also crucially, the propagating linear instability described in section 2.3.1 is no longer present, and consequently we can study the long-time behaviour of KHI.

The period of the Hopf bifurcation at $Re = 4000$ is approximately 1690 advective time units, which is much too high to allow us to converge the resulting periodic orbit directly, but long time integrations at a range of Ri_b give us an idea of the behaviour, since it appears to be stable in this case. Even this simple method becomes useless as we approach Ri_c, since the period increases towards infinity. This is the generic behaviour near a homoclinic bifurcation (Strogatz, 2014), which we believe occurs somewhere between Ri_c and Ri_s: the periodic orbit collides with the lower branch state.

The behaviour of the system, which we believe to be generic for sufficiently high Re, can be completely understood on a two-dimensional manifold described by the two most unstable eigenmodes, as shown schematically in figure 2.5. In region 1, where $Ri_b < Ri_H$, the base state is unstable, and the instability saturates and eventually leads to the upper branch steady state, which is stable. For $Ri_H < Ri_b < Ri_c$, region 2, the base state and upper branch are both unstable, and perturbations lead to a stable periodic orbit. Immediately to the right of the pitchfork bifurcation Ri_c in the region 3, the base state is stable and there exists a lower branch edge state, which is unstable. If finite-amplitude perturbations to the base state are past this edge, they are attracted to the periodic orbit, and we have subcritical 'transition'. Between regions 3 and 4, there is a homoclinic bifurcation of the periodic orbit with the lower branch state. This means that in region 4, the periodic orbit no longer exists. There are unstable finite-amplitude states and large transient trajectories, but the base state is the only attractor. In region 5, past the saddle-node bifurcation, $Ri_b > Ri_s$, the base state is the only known exact coherent structure. Of course, in reality the finite-amplitude states break the

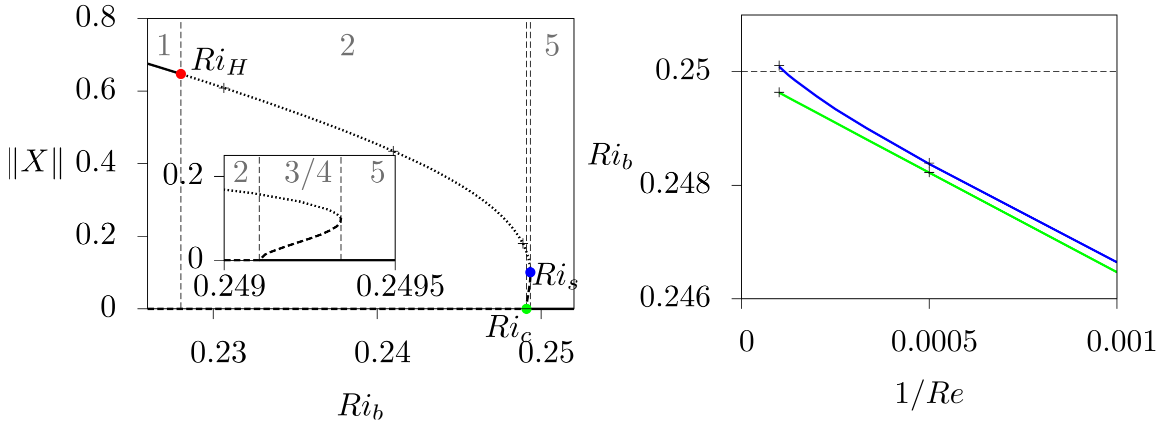

(a) (b)

Fig. 2.4 (a) Bifurcation diagram of the flow with uniform background stratification, at $Re = 4000$. The dashed vertical lines separate the numbered regions, as discussed in the text. The solution branch has one unstable direction (------), two unstable directions (············), or is stable (——). Ri_H is plotted with a red dot, Ri_s with a blue dot and Ri_c with a green dot. (b) Variation of Ri_c (green) and Ri_s (blue) with $1/Re$. Ri_s passes through $1/4$ at $Re \approx 9000$. In both figures, the crosses mark points converged at the higher resolution of 256×1024.

translational symmetry of the base state, and there are in fact a continuum of upper branch states, periodic orbits and so on, with a shift of origin. Which of these the system is attracted to depends on the phase of the initial perturbation.

All of the stationary states we have found, as well as the periodic orbit, are the result of bifurcations away from the parallel base state. It is possible that other states exist in the system which are not connected to this base state at all; as is the case, for example, for the Nagata solutions in plane Couette flow (Nagata, 1990). The existence of these isolated solutions would complicate the above description of the dynamical system. However, we have seen no evidence of any such states in any of our results. If they exist in our flow, therefore, we assume them to be unimportant for the range of parameters considered.

Figure 2.6 shows the vorticity structure of the steady states at two different values of Ri_b. In the case of the Hopf bifurcation, billow-like structures are clearly seen, bearing a strong resemblance to the saturated, unsteady billows found by Howland et al. (2018). Increasing Ri_b along the upper branch to the saddle-node bifurcation, these structures remain but become significantly less pronounced. Baroclinic effects mean that the height of the billows decreases with increasing Ri_b.

We track the values of Ri_c and Ri_s for Re from 1000 to 10000 using the method described in section 2.2.2, and the results are shown on figure 2.4b. As $Re \to \infty$, extrapolation, assuming linearity in $1/Re$, suggests $Ri_c \to 0.25 - 1.4 \times 10^{-5}$, slightly less than $1/4$ because

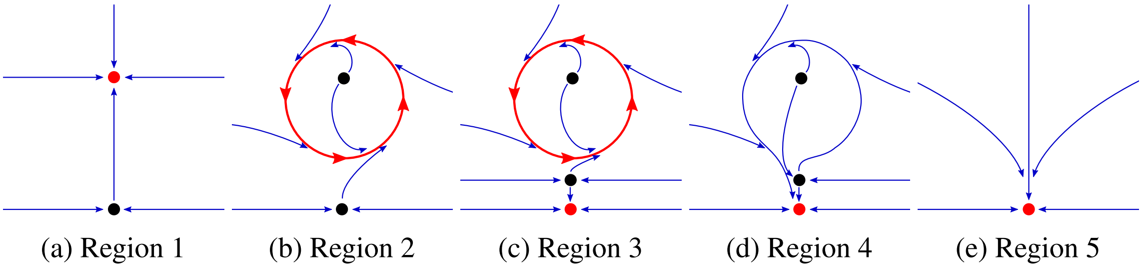
(a) Region 1 (b) Region 2 (c) Region 3 (d) Region 4 (e) Region 5

Fig. 2.5 Schematics of the dynamical system restricted to the two dimensional manifold of the two most unstable eigenmodes. The dots mark steady states, the lower being the base solution, and the lines show a few relevant trajectories. Solutions shown in red are stable, and those in black are unstable.

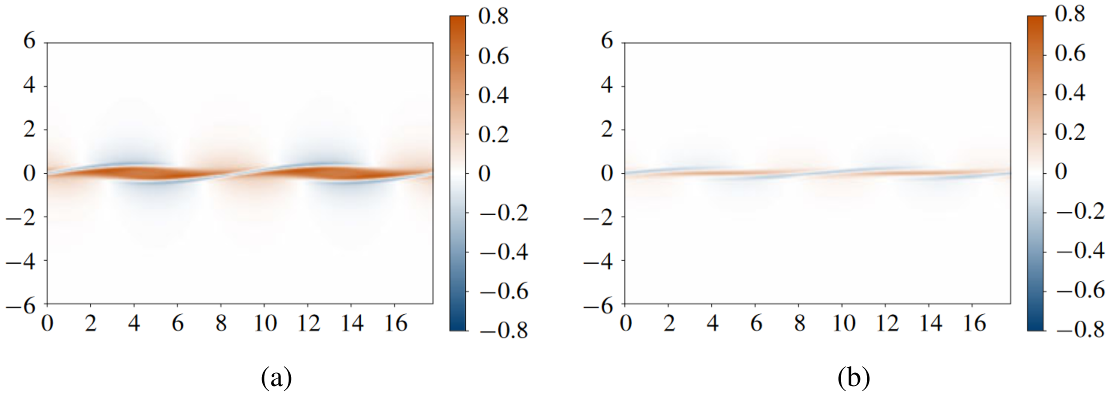

(a) (b)

Fig. 2.6 Spanwise vorticity $\omega = \partial_x w - \partial_z u$ of the stationary states at the (a) Hopf $Ri_H = 0.22803$ between regions 1 and 2 and (b) saddle-node $Ri_s = 0.24934$ between regions 4 and 5, for the flow in figure 2.4a. Two domain lengths are shown horizontally. The full domain is $[-10, 10]$ in the vertical direction.

of the finite height of the domain. We find that $Ri_s > 1/4$ for $Re \gtrsim 9000$ and estimate that $Ri_s \to 0.251$ as $Re \to \infty$. Since we have been unable to find the location of the conjectured homoclinic bifurcation, we are unable to say whether region 3, with a stable periodic orbit, extends above $Ri_b = 1/4$, and hence whether the system is bistable here. Nevertheless, region 4 certainly exists above $Ri_b = 1/4$, so there will be nonlinear transient behaviour, with the development of Kelvin-Helmholtz style billows as shown in figure 2.6. We have also tracked the Hopf bifurcation (omitted from figure 2.4b for scale reasons) and this shows a similar trend to the saddle-node bifurcation.

2.4 Discussion and Conclusions

The Miles-Howard theorem is an important result in the theory of linear stability of inviscid flows. However, the fact it seems to work in more general conditions than those for which it is proven means it has been informally applied as a ‘rule of thumb’ at high *Re*. We have shown that subcritical instability can exist in such flows, so that complex nonlinear behaviour can occur even when the flow is linearly stable. This is not a new result; Maslowe (1977) found subcritical instability in the Holmboe model with $Pr = 0.72$ and $Re = 100$ using a weakly nonlinear analysis. We note however, that this technique of finding the first order correction to the linear theory would have given misleading results applied to the parameters we study, since in the Holmboe model, we find a saddle-node bifurcation very close to the pitchfork, leading to subcritical instability instead of the apparent supercriticality. Furthermore, the technique presented in this chapter allows us to precisely find the location of the saddle-node bifurcations, and demonstrate explicitly that finite-amplitude billows exist at $Ri_b > 1/4$, which has only been inferred previously (Howland et al., 2018; Kaminski et al., 2017).

We have been able to give a simple description of the dynamics in the Drazin model. It is not immediately clear that the dynamics of the artificially forced system studied here will be relevant to those of an unforced system, which has traditionally been used as a model for geophysical flows. The incredibly long periods of the orbits born from the Hopf bifurcation discussed earlier, for example, mean that in an unforced problem, the background flow would have diffused almost entirely away before one complete cycle. Nevertheless, the instability of the unforced flows still leads to saturated states very similar to the steady solutions we have found, and the subcriticality we have demonstrated would certainly lead to non-trivial transient behaviour.

Our results alone do not invalidate the use of $Ri_b = 1/4$ as a ‘rule of thumb’ for criticality. The subcriticality we have found extends only very slightly about $1/4$ in both cases studied. However, the results of Brown et al. (1981) and Churilov and Shukhman (1987), who respectively studied the Holmboe and Drazin models using weakly nonlinear analysis, show strong subcriticality when $Pr > 1$ but supercriticality when $Pr < 1$ and that higher-order terms must be considered at our choice of $Pr = 1$. Preliminary results tracking the saddle-node bifurcation points in our work as Pr varies seem to agree with this, so future research will concentrate on the more oceanographically relevant range $Pr \sim O(10)$.

It should be noted that all our results have been performed at a fixed domain width L_x, and yet the wavelength of maximum growth of KHI is known to vary with Ri_b (Hazel, 1972). Therefore we expect our results would change at different L_x, but since we have chosen the wavelength of maximum growth at criticality and all our results are very close to Ri_c, it is to be assumed that our domain size is the most relevant to a physical flow.

In addition to these finite-amplitude nonlinear states, we have found linear instability with $Ri_b > 1/4$ in the Holmboe model (see figure 2.2), which disappears as $Re \to \infty$, as required by the Miles-Howard theorem. A similar phenomenon was found by Miller and Lindzen (1988). However, their instability had large growth rates and required a carefully constructed flow. We have found an instability in a widely used model, hitherto unreported to the best of our knowledge. The new instability has a tiny growth rate at physically realistic Re. This suggests it can be ignored in oceanic problems, but fails to entirely explain why it has not been discussed before. It is commonly assumed that finite Re effects are always stabilising compared to inviscid behaviour in such flows, despite demonstrations to the contrary (Defina et al., 1999). This instability demonstrates that such assumptions should be checked carefully. While it is not appropriate to classify this instability as ‘classic’ Holmboe wave instability, since HWI is an inviscid instability, we conjecture that it may be homotopically connected to Holmboe instability as parameters are varied, as it has a similar phase speed and occurs at similar values of Ri_b. This is an area for future research.

Chapter 3

The viscous Holmboe instability for smooth shear and density profiles[1]

---

[1] This chapter is a slightly modified version of Parker, J. P., Caulfield, C. P., & Kerswell, R. R. (2020). The viscous Holmboe instability for smooth shear and density profiles. *Journal of Fluid Mechanics, 896*, A14.

Abstract

The Holmboe wave instability is one of the classic examples of a stratified shear instability, usually explained as the result of a resonance between a gravity wave and a vorticity wave. Historically, it has been studied by linear stability analyses at infinite Reynolds number, *Re*, and by direct numerical simulations at relatively low *Re* in the regions known to be unstable from the inviscid linear stability results. In this chapter, we perform linear stability analyses of the classical 'Hazel model' of a stratified shear layer (where the background velocity and density distributions are assumed to take the functional form of hyperbolic tangents with different characteristic vertical scales) over a range of different parameters at finite *Re*, finding new unstable regions of parameter space, corresponding to the 'viscous Holmboe instability' observed in chapter 2. In particular, we find instability when the Richardson number is everywhere greater than $1/4$, where the flow would be stable at infinite *Re* by the Miles-Howard theorem. We find unstable modes with no critical layer, and show that, despite the necessity of viscosity for the new instability, the growth rate relative to diffusion of the background profile is maximised at large *Re*. We use these results to shed new light on the wave-resonance and over-reflection interpretations of stratified shear instability. We argue for a definition of Holmboe instability as being characterised by propagating vortices above or below the shear layer, as opposed to any reference to sharp density interfaces.

3.1 Introduction

Stably stratified shear flows are ubiquitous in the oceans and atmosphere. Their instabilities are believed to be relevant to a variety of geophysical processes, and understanding them is important, for example, in the irreversible mixing of fluid of different densities in the abyssal ocean to close ocean energy budgets. The classical example of a shear instability is the Kelvin-Helmholtz instability (KHI) of a uniform sheet of vorticity. Generally, this instability is damped when a stable stratification is introduced, and the linear instability is no longer found when the minimum Richardson number, quantifying the strength of stratification to shear effects, exceeds one quarter (Drazin, 1958; Miles, 1961; Howard, 1961). However, if a sharp density interface is considered, a qualitatively different, propagating instability is instead found (Holmboe, 1962; Hazel, 1972). This so-called Holmboe wave instability (HWI), or just ‘Holmboe instability’, is believed to be due to an interaction between internal gravity waves on the density interface and vorticity waves on either side of the shear layer. It is hypothesised to be important for ocean mixing (Salehipour et al., 2016), as sharp interfaces are naturally occurring at high Prandtl numbers.

One important result is the Miles-Howard theorem (Miles, 1961; Howard, 1961), which states that, in the inviscid case, a stratified shear profile is linearly stable so long as the local or gradient Richardson number Ri_g (defined precisely below in section 3.2) is everywhere greater than one quarter. For flows in which HWI is usually studied, including the piecewise linear profile of Holmboe (1962) and the one-sided profile of Baines and Mitsudera (1994), as well as the smooth profile studied by Hazel (1972), Ri_g is vanishingly small away from the shear layer, so the theorem does not apply, despite arbitrarily large *bulk* Richardson numbers (also defined more precisely in section 3.2). On the other hand, when the bulk Richardson number Ri_b is small, the internal waves are not strong, and so KHI is preferred over HWI.

Though the Miles-Howard theorem is only proven for inviscid flows, a Richardson number of one quarter is often employed as a criterion for stability in oceanography and related fields. It is argued from this that a density interface must be narrow compared with the shear layer for HWI to be present (Thorpe, 2005), quantified by the ratio R of shear layer thickness to buoyancy interface thickness being high. However, Miller and Lindzen (1988) showed that it is possible to have shear instabilities when $Ri_g > 1/4$ everywhere if viscosity is introduced. This leads to the possibility that HWI exists even when R is of order one, when $Ri_g > 1/4$, at finite Reynolds number. Such an instability was demonstrated, for a single specific choice of parameters, in chapter 2.This could have profound implications for our understanding of geophysical processes, since HWI is known to have very different mixing properties to KHI (Salehipour et al., 2016).

In addition to a succinct proof of the Miles-Howard theorem, Howard (1961) also proves an important result, now called the Howard semicircle theorem. This states that for an inviscid, parallel, stratified shear flow, the complex phase speed of any unstable mode must be located in a semicircle centred about the median velocity on the real axis, with radius of half the velocity difference. Though difficult to interpret directly, this has the immediate corollary that the phase speed of any instability must lie between the maximum and minimum velocities of the flow. For a smooth velocity profile, this means that there certainly exists a critical layer, at which the phase velocity equals the flow velocity, and the Taylor-Goldstein equation (see section 3.2) becomes singular. The behaviour of instabilities at the critical layer is a well-studied field (Maslowe, 1986; Troitskaya, 1991; Churilov and Shukhman, 1996), and leads to the over-reflection hypothesis discussed below. However, the semicircle theorem is again only proven for inviscid flows, and we shall see that it does not generalise when viscosity is taken into account.

Two different physical interpretations of stratified shear instabilities exist in the literature. The first, suggested originally by Taylor (1931), developed by Garcia (1956); Cairns (1979); Caulfield (1994) and Baines and Mitsudera (1994), and reviewed in detail by Carpenter et al. (2013), is the idea that a pair of waves can phase lock and mutually amplify one another if configured correctly. This leads to the classification of three canonical instabilities: KHI, the resonance of two vorticity waves; HWI, the resonance of a vorticity and an internal wave; and the so-called 'Taylor-Caulfield' instability (Taylor, 1931; Caulfield et al., 1995), the resonance of two internal waves. In practice, the distinction between these is not clear cut (Carpenter et al., 2010b; Eaves and Balmforth, 2019). In this chapter, we shall argue that any instability with zero phase speed in flows with a single density interface should be defined as KHI and any instability with a propagating localised vortex should be defined as HWI. The reason for this proposed classification is based on the qualitative nonlinear evolutions, as will become clear in section 3.4.

There is good evidence that an interaction of a gravity and a vorticity wave is responsible for (at least inviscid) HWI. For instance, Alexakis (2005) discovered additional bands of instability at higher Ri_b, which seem to be caused by the resonance of a higher-order gravity wave harmonic with the vorticity wave. In the piecewise linear model, directly considering the interaction of the two waves in isolation leads to accurate prediction of the band of instability (Caulfield, 1994; Baines and Mitsudera, 1994). One major problem with this wave-resonance description is that it does not account for the Miles-Howard theorem. It is not clear why, with a broader density interface, the waves should no longer be able to resonate and cause instability. Further, although KHI seems to be related to an interaction of two vorticity waves, the theory has not yet been able to explain the damping of this instability as Richardson number is increased.

A different perspective, developed by R. S. Lindzen and coauthors, and reviewed in Lindzen (1988), is based on the idea that when the local Richardson number is less than one quarter, the critical layer of a normal-mode wave incident on a stratified shear layer will 'over-reflect', and in the correct configuration, this may lead to exponential growth. This theory, although harder to understand intuitively than the wave-resonance picture, is attractive as it explicitly includes the Miles-Howard criterion. However, Smyth and Peltier (1989) showed that while wave over-reflection could accurately predict KHI and HWI in isolation, near the transition between the two, the theory was insufficient. In particular, there exist regions of parameter space where KHI exists, so the critical layer is located where the velocity vanishes, and yet $Ri_g > 1/4$ here so over-reflection is not expected.

In this chapter, we perform linear stability analyses over a wide range of parameters for the 'Hazel model' (Hazel, 1972), including viscosity which has usually been omitted in the past (Hazel, 1972; Smyth and Peltier, 1989; Alexakis, 2005, 2009). As well as finding a clear continuation of the classic inviscid HWI at values of R for which it is known to exist, we also find instability at much lower R, with growth rates which vanish as Reynolds number is increased. We term this new instability the viscous Holmboe instability (VHI), and demonstrate that it has many similarities to the classic HWI. Our results suggest that while the wave interaction theory gives a useful interpretation of the phenomenology, neither this nor the over-reflection theory is useful as a necessary or sufficient criterion to predict instability. We shall see that results from inviscid theory are not relevant here with viscosity present, even in situations where the Reynolds number is sufficiently high that a 'frozen flow' approximation is valid, and the diffusion of the background velocity and density distributions is not thought to be significant.

The remainder of the chapter is organised as follows. In section 3.2, we present the assumptions made and the equations solved. In section 3.3, linear stability analyses are presented over a wide range of different parameters, and the fastest growing Holmboe modes are tracked and discussed as Reynolds number and R are varied. Section 3.4 shows the nonlinear evolution of VHI at parameter values for which we expect it to grow fastest, and we compare this against the evolution of the classic, inherently inviscid HWI. In section 3.5, the results are discussed with particular emphasis on interpretation through wave-resonance and over-reflection.

3.2 Equations

In this chapter, we consider only two-dimensional perturbations to the background flow. This is a common assumption, by appealing to the results of Squire (1933) and Yih (1955), who showed that any three-dimensional normal mode can be associated with a two-dimensional one with smaller Richardson number and larger Reynolds number. However, this is not necessarily sufficient to show that the fastest growing mode is always a two-dimensional one (Smyth and Peltier, 1990). We discuss this further in section 3.5.

An infinitesimal normal-mode perturbation with vertical velocity $w(x,z,t) = \hat{w}(z)e^{ik(x-ct)}$ to an inviscid Boussinesq flow with velocity profile $U(z)$ and buoyancy profile $B(z)$ must satisfy the well-known Taylor-Goldstein equation

$$(U-c)\left(\partial_z^2-k^2\right)\hat{w}-U_{zz}\hat{w}=-\frac{B_z}{U-c}\hat{w}. \tag{3.1}$$

Here, k is the streamwise wavenumber of the perturbation, and $c=c_r+ic_i$ is the complex phase speed, so that the growth rate of a disturbance is given by $\sigma=kc_i$.

When kinematic viscosity ν^* and diffusivity of the buoyancy distribution κ^* are taken into account, (3.1) becomes the more complicated pair of equations

$$\begin{gathered}(U-c)\left(\partial_z^2-k^2\right)\hat{w}-U_{zz}\hat{w}=ik\hat{b}+\frac{1}{ik}\frac{1}{Re}\left(\partial_z^2-k^2\right)^2\hat{w},\\(U-c)\hat{b}+\frac{1}{ik}B_z\hat{w}=\frac{1}{ik}\frac{1}{PrRe}\left(\partial_z^2-k^2\right)\hat{b},\quad Re\equiv\frac{U_0^*d_0^*}{\nu^*};\ Pr\equiv\frac{\nu^*}{\kappa^*},\end{gathered} \tag{3.2}$$

where length scales and time scales have been non-dimensionalised using the half-depth d_0^* of the shear layer, and half the velocity difference U_0^* across the shear layer, leading to a conventional definition of the Reynolds number Re, and Pr is the usual Prandtl number.

Following Hazel (1972) and many subsequent authors, we consider the ‘Hazel’ model for the background velocity and buoyancy distributions:

$$U(z)=\tanh z,\ B(z)=\frac{J}{R}\tanh Rz;\ R\equiv\frac{d_0^*}{\delta_0^*};\ J\equiv\frac{B_0^*d_0^*}{U_0^{*2}}, \tag{3.3}$$

where δ_0^* is the (dimensional) half-depth of the background buoyancy layer with half-difference B_0^* and J is the bulk Richardson number. This is an extension of the Holmboe model (Holmboe, 1960), which has $R=1$ and is attractive because the stability boundary can be found analytically (Miles, 1961). It is close to the self-similar error function profile expected for a diffusing stratified shear layer when $Pr=R^2$ (Smyth et al., 1988). It is important to note that these profiles are not steady solutions of the viscous Boussinesq equations, but we make the ‘frozen flow’ approximation (Smyth and Carpenter, 2019) which is valid when $\sigma\gg\frac{1}{Re}$. This inequality is not always satisfied by the instabilities we find, as discussed in section 3.3.4.

The gradient Richardson number Ri_g, defined as

$$Ri_g(z)\equiv\frac{\mathrm{d}B/\mathrm{d}z}{(\mathrm{d}U/\mathrm{d}z)^2}=J\frac{\operatorname{sech}^2 Rz}{\operatorname{sech}^4 z}, \tag{3.4}$$

for the Hazel model flow which means (for this particular flow) that at the centreline, $Ri_g(0)=J$. For $R\leq\sqrt{2}$, J is the minimum of Ri_g, for $\sqrt{2}<R<2$, there are two minima of $Ri_g < J$ either side of local maximum $z = 0$, and for $R \geq 2$, $Ri_g \to 0$ as $z \to \infty$ and $z = 0$ is a global maximum (Alexakis, 2005). From the Miles-Howard theorem, we then deduce that inviscid HWI at arbitrarily large J is only possible when $R \geq 2$. In fact, Alexakis (2007) showed that HWI only exists at all for $R \geq 2$, despite the possibility of instability at $J > 1/4$ when $\sqrt{2} < R < 2$.

The solution of (3.2) is performed using a MATLAB code from Smyth and Carpenter (2019). The method is to construct a large matrix eigenvalue problem, using evenly spaced finite differences. This is a mature code, and additionally the existence of viscous Holmboe was confirmed in DNS of the Boussinesq equations at finite Re and $Pr = 1$ (see chapter 2).The boundary conditions are that $\frac{\partial \hat{w}}{\partial z} = \frac{\partial \hat{b}}{\partial z} = 0$, i.e. frictionless, insulating boundaries, at $z = \pm L_z$, although all of the instabilities we discuss here are centred around the shear layer, and changing the boundary conditions would not qualitatively affect the results. All linear stability results are found using 768 finite difference points in the vertical direction, except for the $L_z = 20$ case which used 1024 points, and the figures are generated from a 48×48 grid of calculated growth rates.

3.3 Linear stability analyses

Figure 3.1 shows a typical example of the viscous Holmboe instability (VHI). There is a clear distinction between those unstable modes with zero phase speed, which we identify as KHI, and the modes with non-zero phase speed, which we identify as VHI. Although the existence of unstable modes at $R = 1$ with non-zero phase speed was unknown before the work in chapter 2, the diagram bears a striking resemblance to the classic stability diagrams for inviscid HWI for a piecewise linear profile with a density discontinuity (Holmboe, 1962, figure 7) and the Holmboe model with $R > 2$ (Hazel, 1972, figure 8). Crucially, above $J = 0.25$ on this diagram, the gradient Richardson number of the flow is everywhere greater than one quarter, and so we expect stability as $Re \to \infty$. In the inviscid case, as J is increased the dominant KHI mode and a subdominant KHI mode converge and bifurcate into the pair of HWI modes, with opposite phase speeds. In the viscous case, the regions of the two instabilities overlap slightly and there is no clean bifurcation from one to the other. The remainder of this section will explore how the structure of stability diagrams like figure 3.1 change as various parameters are varied.

Figure 3.2 shows typical eigenmodes of the spanwise vorticity. With $R = 1$, i.e. a density interface as wide as the shear layer, no critical layer exists. With $R = 3$, the eigenmode is virtually indistinguishable from the $Re \to \infty$ case, and a critical layer is present and clearly manifests itself within the spatial structure of the mode. Both of these modes have an

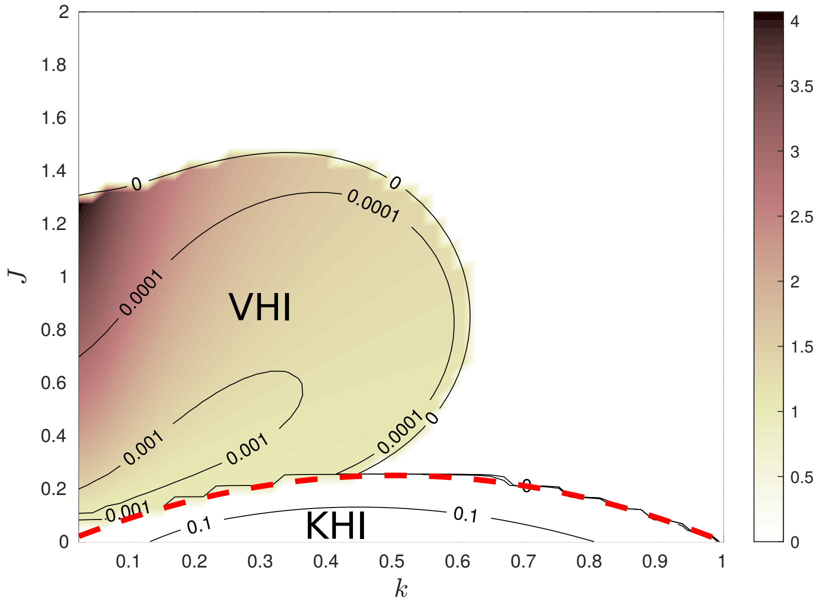

Fig. 3.1 Stability diagram for the Hazel model flow profile as defined in (3.3) with $R = 1$, $Re = 500$, $Pr = 1$, with boundaries at $z = \pm L_z = \pm 15$. The contours show the growth rate of two-dimensional normal mode perturbations of wavenumber k, at bulk Richardson number J. The colours show the phase speed. The lower region, up to $J = 0.25$, is KHI with zero phase speed. The upper lobe is viscous Holmboe instability (VHI), with non-zero phase speed. The dashed line shows the analytic stability boundary $J = k(1-k)$ for an unbounded domain in the inviscid limit (Miles, 1961). In this, and all the stability diagrams in this chapter, a waviness is apparent near stability boundaries. This is a common problem in such stability diagrams (Hogg and Ivey, 2003; Smyth and Winters, 2003; Carpenter et al., 2010b, 2013), and is associated with interpolating near sharp changes of gradient in contour plots.

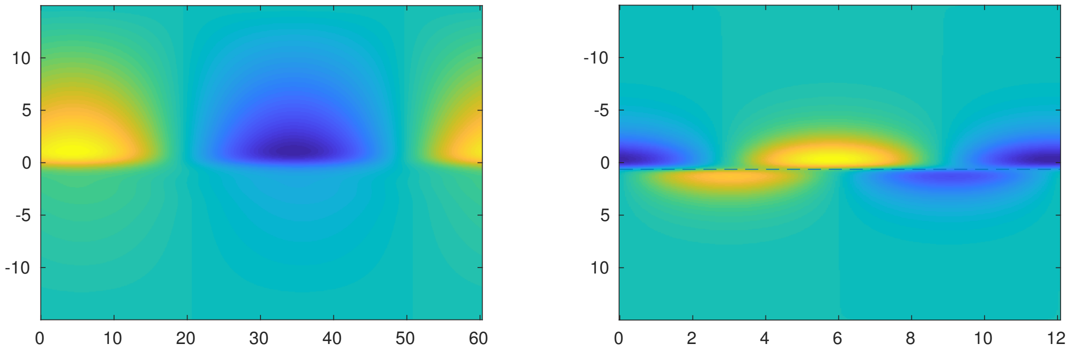

Fig. 3.2 Vorticity field for the most unstable viscous Holmboe instability (VHI) mode for $R = 1$ ($J = 0.2128$, $k = 0.1042$, left) and $R = 3$ ($J = 0.8085$, $k = 0.5208$, right). In the latter case, a critical layer exists at $z = 0.63437$ and is marked with a dashed line.

Re	R	Pr	L_z	σ^{max}	c_r^{max}	J^{max}	k^{max}	Figure
500	1	1	15	0.002031	1.114	0.21277	0.10417	1
500	1	1	10	0.0019489	1.1152	0.21277	0.0625	3a
500	1	1	20	0.0020869	1.1363	0.12766	0.041667	3b
500	1	0.7	15	0.0027958	1.1185	0.21277	0.10417	4a
500	1	7	15	0.00056834	1.2536	0.17021	0.020833	4b
500	0.5	0.25	15	0.0003781	1.557	0.12766	0.041667	5a
500	1.5	2.25	15	0.0032918	1.0156	0.29787	0.10417	5b
500	2	4	15	0.0033963	0.88215	0.38298	0.125	5c
500	3	9	15	0.031314	0.56129	0.80851	0.52083	5d
5.5	1	1	15	0.0014049	1.4289	0.29787	0.125	6
6	1	1	15	0.0025824	1.2608	0.21277	0.125	6
7	1	1	15	0.0039878	1.2708	0.25532	0.14583	6
10	1	1	15	0.0067811	1.2525	0.25532	0.14583	6
15	1	1	15	0.0092699	1.2498	0.34043	0.1875	6
20	1	1	15	0.01023	1.2336	0.34043	0.1875	6
25	1	1	15	0.010546	1.2515	0.34194	0.175	6
30	1	1	15	0.010542	1.2334	0.35806	0.1875	6
40	1	1	15	0.01	1.2446	0.34043	0.16667	6
100	1	1	15	0.0069558	1.1762	0.25532	0.125	6
200	1	1	15	0.0044792	1.1263	0.21277	0.10417	6
400	1	1	15	0.0025701	1.1279	0.17021	0.0625	6
1000	1	1	15	0.0011049	1.1183	0.17021	0.0625	6
2000	1	1	15	0.00057664	1.0722	0.13226	0.025	6
4000	1	1	15	0.0002994	1.0854	0.13226	0.0125	6
10000	1	1	15	0.00012168	1.0827	0.13226	0.0125	6

Table 3.1 The various parameters used for the linear stability diagrams, as well as the maximum growth rate σ^{max} of viscous Holmboe instability (VHI) for each set of parameters, and the phase speed c_r^{max}, wavenumber k^{max} and bulk Richardson number J^{max} at which they occur.

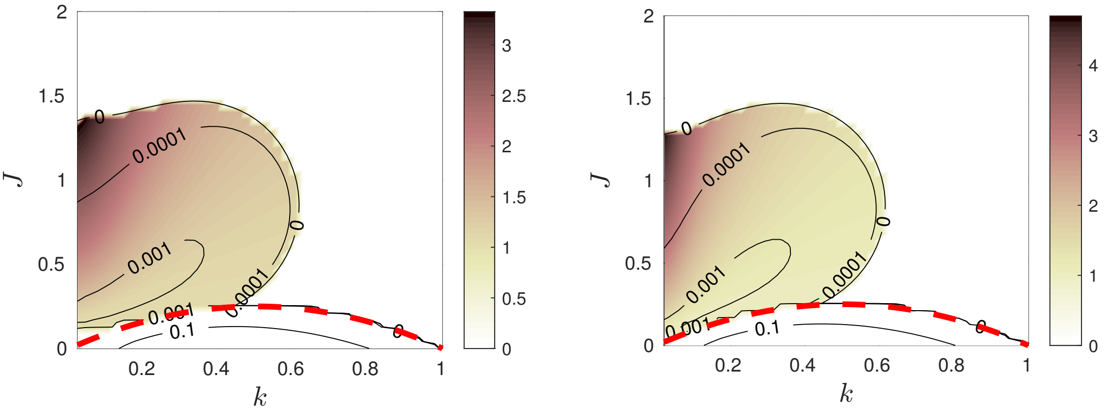

(a)

(b)

Fig. 3.3 As for figure 3.1, but with $L_z = 10$ (a) and $L_z = 20$ (b).

equivalent mode associated with the complex conjugate eigenvalue, which is identical except for a reflection in the centreline. In the $R = 1$ case, we also note that the growth rate is maximised at a much lower wavenumber.

Table 3.1 shows the full list of parameters for which stability diagrams were produced. For each diagram, we find the maximum growth rate for VHI, i.e. the maximum of σ such that the phase speed c_r is non-zero, maximised over the discretised values of k and J. Since the grids are relatively coarse, the values will not be the true maxima as no optimisation algorithm has been employed, but they give a strong indication of the trend.

3.3.1 Effects of domain height

The instabilities we study, KHI and HWI, were originally derived as solutions to the Taylor-Goldstein equation in an unbounded domain. There are several ways to approximate a domain of infinite height numerically, but we choose the simplest, which is to use a domain of sufficiently large, but finite, height. How large is sufficient is an important question, as a very large domain is computationally inefficient. Certainly as the height gets small compared with the wavelength of the instabilities we expect the results to change dramatically, and Hazel (1972) noted how the diagrams always differ from the analytic, unbounded results at low wavenumbers. Figure 3.3 shows the same diagram as figure 3.1, but at a smaller (figure 3.3a) and a larger (figure 3.3b) domain height. Though the results are slightly different, qualitatively they are very similar, especially for $L_z = 20$, with $L_z = 10$ showing more instability at low wavenumbers. The maximum growth rate of the VHI region is $\sigma = 1.9489 \times 10^{-3}$ for

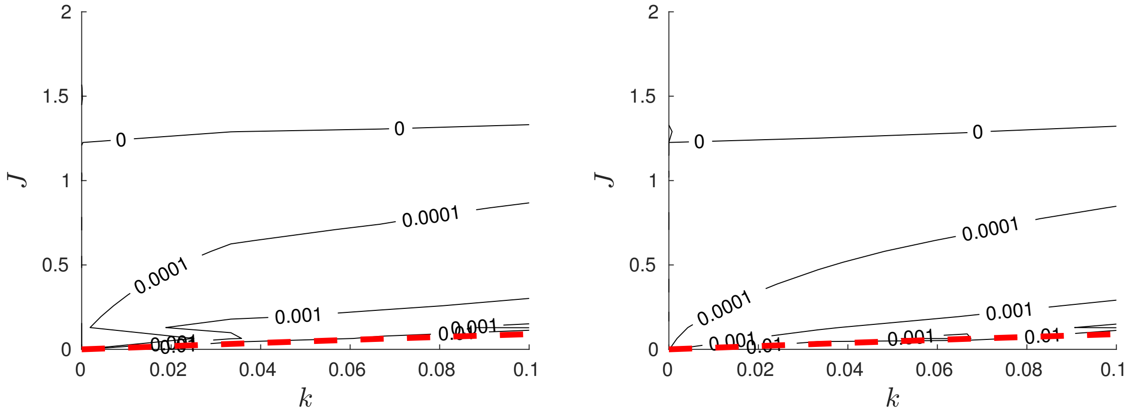

(a) (b)

Fig. 3.4 Contours of growth rate at low wavenumber for (a) $L_z = 20$ and (b) $L_z = 40$. An increased vertical resolution of 1024 was used. In this case the colour for phase speed is omitted as this is not well-defined at $k = 0$.

$L_z = 10$ and $\sigma = 2.0869 \times 10^{-3}$ for $L_z = 20$, compared with $\sigma = 2.0310 \times 10^{-3}$ for $L_z = 15$, suggesting that $L_z = 15$ is sufficient to capture the behaviour in which we are interested.

It is interesting to observe that the region of instability appears to extend to nonzero J at $k = 0$. This is expected for small domain height (Hazel, 1972), but is counter-intuitive and perhaps non-physical as $L_z \to \infty$. To investigate this, figure 3.4 shows the low-wavenumber portion of the stability diagram at $L_z = 20$ and $L_z = 40$. In both cases the stability boundary itself appears to be at $J > 1$ at $k = 0$, but the next contour of $\sigma = 0.0001$ is clearly retreating at $k = 0$ as the domain height is increased. This suggests that the stability boundary itself may be a numerical artifact.

3.3.2 Effects of Prandtl number

Figure 3.5 shows the effect on the stability diagram of varying the Prandtl number. For $Pr = 0.7$ (characteristic of thermally stratified air), we find a maximum growth rate of $\sigma = 2.7958 \times 10^{-3}$, and for $Pr = 7$ (a typical value for thermally stratified water) of $\sigma = 5.6834 \times 10^{-4}$, compared with $\sigma = 2.0310 \times 10^{-3}$ for $Pr = 1$. Therefore, decreasing the diffusion of buoyancy seems to have a stabilising effect on VHI. In contrast, the KHI at the bottom of the figure is virtually unchanged as Pr is varied by an order of magnitude, which reinforces the idea that KHI is produced by the shear alone. Jones (1977) found strong instability at very low Pr, but we believe this to be a different effect.

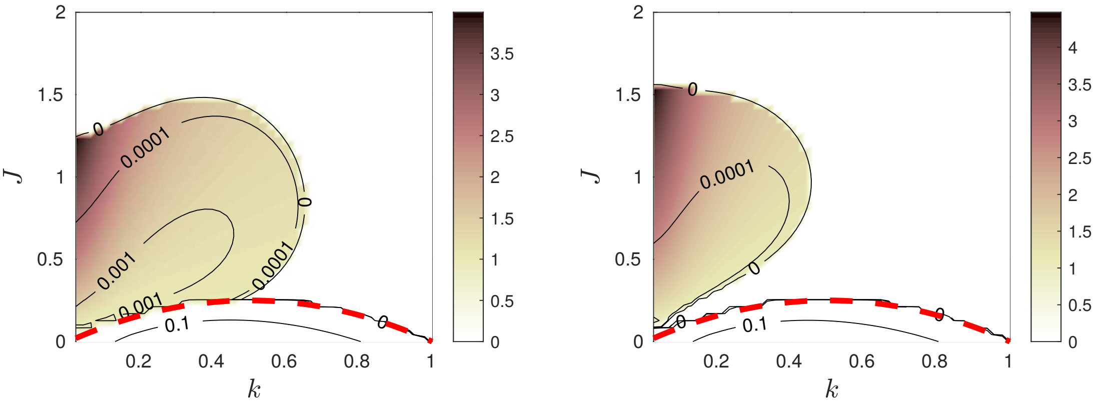

Fig. 3.5 As for figure 3.1, but with $Pr = 0.7$ (left) and $Pr = 7$ (right).

Henceforth, we give results using $Pr = R^2$, as proposed by Smyth et al. (1988). Despite the fact that the instability seems to be destabilised when Pr is reduced, it is also stabilised when R is decreased, as we shall see.

3.3.3 Effects of R

So far, the results we have presented have concentrated on $R = 1$, the original Holmboe model. However, in the inviscid limit, HWI exists only for $R > 2$ (Alexakis, 2007). Figure 3.6 shows the stability diagram at $Re = 500$ over a range of R, with $Pr = R^2$. All diagrams show a region of instability with non-zero phase speed, which we identify as VHI. In the case $R = 3$, the diagram is very similar to the classical diagram of an inviscid fluid (Hazel, 1972). The unstable region above the usual band, at low wavenumbers, has $c_r > 1$, so there is no critical layer. As $R \to 2$ from above, the inviscid results suggest that the band should narrow to a line (Alexakis, 2005), but instead we see a significant region of instability. In the diagrams for $R = 1.5$ and $R = 2$, a second band of instability is observed above the first, with reduced phase speed, and we conjecture that this may be connected with the higher Holmboe modes. This has not been investigated further, as the growth rate here is vanishingly small.

In all cases, although it is not clear from the truncated diagrams, the instability is suppressed at large k by viscosity. This is in contrast to the inviscid limit, which has instability at arbitrarily large k and J. It is only in this large k limit that the wave interaction arguments can be made rigorous.

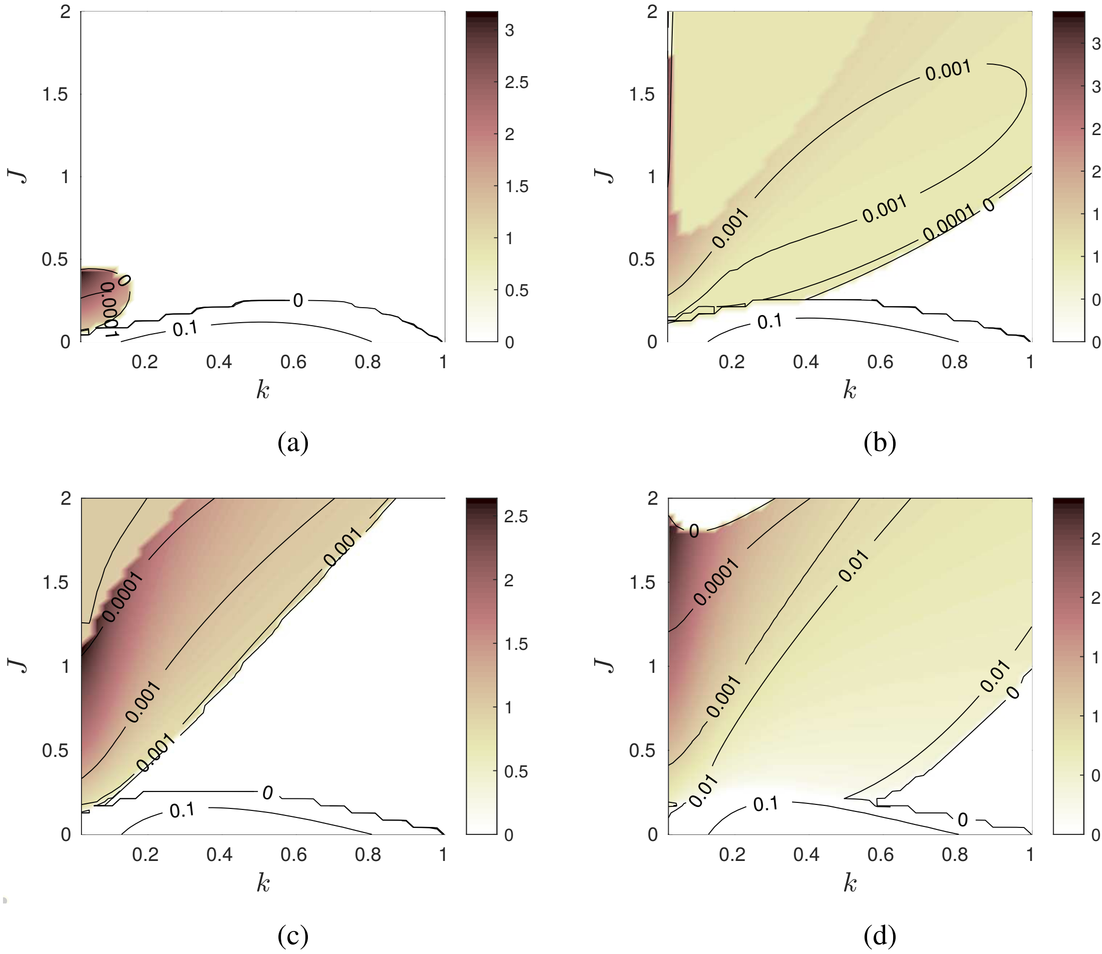

(a) (b) (c) (d)

Fig. 3.6 As for figure 3.1, but with (a) $R = 0.5$, $Pr = 0.25$, (b) $R = 1.5$, $Pr = 2.25$, (c) $R = 2$, $Pr = 4$, (d) $R = 3$, $Pr = 9$. Only the last of these would exhibit HWI at $Re = \infty$.

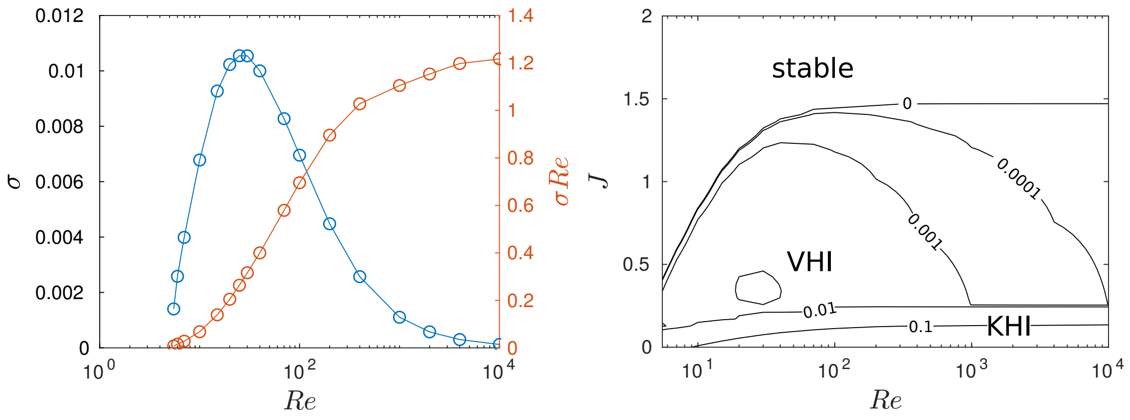

(a) (b)

Fig. 3.7 (a) The growth rate σ (left axis) and relative growth rate σRe (right axis), maximised over k and J, for VHI at $R = 1$, $Pr = 1$, as Re varies. (b) Growth rate against J and Re, maximised over k, for $R = 1$ and $Pr = 1$. The band at the bottom of the figure is KHI, destabilised as Re increases. The upper region with $J \gtrsim 1/4$ is VHI, clearly stabilised as Re increases.

3.3.4 Effects of Reynolds number

The Miles-Howard theorem tells us that VHI at $R = 1$ must disappear for $J > 1/4$, in the inviscid limit $Re \to \infty$. This leaves many possibilities: 1) the stability boundary could retreat below $J = 1/4$; 2) width of the unstable region in the k direction could vanish; or 3) the growth rates could vanish but the region remain a finite size. There may or may not be some finite Re above which VHI does not exist. It is also important to ask at what value of Re the growth of the instability is the fastest, or indeed the relative growth rate compared with the diffusion of the background profile.

The growth rate is maximised between $Re = 25$ and $Re = 30$, with value $\sigma \approx 0.0105$. The relative growth rate σRe, which is required to be large compared with unity for a physically relevant instability (Smyth and Carpenter, 2019), was found to increase with Re (at least until $Re = 10000$), which is a curious result, since it means that despite the growth rate being maximised at a very low value of Re, in practice we are more likely to observe the instability at much higher Re.

The critical Reynolds number Re_c for the viscous Holmboe instability at $R = 1$, $Pr = 1$, below which there is no instability except KHI, was found to be $Re = 4.615$. At criticality, the instability appears at $J = 0.25$ and $k = 0.12$. This is in contrast with KHI, which at $J = 0$ was found to have $Re_c = 0$ (Betchov and Szewczyk, 1963). In that case, viscosity has a purely stabilising effect. Figure 3.7 shows how the growth rate varies with Re.

Asymptotic behaviour at high *Re*

The fact that some of the VHI do not have a critical layer ($c_r^{max} > 1$ in Table 1) suggests a regular perturbation analysis may be sufficient to capture the effect of high but finite *Re*. Defining a perturbation parameter $\varepsilon := 1/Re \ll 1$, we may rewrite (3.2) as

$$\mathscr{L}_0(c)\begin{pmatrix}\hat{w}\\ \hat{b}\end{pmatrix} = \varepsilon\mathscr{L}_1\begin{pmatrix}\hat{w}\\ \hat{b}\end{pmatrix}, \tag{3.5}$$

where we have defined linear operators

$$\mathscr{L}_0(c) := \begin{pmatrix}(U-c)\left(\partial_z^2-k^2\right)-U_{zz} & -ik\\ \frac{1}{ik}B_z & (U-c)\end{pmatrix} \tag{3.6}$$

and

$$\mathscr{L}_1 := \frac{1}{ik}\begin{pmatrix}\left(\partial_z^2-k^2\right)^2 & 0\\ 0 & \frac{1}{Pr}\left(\partial_z^2-k^2\right)\end{pmatrix}. \tag{3.7}$$

Adopting the expansions

$$\begin{pmatrix}\hat{w}\\ \hat{b}\end{pmatrix} = \begin{pmatrix}\hat{w}_0\\ \hat{b}_0\end{pmatrix} + \varepsilon\begin{pmatrix}\hat{w}_1\\ \hat{b}_1\end{pmatrix} + O(\varepsilon^2),$$
$$c = c_0 + \varepsilon c_1 + O(\varepsilon^2),$$

(keeping k fixed), then

$$\mathscr{L}_0(c) = \mathscr{L}_0(c_0) + \varepsilon c_1\mathscr{L}_0' + O(\varepsilon^2) \tag{3.8}$$

where

$$\mathscr{L}_0' := \frac{\partial\mathscr{L}_0}{\partial c} = \begin{pmatrix}-\left(\partial_z^2-k^2\right) & 0\\ 0 & -1\end{pmatrix}. \tag{3.9}$$

Inserting these expansions into (3.5), we have

$$\mathscr{L}_0(c_0)\begin{pmatrix}\hat{w}_0\\ \hat{b}_0\end{pmatrix} + \varepsilon\mathscr{L}_0(c_0)\begin{pmatrix}\hat{w}_1\\ \hat{b}_1\end{pmatrix} + \varepsilon c_1\mathscr{L}_0'\begin{pmatrix}\hat{w}_0\\ \hat{b}_0\end{pmatrix} = \varepsilon\mathscr{L}_1\begin{pmatrix}\hat{w}_0\\ \hat{b}_0\end{pmatrix} + O(\varepsilon^2). \tag{3.10}$$

At leading order, the inviscid Taylor-Goldstein equation is recovered,

$$\mathscr{L}_0(c_0)\begin{pmatrix}\hat{w}_0\\ \hat{b}_0\end{pmatrix} = 0, \tag{3.11}$$

which by the Miles-Howard theorem has only wavelike solutions $c_0 \in \mathbb{R}$ when $R = 1$ and $J > 1/4$. In this case, the diagonal elements of $\mathscr{L}_0(c)$ are real and the off-diagonal elements are purely imaginary, so that for a solution we must have $\arg \hat{b}_0 = \arg \hat{w}_0 \pm \pi/2$ in the absence of a critical layer. Without loss of generality, we may choose the phase so that $\hat{w}_0$ is real and $\hat{b}_0$ is purely imaginary.

With an inner product on the space of vectors

$$\left\langle \begin{pmatrix} w_1 \\ b_1 \end{pmatrix}, \begin{pmatrix} w_2 \\ b_2 \end{pmatrix} \right\rangle := \int_{L_z}^{L_z} (w_1^* w_2 + b_1^* b_2)\,\mathrm{d}z, \tag{3.12}$$

we may define the adjoint operator $\mathscr{L}_0^\dagger(c)$ to $\mathscr{L}_0(c)$ via

$$\left\langle \begin{pmatrix} w_1 \\ b_1 \end{pmatrix}, \mathscr{L}_0(c) \begin{pmatrix} w_2 \\ b_2 \end{pmatrix} \right\rangle = \left\langle \mathscr{L}_0^\dagger(c) \begin{pmatrix} w_1 \\ b_1 \end{pmatrix}, \begin{pmatrix} w_2 \\ b_2 \end{pmatrix} \right\rangle, \tag{3.13}$$

which gives

$$\mathscr{L}_0^\dagger(c) := \begin{pmatrix} \left(\partial_z^2 - k^2\right)(U-c)U_{zz} & -\frac{1}{ik} B_z \\ ik & (U-c) \end{pmatrix}. \tag{3.14}$$

The existence of a non-trivial solution to (3.11) implies a non-trivial solution to

$$\mathscr{L}_0^\dagger(c_0) \begin{pmatrix} \hat{w}_0^\dagger \\ \hat{b}_0^\dagger \end{pmatrix} = 0, \tag{3.15}$$

which is the adjoint eigenfunction. Again, we can choose $\hat{w}_0^\dagger$ to be real and $\hat{b}_0^\dagger$ to be imaginary.

The $O(\varepsilon)$ terms in (3.10) give

$$\mathscr{L}_0(c_0) \begin{pmatrix} \hat{w}_1 \\ \hat{b}_1 \end{pmatrix} = \mathscr{L}_1 \begin{pmatrix} \hat{w}_0 \\ \hat{b}_0 \end{pmatrix} - c_1 \mathscr{L}_0' \begin{pmatrix} \hat{w}_0 \\ \hat{b}_0 \end{pmatrix}, \tag{3.16}$$

so taking the inner product with the adjoint eigenfunction, we have

$$\left\langle \begin{pmatrix} \hat{w}_0^\dagger \\ \hat{b}_0^\dagger \end{pmatrix}, \mathscr{L}_0(c_0) \begin{pmatrix} \hat{w}_1 \\ \hat{b}_1 \end{pmatrix} \right\rangle = \left\langle \begin{pmatrix} \hat{w}_0^\dagger \\ \hat{b}_0^\dagger \end{pmatrix}, \mathscr{L}_1 \begin{pmatrix} \hat{w}_0 \\ \hat{b}_0 \end{pmatrix} \right\rangle - c_1 \left\langle \begin{pmatrix} \hat{w}_0^\dagger \\ \hat{b}_0^\dagger \end{pmatrix}, \mathscr{L}_0' \begin{pmatrix} \hat{w}_0 \\ \hat{b}_0 \end{pmatrix} \right\rangle. \tag{3.17}$$

The left-hand side of this equation is zero by construction, and so

$$c_1 = \frac{\left\langle \begin{pmatrix} \hat{w}_0^\dagger \\ \hat{b}_0^\dagger \end{pmatrix}, \mathscr{L}_1 \begin{pmatrix} \hat{w}_0 \\ \hat{b}_0 \end{pmatrix} \right\rangle}{\left\langle \begin{pmatrix} \hat{w}_0^\dagger \\ \hat{b}_0^\dagger \end{pmatrix}, \mathscr{L}_0' \begin{pmatrix} \hat{w}_0 \\ \hat{b}_0 \end{pmatrix} \right\rangle}. \tag{3.18}$$

Observe from (3.7) and (3.9) that $\mathscr{L}_1$ and $\mathscr{L}_0'$ are purely imaginary and real respectively. By our choice of phase it is clear that the numerator is therefore imaginary and the denominator real, so c_1 is purely imaginary. It can be similarly shown that c_2 is real so the next contribution to the growth rate is at $O(1/Re^3)$. We further observe that both $\mathscr{L}_1$ and $c_1\mathscr{L}_0'$ are purely imaginary, so from (3.16) we deduce that $\hat{w}_1$ and $\hat{b}_1$ are purely imaginary and real respectively, the opposite situation to $\hat{w}_0$ and $\hat{b}_0$.

We compute c_1, and thus the growth rate of the instability as Re becomes large $\sigma = -ikc_1/Re + O(1/Re^3)$, using (3.18) as follows. First, we make an initial guess of c_0 from the real part of c from a numerical linear stability analysis at $Re = 10000$. Secondly, we use this approximate c_0 in the inverse iteration eigenvalue algorithm to solve both (3.11) and (3.15). Finally, we directly evaluate (3.18) using a trapezoidal quadrature rule for the inner products.

The results for two sample parameter values are shown in figure 3.8a. Figure 3.8b shows calculated zeroth- and first-order modes. We thus see that the viscous Holmboe modes are a destabilisation of a stable, propagating mode in the inviscid limit. Viscosity acts to break the exact $\pi/2$ phase difference between the vertical velocity and the buoyancy modes. The fact that VHI varies smoothly between modes with and without critical layers, in particular in figure 3.6c, suggests this regular perturbation analysis will extend to the case where a critical layer exists, and that the critical layer is not important to the dynamics.

3.4 Nonlinear evolution

Smyth and Peltier (1990) showed that at low Reynolds numbers, the linear evolution of HWI is insufficiently fast to overcome the diffusion of the background flow. This leads to the possibility that VHI, for which the growth rates are always small, never physically manifests when the background flow is allowed to diffuse. We consider the nonlinear evolution, which allows us to see whether the viscous Holmboe instability develops the classic counter-propagating vortices of HWI. We use the same DNS code as in chapter 2 to solve the full Boussinesq equations, which is pseudospectral in the streamwise direction and

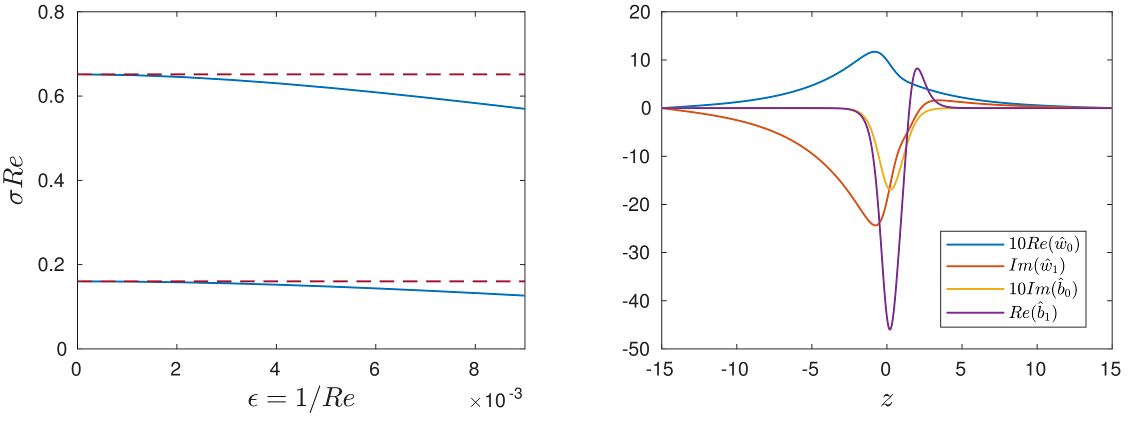

(a) (b)

Fig. 3.8 (a) Asymptotic (dashed) and numerical (solid) values of growth rate for VHI at $J = 1$, $k = 0.5$ (lower) and $J = 0.5$, $k = 0.25$ (upper). (b) Modes for the $J = 0.5$, $k = 0.25$ case. The zeroth order modes have been scaled for clarity. In both figures, $R = 1$, $Pr = 1$ and $L_z = 15$, corresponding to figure 3.1.

utilises finite differences in the vertical. In the present case, the background flow is allowed to diffuse.

Here we present the results of two direct numerical simulations (restricted to two dimensions) with $R = 1.5$, a case for which no HWI is predicted in the inviscid limit. We take $Re = 4000$, a compromise between maximising the relative growth rate (see section 3.3.4) and minimising the spatial resolution. We chose a domain width of $L_x = 20$, which permits multiple unstable modes.

Large-amplitude random initial perturbations were used to simulate the effects of a noisy oceanic or atmospheric environment. Using initial conditions matching the most unstable modes would necessarily have demonstrated some nonlinear behaviour reminiscent of the respective instabilities with sufficiently large initial amplitude. The intention here, instead, is to see whether VHI is sufficiently fast-growing that it can manifest in unfavourable, generic conditions.

Figure 3.9 shows the results of a calculation with $J = 0.1$, for which we expect a Kelvin-Helmholtz instability to develop to finite-amplitude. A linear stability analysis predicts exponential growth rates of $\sigma = 0.1244$ and $\sigma = 0.0981$ for mode 1 and mode 2 disturbances ($k = \pi/10$ and $k = \pi/5$) respectively, in both cases with zero phase speed. We use a relatively large initial perturbation of random noise in low wavenumber Fourier and Hermite modes, which, along with the comparable growth rates for the two unstable modes, leads to an incoherent, but nevertheless recognisable, Kelvin-Helmholtz billow. At the large Re studied, this rapidly breaks down into turbulence, and significant mixing is achieved, although it is important to remember that this DNS is restricted to two dimensions, and so the specific characteristics of the mixing are likely to be unphysical.

Figure 3.10 shows the same calculation with $J = 0.67$, which maximises the growth rate for VHI at this wavenumber. Again, both modes 1 and 2 are unstable, with growth rates $\sigma = 4.1121 \times 10^{-4}$ and $\sigma = 1.7012 \times 10^{-4}$ respectively, and phase velocities $c_r = \pm 1.0211$ and $c_r = \pm 1.0056$. Since the phase speeds are greater than 1, no critical layer exists for these instabilities. In this case, the relative growth rate clearly does not satisfy $\sigma Re \gg 1$, so we require a large initial perturbation to trigger significant instability. The strong asymmetry of this random perturbation means that a Holmboe 'wave' is apparent only on one side of the interface. Despite the lack of a critical layer, a 'cusped wave' very reminiscent of classic HWI (Alexakis, 2009; Salehipour et al., 2016) is apparent, and grows large enough for a clear vortex to be apparent. This vortex is responsible for some mixing, which can be observed when comparing the long time vorticity distribution above the interface, where the vortex exists, to below, where no strong VHI was triggered. However, this mixing is relatively weak compared with the diffusion of the background profile. It is difficult to define a speed precisely for the nonlinear wave, but it appears to be close to 1. Both the background flow velocity at the level of the vortices and the phase velocity of the linear instability are also approximately equal to 1. Animations of both evolving flows are available as supplementary materials.

3.5 Discussion and Conclusions

In this chapter, we have described a new, inherently viscous instability and have demonstrated that it shares many of the characteristic features of the classic, inviscid Holmboe wave instability, namely manifesting as a propagating vortex on either side of the mixing layer and appearing to be caused by the interaction of internal gravity waves on a shear interface. Since it exists in regions of parameter space where no instability is predicted in the inviscid limit, we term it the viscous Holmboe instability, or VHI. The instability we have described is distinct from the 'viscous Holmboe wave instability' found by Eaves and Caulfield (2017) in plane Couette flow, which required non-slip and non-penetration effects in the presence of a rigid boundary, whereas we have shown that boundaries only weakly affect the instability, and the VHI discussed here is truly an instability of a stratified shear layer. Despite the similarities to inviscid HWI, it has significant differences from the classical case: it exists when the density interface is *not sharp* compared with the shear layer; it can have a phase speed greater than the maximum fluid velocity; and it is *destabilised* by viscosity. When there is no critical layer, a simple perturbation analysis shows that the VHI arises by viscosity

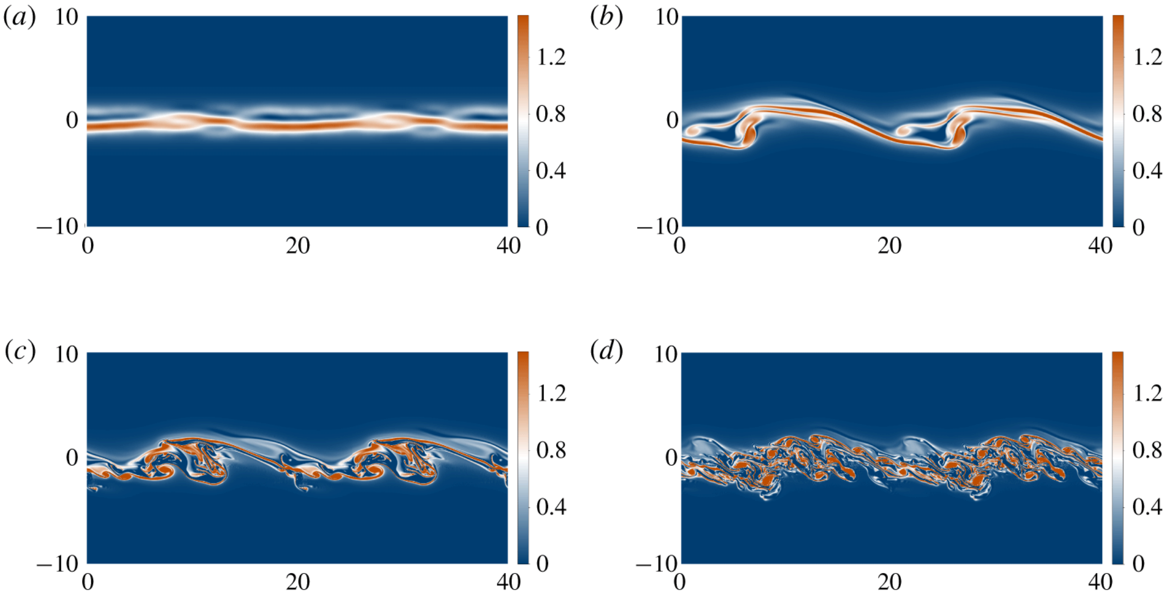

Fig. 3.9 The total vorticity field of a two-dimensional nonlinear simulation of the Boussinesq equations at $Re = 4000$, $Pr = 2.25$, $L_x = 20$, $L_z = 10$ and $J = 0.1$. The initial state is a background field with $R = 1.5$, plus a perturbation of random noise in the first sixth of the horizontal Fourier modes, and the first five Hermite polynomials in the vertical. Two domain widths are shown horizontally. (a) $t = 0$, showing the random initial conditions. (b) $t = 20$, showing the Kelvin-Helmholtz billow that has begun to develop. (c) $t = 40$, showing that the billow has saturated and is starting to break down. (d) $t = 60$, showing that the KHI has led to (two-dimensional) turbulence. An animation of the evolving flow is available as supplementary material.

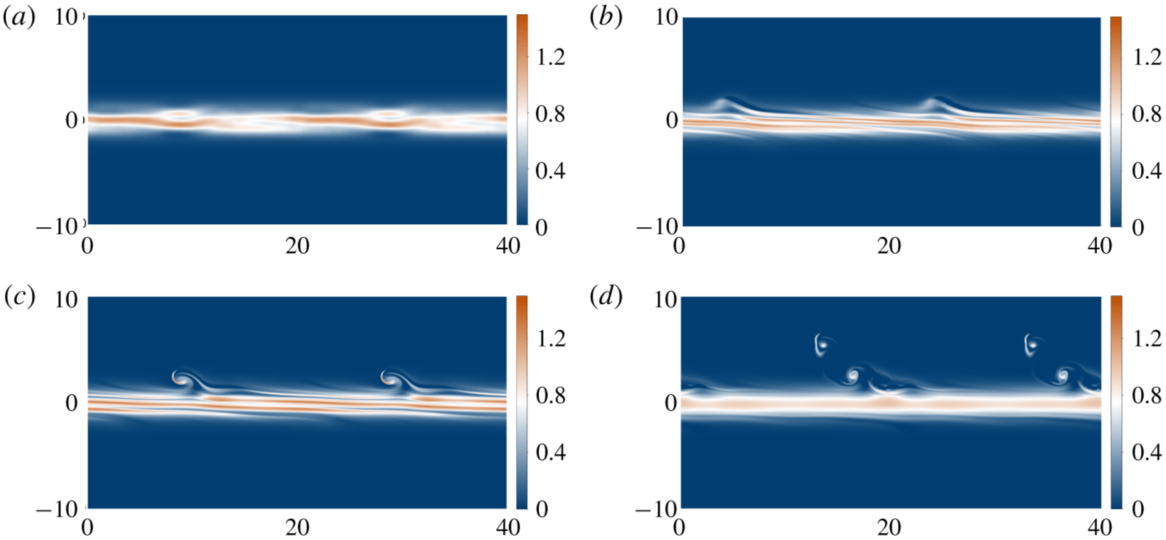

Fig. 3.10 As for figure 3.9, but with $J = 0.4355$. (a) $t = 0$, showing the random initial conditions. (b) $t = 20$, showing that a ‘cusped wave’ is apparent, characteristic of HWI at finite-amplitude. (c) $t = 35$, showing that a leftwards-propagating vortex is now visible above the shear layer. (d) $t = 110$, showing that the vortex has weakened as the mixing layer diffuses away. An animation of the evolving flow is available as supplementary material.

disrupting the perfectly out-of-phase velocity and buoyancy components of the neutrally stable inviscid limit. Our work has made the ‘frozen flow’ approximation that requires σ to be large compared with $1/Re$ for the instability to grow quickly compared with the diffusion of the background profile, but we did not find this to be the case. Indeed, our perturbation analysis shows that $\sigma \sim 1/Re$ as $Re \to \infty$. Numerically, we find that σ is small compared with $1/Re$ when $Re \lesssim 10^2$, despite the fact that σ is maximised for $Re \approx 25$ and only just rises above $1/Re$ for $Re \gtrsim 10^3$. This leads to the curious situation that although this is an instability which requires viscosity to exist, the effect of the instability relative to the diffusion of the background flow appears to be greater as Re is increased.

This work is a study of how viscosity affects the Holmboe wave instability as certain parameters are varied. There are many possible extensions which have been examined for (classic) HWI, including considering the effects of compressibility (Witzke et al., 2015), surface tension (Pouliquen et al., 1994), and relaxing the Boussinesq approximation (Umurhan and Heifetz, 2007; Churilov, 2019). We briefly investigated the possibility that the higher Holmboe modes described by Alexakis (2005, 2007, 2009) are also destabilised by viscosity at low R, and did indeed find a further band of instability with very small growth rates. Our work has been entirely restricted to two dimensions. Though this is a common assumption when studying linear instabilities of shear flows, there is no physical basis for this, and indeed we would fully expect to see the fastest growing mode being three-dimensional in some regions of parameter space, based on the results of Smyth and Peltier (1990). A third dimension would also significantly affect the nonlinear evolution of the instability at high Re.

Despite the lack of a sharp density interface relative to the shear layer for the parameters for which we have found instability, we would certainly still expect internal gravity waves to be present on the interface. There is no reason we are aware of, *a priori*, to think that these could not resonate with the vorticity waves to cause instability. The wave resonance descriptions of stratified shear instabilities have been mainly qualitative, except in the cases of piecewise constant density and vorticity profiles, which would be physically inconsistent at finite viscosity. Recent attempts to analyse the components of resonances (Carpenter et al., 2010b; Eaves and Balmforth, 2019) and to understand better the dynamics of the resonant system (Heifetz and Guha, 2018, 2019) have relied on analysis which requires perturbations to be inviscid, and these certainly would not apply in the low Re regimes we have described. Though the theory of wave resonance has given useful insight in many situations, it is clearly not the full picture. One major outstanding question is how the Miles-Howard criterion may relate to the wave resonance picture. Baines and Mitsudera (1994) give an argument from critical layer theory, though the authors themselves admit that this gives neither a necessary nor sufficient criterion for stability.

Most of the unstable regions of the viscous Holmboe instability for $R \leq 2$ have $|c_r| > 1$, so there is no critical layer. Therefore, Lindzen's wave over-reflection hypothesis for the mechanism of stratified shear instabilities, as well as other interpretations based on the existence of a critical layer, such as the wave-particle interaction described by Churilov (2019), cannot apply. This is in contrast with the viscous instability described by Miller and Lindzen (1988), in which the viscosity was thought to enable over-reflection at the critical layer. As discussed by Smyth and Peltier (1989), it could be possible that the instability is associated with over-reflection of a wave with a different phase speed, which therefore could itself have a critical layer, but this makes an intuitive explanation much harder. Since the wave over-reflection theory is not a predictive explanation of the instability in this case, it does not seem useful here, though it has certainly proven important in many other circumstances.

Under carefully controlled parameters, we have been able to show significant nonlinear growth of the viscous Holmboe instability at $R = 1.5$ and $Re = 4000$, from initial noise, leading to secondary instabilities and transition to disorder. This primary instability has no critical layer. Nevertheless, most of the regions of instability we have studied, with $R < 2$, have much lower growth rates. We conclude that the viscous Holmboe instability is unlikely to be particularly significant in physical processes. In addition to this, for typical values of Prandtl number in the atmosphere ($Pr \approx 0.7$) we see very small growth rates and for typical values of $Pr \approx 7$ in the oceans, we see the full classical HWI, since in this case R is usually large.

Despite these caveats, we have demonstrated the definite existence of an instability which bears a striking resemblance to HWI, but violates many of the supposed prerequisite conditions. We therefore suggest that any instability in a stratified shear layer be considered Holmboe instability if it manifests as propagating vortices on either side of the shear layer, regardless of the relative width of the density interface, the presence of critical layers or the minimum value of the gradient Richardson number.

Chapter 4

The effects of Prandtl number on the nonlinear dynamics of Kelvin-Helmholtz instability in two dimensions[1]

---

[1] This chapter is a slightly modified version of Parker, J. P., Caulfield, C. P., & Kerswell, R. R., The effects of Prandtl number on the nonlinear dynamics of Kelvin-Helmholtz instability in two dimensions. In review in *Journal of Fluid Mechanics*.

Abstract

It is known that the pitchfork bifurcation of Kelvin-Helmholtz instability occurring at minimum gradient Richardson number $Ri_m \simeq 1/4$ in viscous stratified shear flows can be subcritical or supercritical depending on the value of the Prandtl number, Pr. Here we study stratified shear flow restricted to two dimensions at finite Reynolds number, continuously forced to have a constant background density gradient and a hyperbolic tangent shear profile, corresponding to the 'Drazin model' base flow. Bifurcation diagrams are produced for fluids with $Pr = 0.7$ (typical for air), 3 and 7 (typical for water). For $Pr = 3$ and 7, steady billow-like solutions are found to exist for strongly stable stratification of Ri_m up to $1/2$ and beyond. Interestingly, these solutions are not a direct product of a Kelvin-Helmholtz instability, having too short a wavelength, but can give rise to Kelvin-Helmholtz states of twice the wavelength through subharmonic bifurcations. These short-wavelength states can be tracked down to at least $Pr \approx 2.3$ and act as instigators of complex dynamics even in strongly stratified flows when the flow is unforced.

4.1 Introduction

Kelvin-Helmholtz instability (KHI) is believed to be important in geophysical flows found in both the oceans (Smyth and Moum, 2012) and atmosphere (Fukao et al., 2011; Sun et al., 2015). Of particular importance is the generation of abyssal oceanic turbulence by the break down of shear instabilities, which is an area of significant uncertainty in climate modelling (Gregg et al., 2018b). Direct observations in the atmosphere, such as of sheared clouds, are relatively straightforward to perform, whereas only a few studies have observed Kelvin-Helmholtz billows in the abyssal ocean (Van Haren and Gostiaux, 2010). Amongst other parameters, the Prandtl number $Pr := \nu/\kappa$ (the ratio of kinematic viscosity ν to thermal diffusivity κ), involved in these two settings is different making it important to understand any resulting differences in the dynamics. In the atmosphere, $Pr \simeq 0.7$ whereas in the ocean $Pr \simeq 7$ and when the diffusion of salt is important (described by a diffusivity κ_s), the equivalent Schmidt number $Sc := \nu/\kappa_s \simeq 700$ (Thorpe, 2005).

Several simple models of stratified mixing layers have been proposed which exhibit KHI. The two most common, the Drazin (1958) and Holmboe (1960) models, are both found to be linearly stable in the inviscid case when the minimum gradient Richardson number Ri_m (as defined below) is greater than one quarter. This observation led to the celebrated Miles-Howard theorem (Miles, 1961; Howard, 1961), which shows that inviscid flows are always linearly stable when the gradient Richardson number is everywhere greater than one quarter. A longstanding challenge has been to determine whether significant *nonlinear* dynamics are also precluded for $Ri_m > 1/4$.

With viscosity, the Prandtl number enters the problem and there is a body of evidence suggesting this parameter has a significant impact on the behaviour of KHI (Salehipour et al., 2015; Rahmani et al., 2016). In particular, it has been shown that the bifurcation of KHI near (minimum gradient) Richardson number $1/4$ is subcritical when $Pr > 1$ and supercritical when $Pr < 1$ (Brown et al., 1981; Churilov and Shukhman, 1987; Lott and Teitelbaum, 1992; Mkhinini et al., 2013). (In this chapter we use the dynamical systems convention that 'subcritical' refers to the stable region $Ri_m > Ri_c$ and 'supercritical' to the unstable region $Ri_m < Ri_c$.) Despite this, most simulations studying the nonlinear behaviour of KHI have concentrated on the degenerate value $Pr = 1$ (Klaassen and Peltier, 1985; Caulfield and Peltier, 2000; Mashayek and Peltier, 2011; Kaminski et al., 2017), which allows a coarser computational grid to be used compared with higher Pr.

Although the effect of Pr on the sub/supercriticality of the bifurcation is well documented, this gives only a weakly nonlinear understanding beyond classical linear stability analyses, and cannot predict the full nonlinear effects. It could be the case that full turbulence is possible through subcritical transition for flows with high minimum Richardson numbers, substantially above $1/4$, where turbulence is usually assumed to be suppressed (Thorpe, 2005), or it could be that non-trivial, nonlinear states do not exist in flows with Ri_m significantly larger than $1/4$, and that the behaviour is simple and transient, as was found for $Pr = 1$ in chapter 2.Below, we argue for the former scenario by presenting direct evidence that 2-dimensional finite-amplitude billow-like states exist for $Ri_m \gtrsim 0.4$ - i.e. substantially above $1/4$ - for $Pr \gtrsim 2.3$ and indirect evidence that this situation continues below this threshold. Importantly, this implies that complicated temporal dynamics are possible for flows generally considered inert due to a lack of a Kelvin-Helmholtz linear instability.

To establish this key result, the chapter proceeds as follows. In §4.2, the equations of our forced model and numerical methods are briefly presented while in §4.3, bifurcation diagrams of the forced two-dimensional flow are given for $Pr \in \{0.7, 3, 7\}$, and the differences and continuous change between these two values is discussed. Finally, §4.4 considers the time evolution of the equivalent unforced systems by performing a 2D direct numerical simulation of the flow at various Richardson numbers, before concluding remarks are made in §4.5.

4.2 Methods

We study the Boussinesq equations for velocity $\mathbf{u}$ and buoyancy b:

$$\frac{\partial \mathbf{u}}{\partial t} + \mathbf{u} \cdot \nabla \mathbf{u} = -\nabla p + Ri_b b \mathbf{e}_z + \frac{1}{Re} \nabla^2 \mathbf{u}, \tag{4.1a}$$

$$\frac{\partial b}{\partial t} + \mathbf{u} \cdot \nabla b = \frac{1}{RePr} \nabla^2 b, \tag{4.1b}$$

$$\nabla \cdot \mathbf{u} = 0. \tag{4.1c}$$

The non-dimensional parameters are the Reynolds number Re, quantifying the relative importance of inertia to viscosity, the Prandtl number Pr, quantifying the relative importance of diffusion of buoyancy to viscosity, and the bulk Richardson number Ri_b, quantifying the relative importance of buoyancy to shear. With a gravitational acceleration g, shear layer depth $2d^*$, velocity difference $2U^*$, reference density ρ^*, reference density gradient $\Delta\rho^*/d^*$, and diffusivities ν and κ for momentum and density respectively, these are calculated as

$$Re := U^* d^*/\nu, \quad Pr := \nu/\kappa \quad \text{and} \quad Ri_b := \frac{g \Delta\rho^* d^*}{\rho^* U^{*2}}. \tag{4.2}$$

In this chapter we consider the evolution of perturbations away from the flow $\mathbf{u} = \tanh z \, \mathbf{e}_x$, $b = z$. This is the so-called ‘Drazin model’ of a mixing layer, for which weakly-nonlinear analyses have been performed (Churilov and Shukhman, 1987). Unlike the perhaps more commonly considered ‘Holmboe model’ with $b = \tanh z$, the Drazin model does not exhibit the viscous Holmboe instability discussed in chapter 3, which would complicate our picture. Using the Drazin model, the gradient Richardson number of the flow Ri_g is bounded below by Ri_b, since

$$Ri_g(z) := Ri_b \frac{db/\mathrm{d}z}{(du/\mathrm{d}z)^2} \geq Ri_m = Ri_g(0) = Ri_b. \tag{4.3}$$

Therefore, for this flow, the dynamically significant *minimum* gradient Richardson number Ri_m corresponds to the *bulk* Richardson number Ri_b which appears as a coupling parameter in the governing equations. Furthermore, the Miles-Howard theorem thus implies linear stability for $Ri_b > 1/4$ at infinite Re.

For finite Re, these choices of velocity and buoyancy profiles are not steady solutions of (4.1), but will diffuse away on an $O(Re)$ timescale. Nevertheless, the background profiles can be considered steady for perturbation dynamics over a shorter timescale. Therefore, when finding bifurcation diagrams (which require a non-decaying base state from which finite-amplitude states can bifurcate), we study solutions of the related forced equations

$$\frac{\partial \mathbf{u}}{\partial t} + \mathbf{u}\cdot\nabla\mathbf{u} + \tanh z \frac{\partial \mathbf{u}}{\partial x} + w\,\mathrm{sech}^2 z = -\nabla p + Ri_b b\mathbf{e}_z + \frac{1}{Re}\nabla^2\mathbf{u}, \tag{4.4a}$$

$$\frac{\partial b}{\partial t} + \mathbf{u}\cdot\nabla b + \tanh z \frac{\partial b}{\partial x} + w = \frac{1}{RePr}\nabla^2 b, \tag{4.4b}$$

$$\nabla\cdot\mathbf{u} = 0, \tag{4.4c}$$

where now $\mathbf{u}$, b and p represent the (possibly large) disturbances away from the background flow. Throughout, we take $Re = 1000$ which is relatively low compared with most modern direct numerical simulations, (see for example Salehipour et al. (2015)) but the high Pr combined with the computational intensity of the state tracking means that higher Re are not at present feasible. This limitation is discussed in §4.5.

The equations are solved on a two-dimensional domain periodic in the x direction with length L_x. Stress-free boundary conditions are imposed at $z = \pm L_z$. Both the solution of these equations and the finding and tracking of states and bifurcations largely uses the procedures presented in chapter 2.The key difference is that the non-uniform vertical grid has been modified to give a broader region of high resolution in the centre of the domain, in that we now use grid points located at

$$z_n = \frac{L_z}{3}\left[2\left(\frac{2n-N_z-1}{N_z-1}\right)^7 + \left(\frac{2n-N_z-1}{N_z-1}\right)\right].$$

States are converged using Newton-GMRES, then followed as parameters vary using pseudo-arclength continuation. The bifurcation analysis of §4.3 uses a grid with $N_x = 64$ horizontal grid points and $N_z = 512$ vertical grid points, which was shown to be sufficiently accurate by reconverging some of the points at $N_x = 256$, $N_z = 768$. For the direct numerical simulations of §4.4, for which much more complex spatial structures are possible, $N_x = 256$ and $N_z = 768$ is used.

For a state $X = (\mathbf{u}, b)$, we define the (energy-like) norm

$$\|X\| := \sqrt{\frac{1}{L_x}\int_{-L_z}^{L_z}\mathrm{d}z\int_0^{L_x}\mathrm{d}x\,(|\mathbf{u}|^2 + Ri_b b^2)}. \tag{4.5}$$

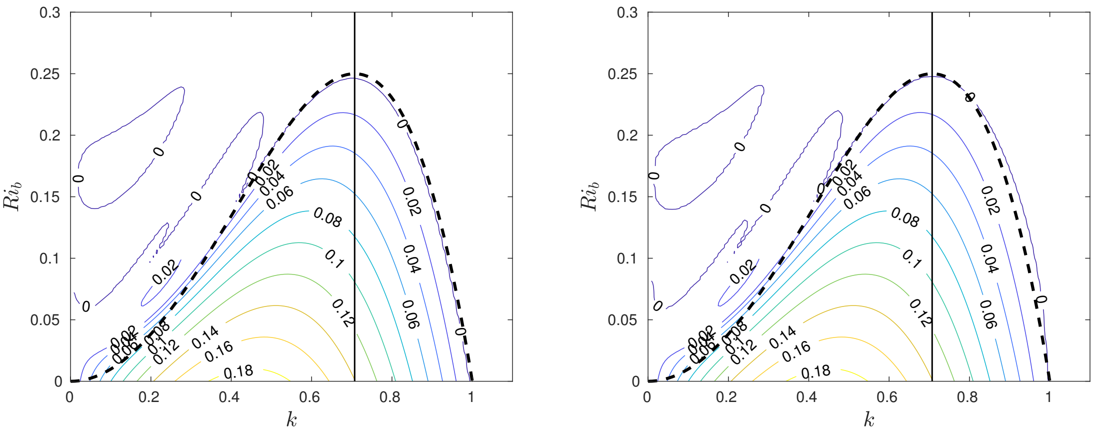

(a) (b)

Fig. 4.1 Linear stability diagrams of the flow at $Re = 1000$ for (a) $Pr = 0.7$ (b) $Pr = 7$, given as contours of the growth rate σ plotted against the wavenumber k and Ri_b, where the fastest growing mode of the form $e^{ik(x-ct)+\sigma t}\hat{\mathbf{u}}(z)$ has been found. The vertical line marks the wavenumber corresponding to a mode-1 disturbance in our domain of length $2\sqrt{2}\pi$. Note that mode-n, $n \geq 2$, are all stable for all Ri_b. The dashed line shows the stability boundary calculated by Drazin (1958) for $Re \to \infty$. Here, as with all the nonlinear calculations, the domain half-height is $L_z = 10$.

We also define a second function $m(X)$ of a given state, a measure of the component of the vertical velocity in the first Fourier mode

$$m(X) := \frac{1}{L_x}\int_{-L_z}^{L_z} \mathrm{d}z \int_0^{L_x} \mathrm{d}x\, u_z \sin\frac{2\pi x}{L_x}. \tag{4.6}$$

4.3 Bifurcation diagrams

Figure 4.1 shows the linear stability, calculated using a code from Smyth and Carpenter (2019), of the flows considered. The shape of the stability boundary is very close to the inviscid analytical result $Ri_b = k^2(1-k^2)$ (Drazin, 1958), which is overlaid. One curious difference is the presence of bands of instability at low wavenumbers. These have nonzero phase speed, and are similar to the ‘Holmboe instability’ mentioned in passing by Smyth and Peltier (1989) for a linear stratification and piecewise linear shear. The exact structure of these unstable bands is highly sensitive to the domain height, and they are believed to be caused by a resonance between discretised internal waves and the shear. This diagram varies little as Pr is changed. However, as we demonstrate below, the nonlinear behaviour is strongly affected by Pr.

Henceforth we concentrate on the case of a domain of fixed streamwise length $L_x = 2\sqrt{2}\pi$. This is the wavelength of the marginally unstable mode at $Ri_b = 1/4$ in the inviscid, unbounded case, which is little modified in our viscous domain of finite height. The associated wavenumber $k_1 := 1/\sqrt{2}$ is marked on figure 4.1 as a vertical line. For $0.7 \leq Pr \leq 7$ the critical Richardson number Ri_c is close to, but slightly less than $1/4$ due to viscous effects: $Ri_c \approx 0.246$ for $Pr = 0.7$ and $Ri_c \approx 0.248$ for $Pr = 7$. Note that for this choice of domain size, only mode-1 disturbances (i.e. those which have one wavelength in the domain) are linearly unstable, as any mode with $k \geq 2k_1$ (so two or more wavelengths in the domain) is linearly stable. A domain height of $L_z = 10$ was chosen, as this was assumed to be sufficiently large compared with L_x that the behaviour at large Ri_b is not significantly altered, while still being computationally efficient. At low Ri_b, this choice of L_z becomes significant, as discussed a little later.

Figure 4.2 shows the primary branch of steady KH states at $Pr = 0.7$ which bifurcates from the background flow at $Ri_b \approx 0.246$, in agreement with the linear stability analysis of figure 4.1a. The branch was found to be stable at $Ri_b = 0.24$, and a state was converged here using a simple timestepper. The rest of the branch was traced out using pseudo-arclength continuation. The pitchfork bifurcation is clearly supercritical, in agreement with weakly-nonlinear theory. Figure 4.2 also shows the bifurcation curve at $Pr = 1$ described in chapter 2. This is close to the degenerate case between super- and sub-criticality; it can just be made out that this case is very slightly subcritical.

Figure 4.3 shows the much more complicated situation at $Pr = 7$. The pitchfork bifurcation P_0 at $Ri_b \approx 0.247$ of the background flow is subcritical, in agreement with weakly nonlinear theory. The state which arises is therefore unstable, and was converged by a conventional edge-tracking procedure (e.g. Schneider et al., 2007). Edge-tracking was performed at $Ri_b = 0.26$, applying interval bisection with initial conditions of the upper branch state with wavenumber $k = k_1$ (see below), scaled to have lower amplitudes. At P_1, two symmetric branches of wavenumber k_1, which differ in phase by $\pi/2$, collide to give a state with wavenumber $k_2 := 2k_1$. The saddle-node bifurcations S_1, S_2 and S_3 indicate the location of this mode-2 branch.

Separately to this, a stable upper branch state from $Pr = 3$ (where the system gives a simpler subcritical bifurcation, see below) was continued up in Pr to give rise to the mode-1 states of wavenumber k_1 which join at the pitchfork P_2. At this value of Pr, none of this branch is stable. In fact, numerous other pitchfork and Hopf bifurcations, the precise locations of which were not determined, were found to exist on all branches, so that only a small section of the k_2 branch is stable. These secondary bifurcations give rise to the complex and apparently chaotic behaviour of the system discussed in §4.4.

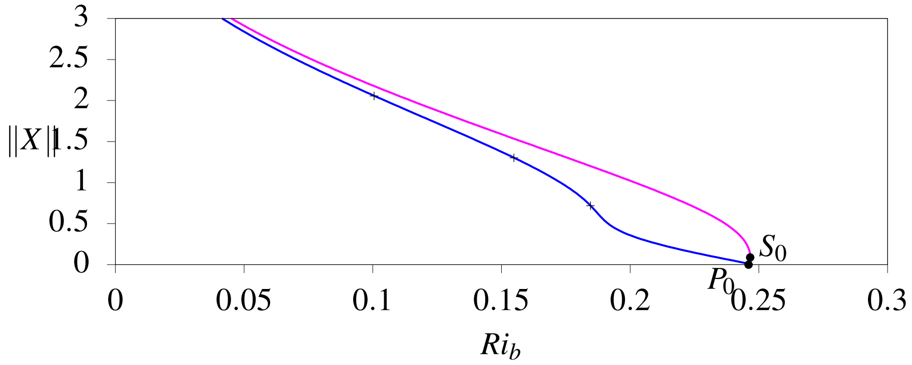

Fig. 4.2 Bifurcation diagram for the Drazin model with a domain width of $2\sqrt{2}\pi$, with $Re = 1000$ and $Pr = 0.7$ (blue) and $Pr = 1$ (pink). The line represents a steady state solution with magnitude shown on the vertical axis. The crosses mark points reconverged at a higher resolution.

As the states in figures 4.2 and 4.3 are traced to lower Ri_b and their amplitude and therefore physical extent becomes sufficiently large, the states begin to 'feel' the effects of the boundaries at $z = \pm L_z = \pm 10$. At this point, the structure changes dramatically, with the branches folding back to higher Ri_b, and the results are no longer physically relevant to unbounded flows. We have therefore chosen to exclude these sections from the diagrams. In an unbounded or sufficiently tall domain, the unstable states presumably continue past $Ri_b = 0$, as the unstratified Kelvin-Helmholtz instability saturates as a finite-amplitude 'billow', although whether this also occurs for the k_2 branch is unclear.

Figure 4.4 depicts three low amplitude states on the branch between the pitchfork bifurcations P_0 and P_1. Figure 4.4a is relatively close to the primary pitchfork P_0, and shows a clear mode-1 structure of wavenumber k_1, in agreement with the unstable eigenmode of the background flow, which the structure closely resembles. Figure 4.4b is further along the branch and there is now a noticeable mode-2 signal, manifesting as a structure emerging between the two 'billows'. The amplitude has also increased. There is a natural transition therefore between the eigenmode and the pure mode-2 structure at P_1, as shown in figure 4.4c. A similar transition, at significantly higher amplitude, with structures much more closely resembling classic KH billows, is observed on the upper branch, as Ri_b increases towards P_2 (figure 4.5).

Figure 4.6 shows the mode-2 structures, i.e. those with wavenumber k_2, at the three saddle-node bifurcation points. They are all qualitatively different. S_1 and S_3, in figures 4.6a and 4.6c respectively, are both highly reminiscent of classical KH billows, with a clear elliptical vortex. At S_1 the billows are significantly separated spatially, but at S_3 they are much more closely backed, but still with a distinctive 'braid' region connecting them. At S_2,

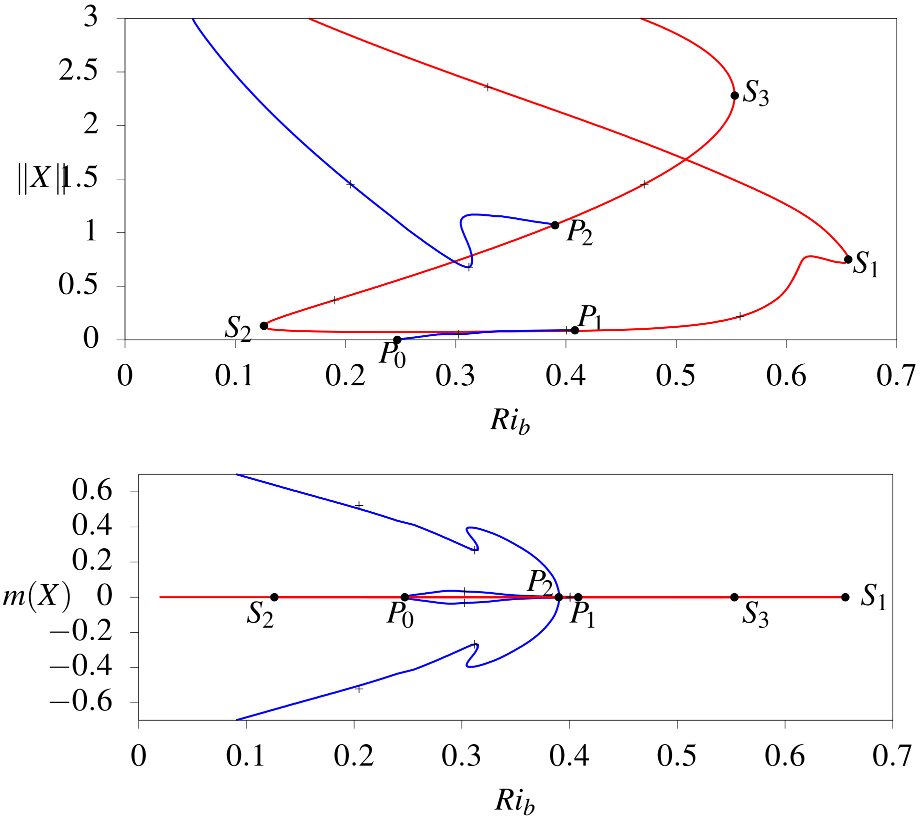

Fig. 4.3 Top: As for figure 4.2, but with $Pr = 7$. Bottom: the same data, showing the contribution of the first Fourier mode in the streamwise direction to the states. The blue lines shows states with wavenumber $k_1 := 1/\sqrt{2}$, in agreement with the linear instability of the background flow. The red lines shows states with wavenumber $k_2 := 2k_1$, which arise at the pitchfork bifurcation P_1. The crosses mark points reconverged at a higher resolution.

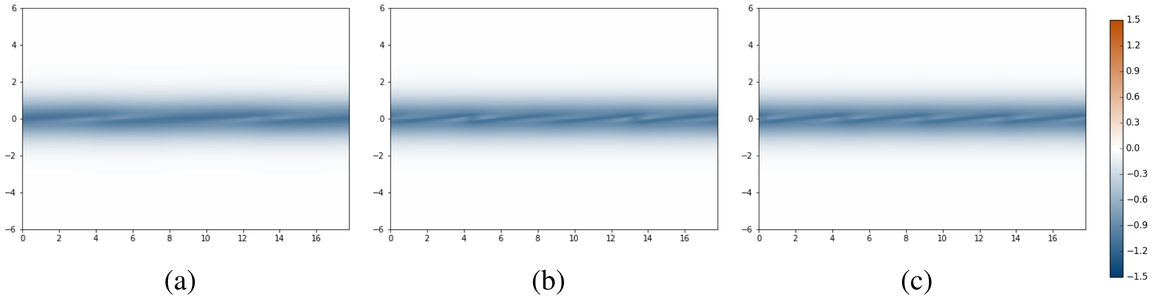
(a) (b) (c)

Fig. 4.4 Vorticity fields of the steady perturbation states at $Pr = 7$ on the mode-1 branch connecting P_0 and P_1. (a) $Ri_b \approx 0.3$, (b) $Ri_b \approx 0.4$, (c) at P_1, $Ri_b \approx 0.41$. Here, and in all other such figures, two domain widths have been plotted to show the periodic structure.

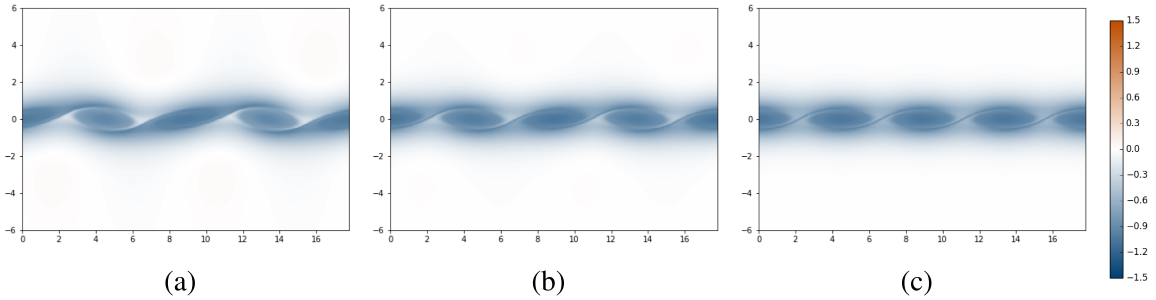
(a) (b) (c)

Fig. 4.5 Vorticity fields on the upper mode-1 ($k = k_1$) branch at $Pr = 7$. (a) $Ri_b \approx 0.34$, (b) $Ri_b \approx 0.38$, (c) at P_2, $Ri_b \approx 0.39$.

a low amplitude state intermediate between S_1 and S_3, the structure is different again, and much less familiar.

The bifurcation points labelled in figure 4.3 can themselves be converged using a Newton-GMRES method, and tracked as Pr is varied, in a way identical to the tracking of bifurcation points as Re varies in chapter 2.The basic (mode-1) saddle-node bifurcation found in that chapter, which we call S_0, was continued to larger values of Pr just as those of figure 4.3 were continued to smaller values of Pr. The primary pitchfork P_0, which exists for $Pr < 1$ too, can be found using this method or from linear stability analysis of the background flow. The results are shown in figure 4.7. S_1 and S_3 were found to be difficult to converge and continue, due to the presence of several marginally stable eigenvalues nearby, but were located directly at $Pr = 7$ and $Pr = 3$. S_0 could not be continued beyond $Pr = 3.8$, and there is no obvious bifurcation point which corresponds to S_0 in figure 4.3. P_1, P_2 and S_2 all stopped converging below $Pr = 2.3$ and they appear to collide and disappear.

To clarify the situation, the intermediate value $Pr = 3$ was studied in detail (figure 4.8). The main (mode-1) branch, with $k = k_1$ and which connects to the fundamental pitchfork P_0, is a simple subcritical curve, extending up to $Ri_b \approx 0.3$. Completely disconnected from

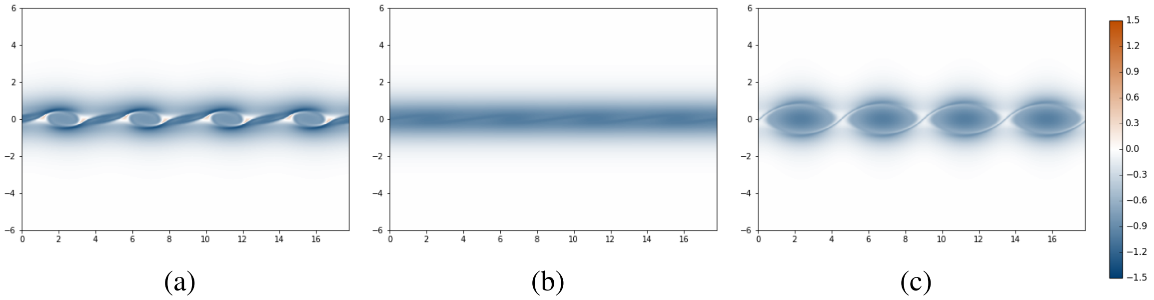

(a) (b) (c)

Fig. 4.6 Vorticity fields of the mode-2 ($k = k_2$) steady states at $Pr = 7$ at the saddle-node bifurcations (a) S_1, (b) S_2, (c) S_3.

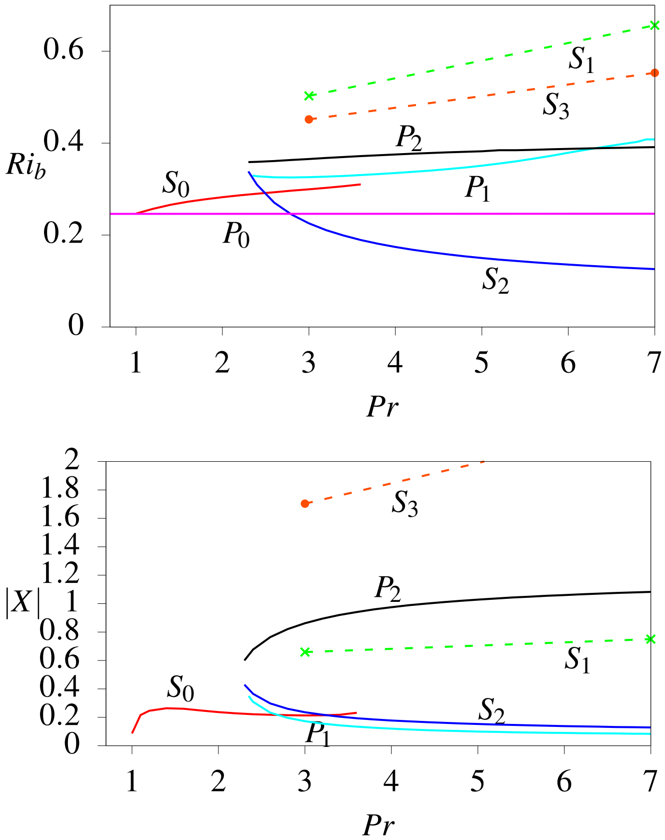

Fig. 4.7 Tracking of the various bifurcation points shown in figures 4.2 and 4.3 as Pr varies. S_1 and S_3 were not tracked, but their locations at $Pr = 3$ and $Pr = 7$ have been marked and interpolated with dashed lines.

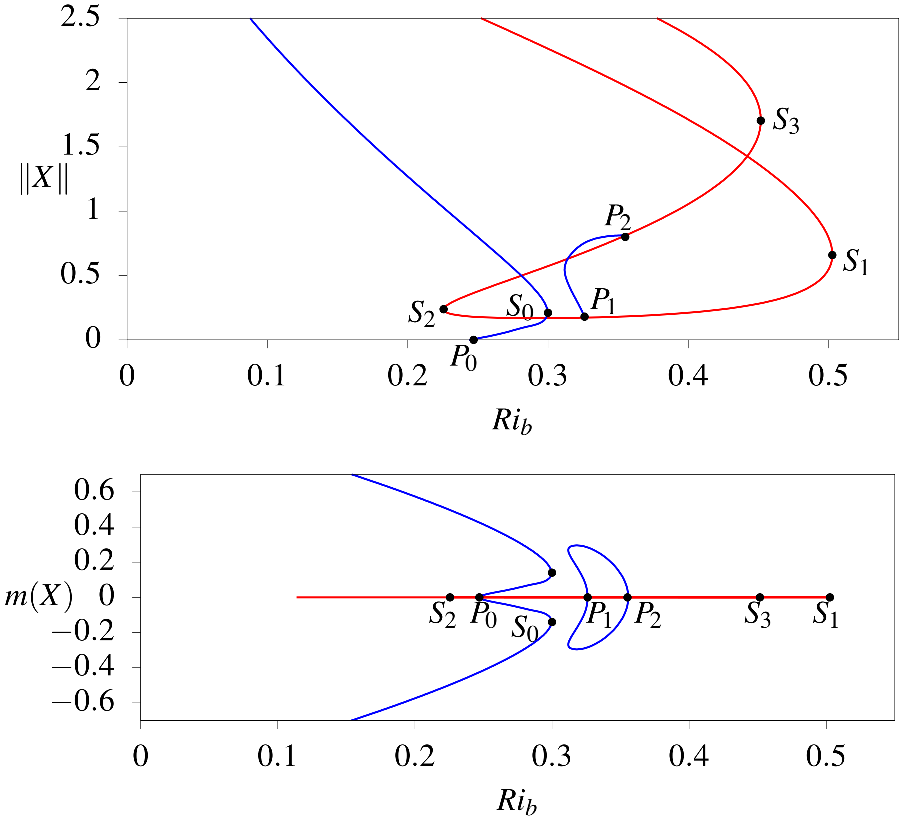

Fig. 4.8 As for figure 4.3, but with $Pr = 3$.

this, extending to higher Ri_b, is a mode-2 loop (with $k = k_2$), which is a continuation of the similar curve shown in figure 4.3. There is also a mode-1 branch ($k = k_1$) connected to this, which links P_1 and P_2. Between $Pr = 3$ and $Pr = 7$, this mode-1 branch collides with the fundamental mode-1 branch to give the situation in figure 4.3. Below $Pr = 3$, it appears that this disconnected curve closes at $Pr \approx 2.3$, though the picture is incomplete, since the behaviour of the states at high amplitude is unknown. The most natural explanation would be that the k_2 branch is a closed loop, but no evidence of this has been found up to amplitudes for which the finite vertical domain size becomes important and obscures the results.

4.4 The unforced dynamical system

As mentioned in §4.2, the equations (4.4) are an approximation for large but finite Re, which ignores the fact that the background profiles diffuse. This is not a problem for rapidly changing perturbations to the background flow, but many of the connections between the steady states found in §4.3 appear to be very slow dynamically. In particular, although the

KHI grows rapidly from small disturbances to the background, it took exceptionally long time integrations, of non-dimensional times an order of magnitude larger than *Re*, before the billow states were steady enough for the Newton iteration to converge on the stable states. For this reason, it is difficult to draw conclusions about the unforced system directly from the results of §4.3. The steady states of the forced system do not correspond to steady states in the unforced system, and a bifurcation analysis in the same way is not possible. Therefore, we explore the behaviour of the unforced system (4.1) using (two-dimensional) direct numerical simulation.

Direct numerical simulations started from noise follow chaotic trajectories and visit states much more spatially complex than the simple steady states discussed in §4.3. Therefore, a much higher resolution is required to avoid 'ringing' artifacts and be confident that the equations are being solved accurately. It was found to be sufficient to use 256 horizontal modes and 768 grid points vertically. Eight different simulations were performed, at $Re = 1000$, with a domain half-height $L_z = 10$, in agreement with the calculations of section 4.3. We study the cases of $Pr = 0.7$ and $Pr = 7$, modelling air and water; $Ri_b = 0.1$ and $Ri_b = 0.3$ for the supercritical and subcritical regions; and initial disturbance wavenumbers k_1, for which the linear instability is approximately maximised, and k_2, for which no linear instability is predicted but for which we found nonlinear steady states. The simulations of equations (4.1) are started from the Drazin model plus a random perturbation,

$$\mathbf{u} = \tanh z\,\mathbf{e}_x + \mathbf{u}', \quad b = z + b', \tag{4.7}$$

where the perturbation $X = (\mathbf{u}', b')$ has components only in the first 42 Fourier modes horizontally (with even numbered modes only for k_2) and first four Hermite polynomials vertically, as in chapter 3. The initial perturbations are scaled to have amplitude $\|X\| = 0.3$, which is greater than that of the lowest branch of states in figure 4.3.

For perturbations with $k = k_2$ at $Pr = 0.7$, no significant nonlinear behaviour was observed at either value of Ri_b. Figures 4.9a and 4.9c both show S-shaped vorticity streaks characteristic of the transient, linear Orr mechanism at $t = 20$. By $t = 100$, as shown in figures 4.10a and 4.10c, these have diffused away to give simple shear layers, which are slightly asymmetric due to the random nature of the initial perturbations. These results are unsurprising, since no linear instability exists at this wavelength and we did not detect any nonlinear modes at this *Pr* either.

For perturbations with $k = k_1$ at $Pr = 0.7$, nonlinear billow structures are observed at both $Ri_b = 0.1$ and $Ri_b = 0.3$. The former is to be expected since a linear instability exists, but the latter is more surprising, as the base flow is linearly stable and the results of §4.3 show the bifurcation to be a simple supercritical one. The existence of a finite-amplitude steady state in the forced model should be expected to imply non-trivial dynamics in the unforced simulations, but the converse is not necessarily true. We speculate further on this case in §4.5.

The $k = k_2$ simulations at $Pr = 7$ show what we believe to be the most novel result reported here, namely that Kelvin-Helmholtz-like billows can exist in domains too narrow to support a linear instability. Figure 4.11a with $Ri_b = 0.1$ appears to just show the results of the Orr mechanism on the initial perturbation, but by $t = 100$ shown in figure 4.12a one can just discern a long-lived, low-amplitude structure which is highly reminiscent of the lower branch of solutions found in §4.3, as shown in figure 4.6b. Figures 4.11c and 4.12c at $Ri_b = 0.3$ show the slow development of a higher amplitude state, which is very similar to the exact solution show in figure 4.6a.

Figures 4.11b and 4.12b show the large billow which develops at $Pr = 7$ and $Ri_b = 0.1$. This is despite the fact that we also found steady states with double this wavenumber in the forced model, but since all the states we found at these parameters were unstable, it is difficult to draw conclusions. Similarly at $Ri_b = 0.3$ in figures 4.11d and 4.12d, a small billow of wavenumber k_1 is observed. It could be the case that the initial perturbation determines whether a mode-1 or mode-2 structure develops in the wider domain, since the initial amplitude is rather large and the results are noisy, or this could be evidence that the mode-1 structure is, in some sense, more stable.

Movies of all eight of these simulations are available in the supplementary material. We note that in some situations the billows are observed to propagate through the domain; this is not evidence of a Holmboe wave type instability, but rather a consequence of the large initial amplitude perturbation having a net effect on the mean flow.

4.5 Conclusion

This chapter presents a systematic study of the nonlinear behaviour of the Drazin model of a two-dimensional finite Reynolds-number stratified shear layer - a hyperbolic tangent shear and constant density gradient - at three different values of Pr, using both the tracking of exact coherent structures in the forced system and direct numerical simulations of the unforced system.

In the $Pr = 0.7$ case, we found a simple, supercritical pitchfork bifurcation, with the resulting steady-state Kelvin-Helmholtz billows increasing in amplitude as (minimum) Richardson number is decreased, so far as we could track them. This agrees with weakly-nonlinear results which predict a supercritical bifurcation for $Pr < 1$. Despite the fact that we have found no finite-amplitude steady states at $Ri_b > 1/4$ when $Pr = 0.7$, the

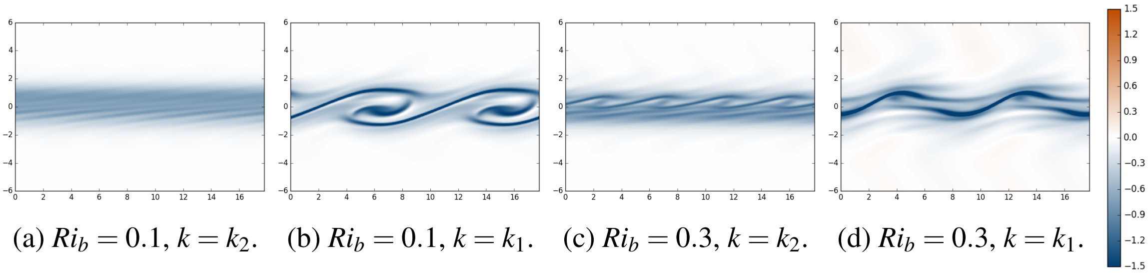

(a) $Ri_b = 0.1$, $k = k_2$. (b) $Ri_b = 0.1$, $k = k_1$. (c) $Ri_b = 0.3$, $k = k_2$. (d) $Ri_b = 0.3$, $k = k_1$.

Fig. 4.9 Total vorticity field of the unforced flow at time $t = 20$ for the Drazin model plus a random perturbation. Parameter values: $Re = 1000$, $Pr = 0.7$.

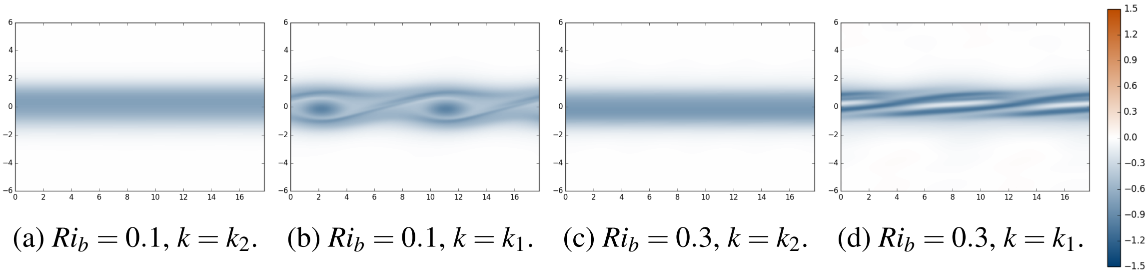

(a) $Ri_b = 0.1$, $k = k_2$. (b) $Ri_b = 0.1$, $k = k_1$. (c) $Ri_b = 0.3$, $k = k_2$. (d) $Ri_b = 0.3$, $k = k_1$.

Fig. 4.10 Vorticity at $Re = 1000$ and $Pr = 0.7$ at $t = 100$.

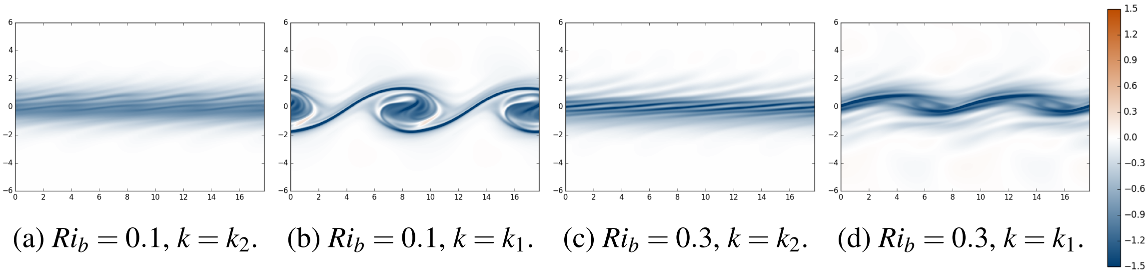

(a) $Ri_b = 0.1$, $k = k_2$. (b) $Ri_b = 0.1$, $k = k_1$. (c) $Ri_b = 0.3$, $k = k_2$. (d) $Ri_b = 0.3$, $k = k_1$.

Fig. 4.11 Vorticity at $Re = 1000$ and $Pr = 7$ at $t = 20$.

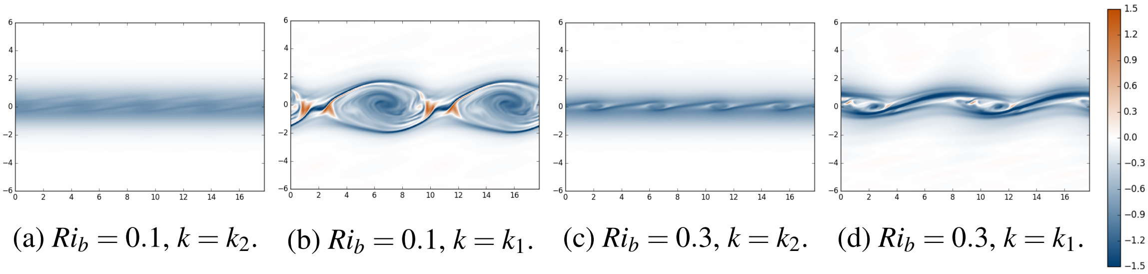

(a) $Ri_b = 0.1$, $k = k_2$. (b) $Ri_b = 0.1$, $k = k_1$. (c) $Ri_b = 0.3$, $k = k_2$. (d) $Ri_b = 0.3$, $k = k_1$.

Fig. 4.12 Vorticity at $Re = 1000$ and $Pr = 7$ at $t = 100$.

unforced simulations of §4.4 showed clear nonlinear billow-like structures at $Ri_b = 0.3$. This could mean that there are additional steady states which are either connected to the primary instability by a bifurcation of the upper branch, or disconnected, perhaps through a homotopic continuation of the disconnected states found at $Pr = 3$ (see figure 4.8). It could also be the case that these structures appear on trajectories which do not have an associated steady state, but rather represent an excitable system, for which the base state is stable but fast/slow dynamics nevertheless allow rapid transient growth. The observation of this structure means we are unable to state categorically whether significant nonlinear behaviour, which could lead to turbulence and mixing in the three-dimensional case, is likely to occur for $Ri_b > 1/4$ in gases, although these results and the work of Kaminski et al. (2017) are highly suggestive that there is more to discover at $Pr \lesssim 1$.

We observed a strongly subcritical pitchfork bifurcation in the flow modelling water with $Pr = 7$, as expected from the weakly-nonlinear predictions. Significantly, states were found to exist well above $Ri_b = 0.5$. Moreover, the fact that the mode-1 structure bifurcated in a subharmonic instability from a hitherto-unknown mode-2 structure implies that billow structures exist at wavelengths which are linearly stable. This striking result was corroborated by direct numerical simulations of the unforced model, with observations of such billows at both $Ri_b = 0.1$ and $Ri_b = 0.3$. These results clearly indicate that in oceanic flows, the Miles-Howard criterion for linear stability does not preclude complicated mixing dynamics on times short compared to viscous diffusion.

The transition between $Pr = 0.7$ and $Pr = 7$ was studied in the forced model, to understand how the structures relate to one another. $Pr = 1$ and $Pr = 3$ both show the primary branch of billow states to be a simple subcritical one, but at $Pr = 3$, disconnected mode-1 states were also found, connecting to the mode-2 states at $Pr = 7$, and apparently disappearing below $Pr = 2.3$. Increasing the Prandtl number above 3, the disconnected mode-1 branch collides at some point (< 7) with the primary mode-1 branch to fundamentally change the mode-1 solution topology. Given this microcosm of behaviour, it is entirely plausible that (a) further loops of mode-1 solutions exist off the mode-2 branch and survive down below $Pr \approx 2.3$ as well as (b) the mode-2 branch itself reaches to much lower Pr. In fact, it is not inconceivable that the mode-2 branch exists at $Pr = 1$ but is not at all connected to the primary mode-1 branch of Kelvin-Helmholtz instability tracked in chapter 2.

It should be clear that there are numerous natural extensions to the present study. It would be of interest to see how the results vary with Re, as $Re = 1000$ is much lower than in geophysically relevant flows. It is assumed that if complex behaviour exists at $Re = 1000$ for given Pr and Ri_b, it will also do so for higher Re - in chapter 2 it was shown that increasing Re corresponds to an increase in the maximum Ri_b of steady states, at least for $Pr = 1$. Much higher values of *Pr*, as would be relevant to salt-stratified water, could also be an area for future study. Our results suggest that the dynamics only get more complex with increasing *Pr*, and higher Ri_b can give rise to steady states. Increasing either *Re* or *Pr* significantly would require a finer discretisation of the domain, necessitating either much more computational resources or a different strategy from that pursued here.

Even at the parameters we studied, much remains unclear. To what other states do the secondary bifurcations give rise? Hopf bifurcations were detected, so periodic orbits as well as steady states are expected. What new dynamics does a third, spanwise dimension add to the flow? Certainly all 2-dimensional states we have found will exist in three dimensions, but many more secondary instabilities will exist and we expect those states found to be stable in two dimensions to become unstable in three. From direct numerical simulations, three dimensional flows prone to primary Kelvin-Helmholtz instability are known to behave very differently, quickly breaking down into turbulence, without long-lived coherent billows; most of the mixing associated with KHI is due to this billow breakdown in three dimensions. Finally, how do the steady states we have found relate to the chaotic behaviour of the unforced problem? We have demonstrated a similarity between the dynamics, but it is not clear that exact steady states in the forced model correspond to any particular trajectories in the unforced case.

Chapter 5

Optimal perturbation growth on a breaking internal gravity wave

Abstract

The breaking of internal gravity waves in the abyssal ocean is thought to be responsible for much of the mixing necessary to close oceanic energy budgets. It has been speculated that Kelvin-Helmholtz type shear instabilities are the primary mechanism of transition to turbulence in this breaking. However, recent evidence has suggested that convective instability of the statically unstable density distributions which can arise could instead be responsible when the mean Richardson number is high. We perform a systematic analysis of the stability of internal gravity waves in a background shear flow, using direct-adjoint looping to find the perturbation giving maximal energy growth on this evolving flow. We find that in all cases, three-dimensional, convective mechanisms produce greater energy growth than their two-dimensional counterparts. This is particularly pronounced when the energy is maximised at larger target times.

5.1 Introduction

Energy budgets of the global oceans suggest that turbulence, on scales too small to simulate directly in computational models, is an important element to dissipate energy and close the budget (Wunsch and Ferrari, 2004). The existence and behaviour of such turbulence is crucial to understanding the mixing of different waters, which has implications for the storage of heat and carbon dioxide in the oceans. Observations (Baker and Gibson, 1987; Alford and Pinkel, 2000) have shown that such turbulence is intermittent and localised, and the nonlinear breaking of internal gravity waves has been proposed as a likely candidate for the main source of the turbulence.

Such wave breaking could be caused by a number of mechanisms. Lombard and Riley (1996) used linear stability analysis to show that instabilities on an internal wave are strongly dependent upon both the amplitude and the propagation angle of the wave, with strongly three-dimensional and two-dimensional modes being dominant in different cases. One imporant effect, not taken into account in these analyses, is the amplification of waves as they approach critical layers within the flow (Booker and Bretherton, 1967), where the flow velocity matches the phase speed. Motivated by these observations, Howland et al. (2020) set up an idealised flow to numerically model an internal gravity wave incident on a shear flow: a superposition of a plane internal wave in a constant density gradient, and a simple sinusoidal shear profile. We exactly recreate the basic flow used in that work, but study it from a more theoretical viewpoint.

The default first step in understanding instabilities of a steady flow is to perform a normal mode stability analysis, i.e. to discover which infinitesimal disturbance grows at the fastest exponential rate. The form of this disturbance is often closely related to the finite-amplitude structures which arise as the flow evolves. However, the flow model used by Howland et al. (2020) is not a steady one, and so different structures will grow fastest at different points in the evolution of the basic flow. One approach would be to perform linear stability analyses on ‘frozen’ background flows at different times, which has been done extensively, for example, on Kelvin-Helmholtz billows (Klaassen and Peltier, 1985; Caulfield and Peltier, 2000; Mashayek and Peltier, 2012a,b, to name but a few). This is a valid strategy for slowly varying background flows, or for quickly growing instabilities, but otherwise just gives a hint on the possible nonlinear behaviour.

The approach we take in this chapter is to ask, over a fixed finite time, which initial, infinitesimal perturbation is amplified by the greatest amount. This is still an entirely linear approach, but typically requires a lot more computation than traditional linear stability analyses. Indeed, even for a steady background flow, the finite time ‘optimal growth’ is still an interesting problem, since for non-normal linear operators such as in the Orr-Sommerfeld equations, the most unstable normal mode is not necessarily the one that grows the most over a finite time interval (Schmid, 2007). This problem can be studied via a singular value decomposition of the time-integrated evolution operator (Schmid and Henningson, 2001). However, with an evolving background flow, this integrated operator is incredibly complex, so some form of iterative method is required, based on a DNS of the equations.

The method we employ, direct-adjoint looping (DAL) (Luchini, 2000; Corbett and Bottaro, 2000), is derived in section 5.2.1, and is essentially equivalent to that used by Arratia et al. (2013) to study optimal growth on a 2D, time-evolving Kelvin-Helmholtz billow. It is an iterative method, with each solution of the Navier-Stokes equations followed by a solution of the corresponding adjoint equations, which gives a sensitivity with respect to a given quantity of interest, allowing one to optimise, for example, the time-integrated energy, the mixing, or the difference from a particular state. In this chapter we optimise the energy at time T of a infinitesimal perturbation at time $t = 0$, which gives a particularly simple formulation. It is also the objective functional which is easiest to compare with a traditional linear stability analysis.

When studying shear flows, recourse is often made to Squire's theorem (Squire, 1933), and its stratified equivalent proven by Yih (1955) (see Smyth et al. (1988) for a detailed discussion and proof), which implies that in most circumstances, the primary instability is a two-dimensional one. However, this only applies for a strictly parallel, steady flow, which is not the case here. For the flow studied herein, we have no reason a priori to assume that the fastest growing disturbance is a two-dimensional one, and indeed we shall see that it is not. However, it is sufficient to consider separate individual Fourier modes in this direction, since the background flow is two-dimensional and the disturbances are treated as infinitesimal. This means that there is no nonlinear interaction between the disturbance and itself. Furthermore, we are considering unbounded flows in the additional, spanwise direction.

The remaining three sections of the chapter are as follows: §5.2 gives the precise flow we are considering, and gives the derivation and implementation details of the direct-adjoint looping algorithm. §5.3 presents our results for different target times and discusses in detail two different cases, and §5.4 gives concluding remarks. Appendix 5.A presents the derivation of the adjoint equations which are stated in §5.2.

5.2 Methods

The Boussinesq equations consist of the Navier-Stokes equation, the advection-diffusion equation for buoyancy and the incompressibility condition

$$\frac{\partial \mathbf{u}}{\partial t} + \mathbf{u} \cdot \nabla \mathbf{u} = -\nabla p + Ri_b b \mathbf{e}_z + \frac{1}{Re} \nabla^2 \mathbf{u}, \tag{5.1a}$$

$$\frac{\partial b}{\partial t} + \mathbf{u} \cdot \nabla b = \frac{1}{RePr} \nabla^2 b, \tag{5.1b}$$

$$\nabla \cdot \mathbf{u} = 0. \tag{5.1c}$$

These equations have been non-dimensionalised using a typical length scale L, velocity U, gravitational acceleration g, density ρ, density gradient ρ_z, kinematic viscosity ν and density diffusion coefficient κ to give the nondimensional Reynolds number $Re = \rho UL/\mu$, Prandtl number $Pr = \nu/\kappa$, and bulk Richardson number $Ri_b = g\rho_z L^2/\rho U^2$.

Following Howland et al. (2020), we consider an internal gravity wave with wavevector $\mathbf{k} = (k_1, 0, k_3)$ (and define $k = ||\mathbf{k}||$) and 'wave steepness' s incident on a background flow that is uniformly stratified and has a sinusoidal velocity profile, so that at time $t = 0$

$$u = \sin z + \frac{s\omega}{k_1}\sin(\mathbf{k}\cdot\mathbf{x}), \tag{5.2a}$$

$$w = \quad -\frac{s\omega}{k_3}\sin(\mathbf{k}\cdot\mathbf{x}), \tag{5.2b}$$

$$b = z \quad + \frac{s}{k_3}\cos(\mathbf{k}\cdot\mathbf{x}). \tag{5.2c}$$

where $\omega^2 = Ri_b\frac{k_1^2}{k^2}$ is the (squared) frequency of the internal wave, so that the phase speed of this wave in isolation is given by $\mathbf{k}\omega/k^2$. The evolution of this two-dimensional background flow is complex, as will be seen in section 5.3.

An infinitesimal (now three-dimensional) perturbation to equations (5.1) satisfies the linear PDEs (the primes denote the perturbation)

$$\frac{\partial \mathbf{u}'}{\partial t} + \mathbf{u}\cdot\nabla\mathbf{u}' + \mathbf{u}'\cdot\nabla\mathbf{u} = -\nabla p' + Ri_b b'\mathbf{e}_z + \frac{1}{Re}\nabla^2\mathbf{u}', \tag{5.3a}$$

$$\frac{\partial b'}{\partial t} + \mathbf{u}\cdot\nabla b' + \mathbf{u}'\cdot\nabla b = \frac{1}{RePr}\nabla^2 b', \tag{5.3b}$$

$$\nabla\cdot\mathbf{u}' = 0. \tag{5.3c}$$

In these equations, $\mathbf{u}$ and b evolve with time according to (5.1).

5.2.1 Direct-adjoint looping

Consider the space of state vectors $X = (\mathbf{u}'_X, b'_X)$ satisfying $\nabla\cdot\mathbf{u}'_X = 0$ (p' can be determined from these by solving a Poisson equation). Let us define a linear operator Φ_T acting on this space, defined as the solution of (5.3a)-(5.3c) up to time $t = T$. Further, we define an inner product $\langle X,Y\rangle = \frac{1}{L_xL_yL_z}\int(\mathbf{u}'_X\cdot\mathbf{u}'_Y + Ri_b b'_X b'_Y)\,\mathrm{d}V$, so that an energy for the perturbation X is given by $\frac{1}{2}\langle X,X\rangle$. We wish to find the maximum possible energy growth of a perturbation of fixed energy over a time T, i.e. to maximise the Lagrangian

$$\mathscr{L} = \frac{1}{2}\langle X_T, X_T\rangle + \lambda\left(\frac{1}{2}\langle X_0, X_0\rangle - \frac{1}{2}\right) + \left\langle \tilde{X}, X_T - \Phi_T X_0\right\rangle. \tag{5.4}$$

Here, λ is a Lagrange multiplier that enforces the normalisation of the initial state X_0. The precise choice of this initial energy is irrelevant, since the system is linear and we are only interested in the energy gain, i.e. the ratio of final energy to initial energy, but for a well-posed problem we nevertheless must constrain the initial energy. $\tilde{X}$ is a Lagrange multiplier state we call the adjoint state – for reasons which will become clear below – that enforces that

$X_T = \Phi_T X_0$. At an optimal, all variations of the Lagrangian vanish, so that

$$0 = \frac{\delta \mathscr{L}}{\delta \lambda} = \frac{1}{2}\langle X_0, X_0 \rangle - \frac{1}{2}, \tag{5.5a}$$

$$0 = \frac{\delta \mathscr{L}}{\delta \tilde{X}} = X_T - \Phi_T X_0, \tag{5.5b}$$

$$0 = \frac{\delta \mathscr{L}}{\delta X_0} = \lambda X_0 - \Phi_T^\dagger \tilde{X}, \tag{5.5c}$$

$$0 = \frac{\delta \mathscr{L}}{\delta X_T} = X_T + \tilde{X}, \tag{5.5d}$$

where $\Phi_T^\dagger$ is the adjoint operator to Φ_T with respect to our inner product. The precise definition of $\Phi_T^\dagger$ is the solution of the so-called adjoint equations

$$-\frac{\partial \tilde{\mathbf{u}}}{\partial t} - \mathbf{u} \cdot \nabla \tilde{\mathbf{u}} + \tilde{\mathbf{u}} \cdot (\nabla \mathbf{u})^T + Ri_b \tilde{b} \nabla b = \nabla \tilde{p} + \frac{1}{Re} \nabla^2 \tilde{\mathbf{u}}, \tag{5.6a}$$

$$-\frac{\partial \tilde{b}}{\partial t} - \mathbf{u} \cdot \nabla \tilde{b} = \tilde{w} + \frac{1}{Re} Pr \nabla^2 \tilde{b}, \tag{5.6b}$$

$$\nabla \cdot \tilde{\mathbf{u}} = 0, \tag{5.6c}$$

integrated backwards in time from $t = T$ to $t = 0$. The derivation of these is given in appendix 5.A. Equations (5.5) can be solved to give

$$X_0 = \frac{\Phi_T^\dagger \Phi_T X_0}{\sqrt{\left\langle \Phi_T^\dagger \Phi_T X_0, \Phi_T^\dagger \Phi_T X_0 \right\rangle}} \tag{5.7}$$

at an optimal, which suggests the iterative method

$$X_{n+1} = \frac{\Phi_T^\dagger \Phi_T X_n}{\sqrt{\left\langle \Phi_T^\dagger \Phi_T X_n, \Phi_T^\dagger \Phi_T X_n \right\rangle}}. \tag{5.8}$$

This is in fact precisely the power iteration eigenvalue algorithm to find the eigenvalue of greatest modulus of the linear operator $\Phi_T^\dagger \Phi_T$, and so will converge given a unique such eigenvalue. Since $\Phi_T^\dagger \Phi_T$ is self-adjoint, the eigenvalue will be real. The value of the eigenvalue is given by

$$\lim_{n \to \infty} \left\langle X_n, \Phi_T^\dagger \Phi_T X_n \right\rangle = \lim_{n \to \infty} \langle \Phi_T X_n, \Phi_T X_n \rangle \tag{5.9}$$

which is exactly (twice) the energy growth we wish to maximise. Therefore, so long as the initial guess state has a component in the direction of the optimal, (5.8) will find the maximum energy growth and the state needed to excite it.

5.2.2 Algorithm implementation

Because of the large storage requirements of the two dimensional background state $(\mathbf{u}, b)$, which must be known at every point in time, the following algorithm is used, which employs 'checkpointing':

1. The two dimensional background state is evolved according to (5.1) from $t = 0$ to $t = T$. Every 100 timesteps, the state is stored to disk.
2. An initial perturbation state X_1 is generated randomly. Set $n = 1$.
3. X_n is scaled to have unit energy (required by (5.5a)).
4. The perturbation state X_n is evolved from $t = 0$ to $t = T$ in blocks of 100 timesteps (required by (5.5b)):
    (a) The background state is loaded at the start of the block, and evolved by 100 timesteps according to (5.1), with results at each timestep stored in memory.
    (b) The perturbation state is evolved from the start to the end of the block according to (5.3), using the background states stored in memory.
5. The adjoint state $\tilde{X}_n$ is initialised as the negative of the result of step 4 at $t = T$ (required by (5.5d)).
6. The adjoint state is evolved from $t = T$ to $t = 0$ in blocks of 100 timesteps (required by (5.5c)):
    (a) The background state is loaded at the *start* of the block, and evolved by 100 timesteps according to (5.1), with results at each timestep stored in memory.
    (b) The adjoint state is evolved from the *end* to the *start* of the block according to (5.6), using the background states stored in memory (in reverse order).
7. The next state X_{n+1} is initialised to be the negative of the result of step 5 at $t = 0$.
8. Repeat from step 3 with $n \to n+1$ until the residual $\langle X_{n+1} - X_n, X_{n+1} - X_n \rangle \,/\, \langle X_n, X_n \rangle$ is less than 10^{-6}.

5.3 Results

The equations (5.1), (5.3) and (5.6) are solved on a triply-periodic grid with a pseudo-spectral method. We use 2048 gridpoints in the streamwise (x) direction, with a domain length $L_x = 8\pi$, and 512 gridpoints in the vertical (z) direction, with a domain height of $L_z = 2\pi$. The resolutions in these directions match those employed in the non-turbulent phase of the flow evolution by Howland et al. (2020). In the spanwise (y) direction, only the first two Fourier modes are evaluated, allowing mode-0 (i.e. spanwise independent, exactly two dimensional) disturbances, and mode-1 disturbances, with a wavelength that matches the domain depth L_y. We vary L_y to determine the spanwise wavelength of the fastest growing disturbance. This is a straightforward way of simulating a single Fourier mode with a full pseudo-spectral DNS code (with dealiasing deactivated in this direction) by using only three gridpoints in this direction, and has the added benefit of determining for which wavelengths the spanwise independent optimal grows faster than the mode-1 optimal.

All calculations employ $Re = 5000$, the lowest used by Howland et al. (2020) for computational efficiency and direct comparison; we used $Pr = 1$, again for comparison but also motivated by the fact that in chapter 4 we showed that varying Pr has almost no effect on the linear results; and we used $Ri_b = 1$. In the initial conditions (5.2) we took the wave steepness to be $s = 0.75$ and the wave vector to be $\mathbf{k} = (\frac{1}{4}, 0, 3)$. With this choice, one wavelength in the streamwise direction and three wavelengths in the vertical direction fit within the periodic box.

With this choice of parameters, the phase speed of the wave in the streamwise direction is $k_1\omega/k^2 = \frac{4}{145\sqrt{145}} \approx 0.0023$, which gives two critical layers in the flow, one just below the midline of the domain at $z = \pi$ and the other just above the bottom at $z = 0$. This is just an approximation to the critical layers within a non-uniform flow, see Howland et al. (2020) for a more precise derivation and discussion. Figure 5.1 shows the complex, nonlinear evolution of this flow. A clear amplification of the wave near the central critical layer is apparent, as predicted by classical wave theory. Regions with negative vertical buoyancy gradient are visible near the critical layer after approximately $t = 5$.

We perform direct-adjoint looping with target times $T \in \{5, 10, 20, 30\}$ and $L_y \in [0.1, 1.6]$ (initially with increments of 0.2, with additional calculations where necessary to smooth the curves). The results are shown in figure 5.2. In each case, when the spanwise domain size L_y is sufficiently small, the optimal structures become entirely 2D, and this result is shown as a horizontal line. Howland et al. (2020) used a periodic domain of size $L_y = \pi/2$, so assuming a normal mode structure in this direction, wavelengths $\pi/2$, $\pi/4$, $\pi/6$, etc. are permissible, as well as purely two-dimensional structures. The first six of these possible wavelengths are

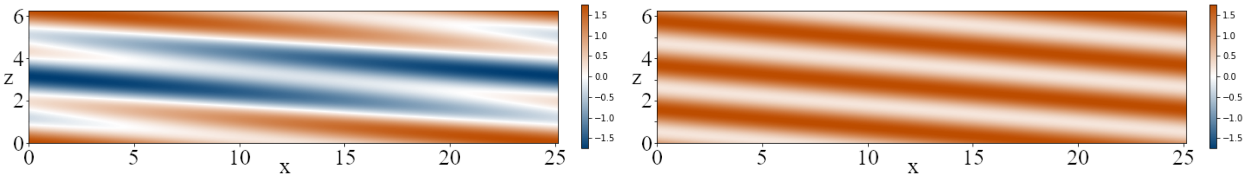

(a) $t = 0$

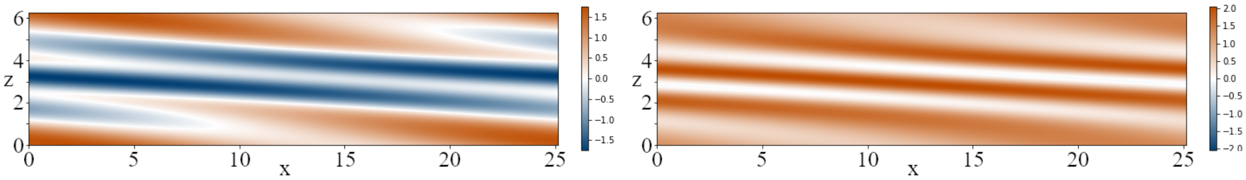

(b) $t = 5$

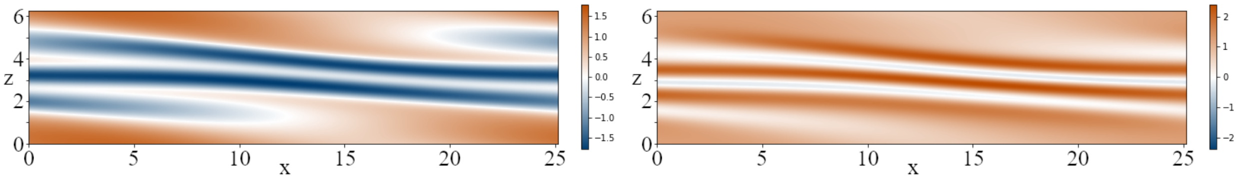

(c) $t = 10$

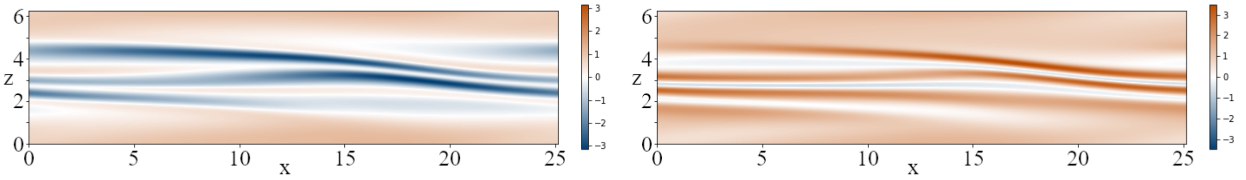

(d) $t = 20$

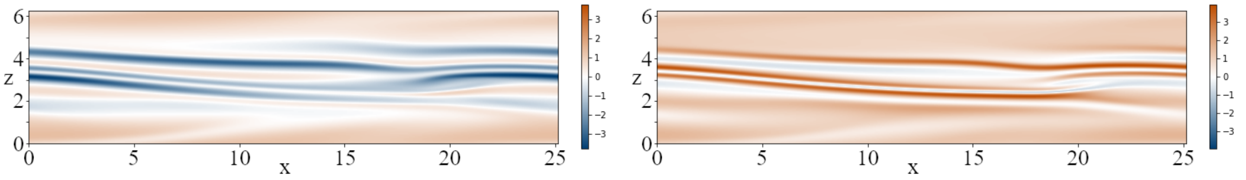

(e) $t = 30$

Fig. 5.1 The complex two-dimensional evolution of the background flow, a superposition of an internal gravity wave and a sinusoidal shear. Left: vorticity $\partial u/\partial z - \partial w/\partial x$. Right: buoyancy gradient $\partial b/\partial z$.

shown as vertical lines on the figures, with the observed wavelength from Howland et al. (2020) shown in red – $\pi/8$, corresponding to a pair of streamwise rolls repeated four times.

Figures 5.3 and 5.4 show the development of the optimal for target time $T = 30$ (see figure 5.2d), in both the 2D case (which was found by the 3D computations for $L_y \leq 0.1$), and the maximal growth case with $L_y = 0.4$. The two figures are typical of the 2D and 3D mechanisms respectively, which are qualitatively completely different from one another.

The 2D optimals, exemplified by figure 5.3, exploit the Orr mechanism, the transient amplification of elongated spanwise vortices as they are rotated by a shear. In this case, two patches of alternating-signed vortices are visible, at locations of high shear within the background flow. These grow in both spatial extent and amplitude as they are sheared and advected by the background. Compared with the 2D optimal for lower target times, the vortex pattern visible is of particularly high wavenumber, which allows the Orr mechanism more time to amplify the disturbance. There does not appear to be any component, in these optimals, of a Kelvin-Helmholtz-type shear instability – which would manifest as spanwise vortices of only one sign which are not visibly sheared as the flow evolves – as opposed to the transient Orr process. At the end of the simulation, the patch of vorticity is located at an area of negative buoyancy gradient in the background flow, and the optimal is therefore exploiting the unstable stratification for energy growth via spanwise counterrotating convective rolls. This was confirmed by the observation that a significant proportion of the energy change (see figure 5.5) was contributed by buoyancy flux in the second half of the simulation.

The 3D optimals, exemplified by figure 5.4, show no evidence of any Orr mechanism, and instead take the form of a single patch of quasi-streamwise-independent, counterrotating, streamwise aligned vortices. As the flow evolves, this patch is advected and significantly amplified. The patch exactly aligns with one of the regions of negative buoyancy gradient in figure 5.1, strongly suggesting that these are indeed convective rolls, being amplified by the statically unstable stratification, though it is likely that the lift-up mechanism (Landahl, 1980) is also being exploited, a viscous algebraic instability of shear flows. Figure 5.5 shows that a large component of the energy growth is driven by the vertical rearrangment of the negative buoyancy gradient, as dense fluid moves down and less dense fluid moves up.

Figure 5.6 shows the energy growth for both of these $T = 30$ optimals. Both optimals, after some initial waviness, show apparently exponential energy growth, suggesting the dominant mechanism in each case is a convective instability, rather than the transient Orr mechanism or the algebraic lift-up mechanism. The 3D optimal is many orders of magnitude more energetic.

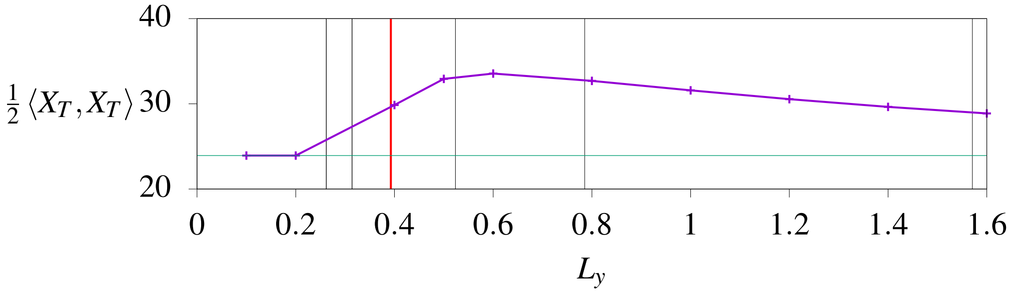

(a) $T = 5$.

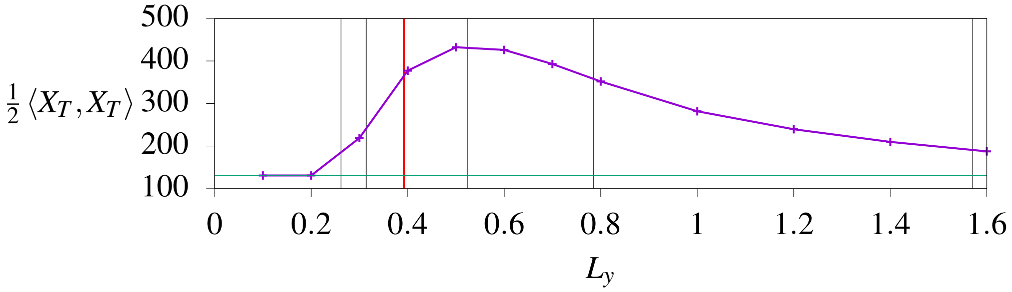

(b) $T = 10$.

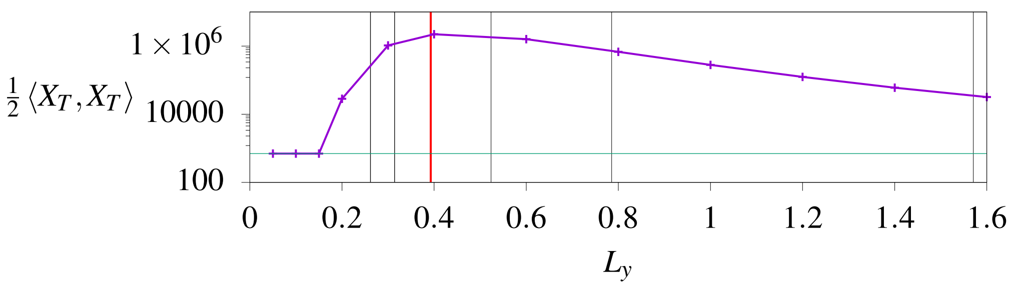

(c) $T = 20$.

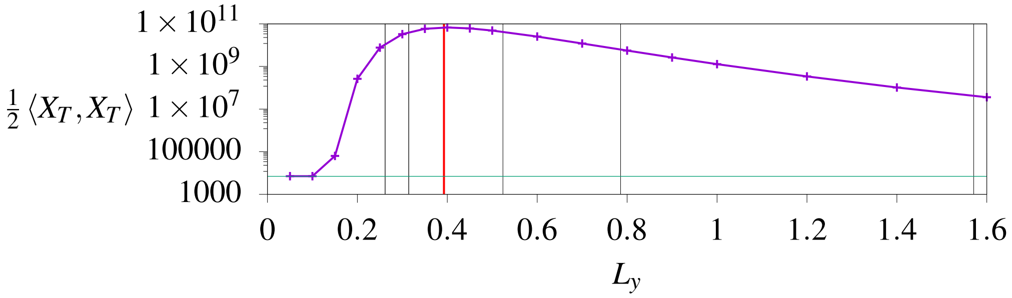

(d) $T = 30$.

Fig. 5.2 Maximum possible final energy of a linear perturbation with initial energy $\frac{1}{2}$, as the spanwise wavelength varies. The vertical lines mark the possible (low wavenumber) wavelengths in the finite-sized periodic box employed by Howland et al. (2020), with the observed wavelength in red. The horizontal line shows the 2D result, which is independent of L_y.

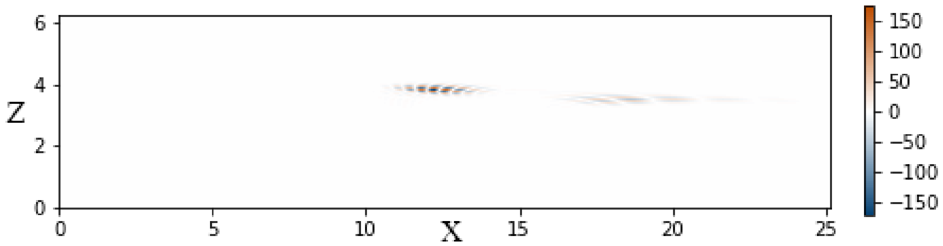

(a) $t = 0$

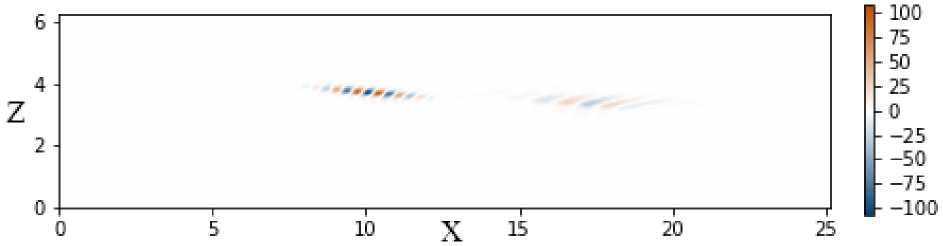

(b) $t = 5$

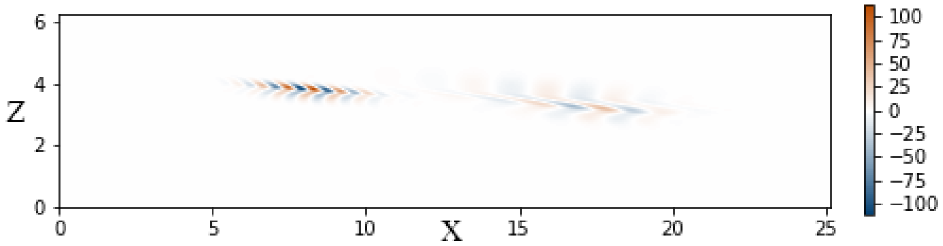

(c) $t = 10$

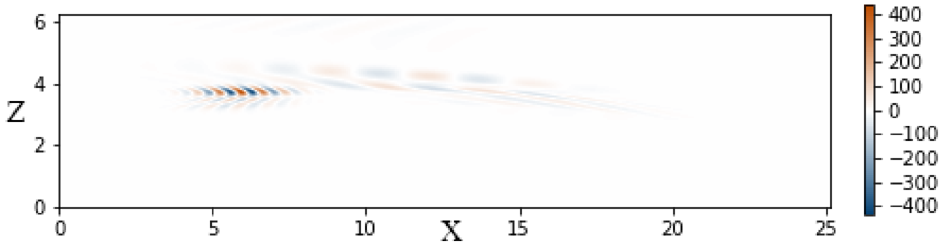

(d) $t = 20$

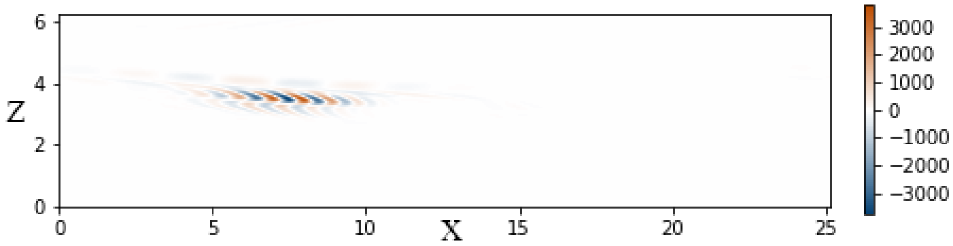

(e) $t = 30$

Fig. 5.3 $x-z$ plane slices of the perturbation spanwise vorticity field $\partial u'/\partial z - \partial w'/\partial x$ for the 2D optimal (calculated using $L_y = 0.1$) with $T = 30$. Alternating spanwise vortices are tilted by the background shear, as is typical of the Orr mechanism.

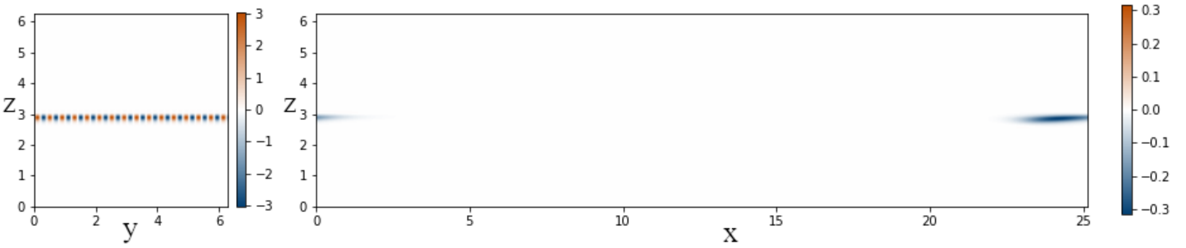

(a) $t = 0$

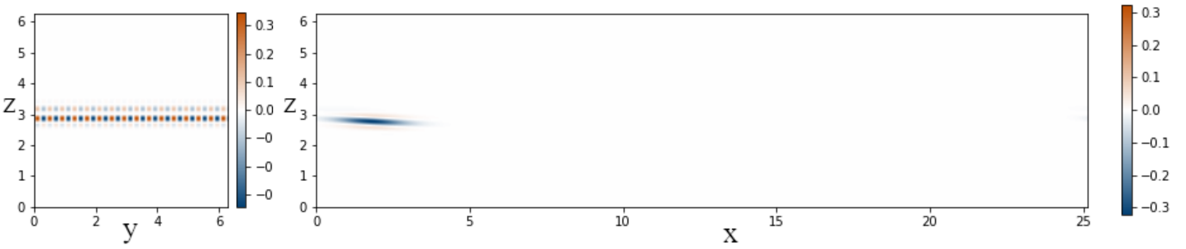

(b) $t = 5$

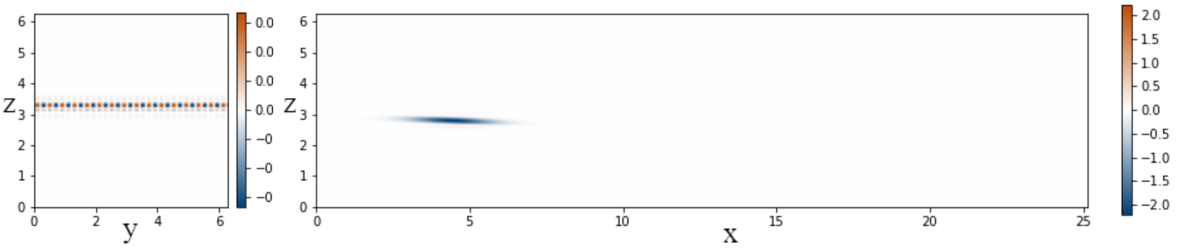

(c) $t = 10$

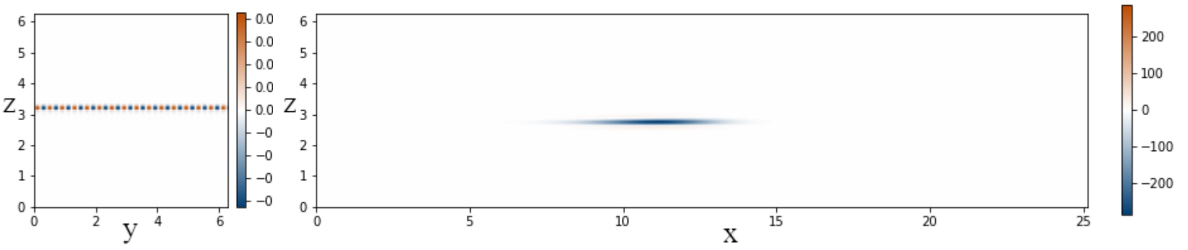

(d) $t = 20$

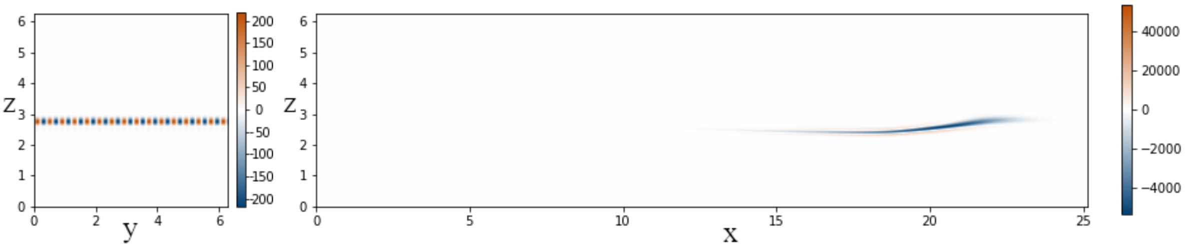

(e) $t = 30$

Fig. 5.4 Slices of the perturbation buoyancy field b' for $L_y = 0.4$ with $T = 30$. On the left, $y-z$ plane slices with $x = 0$, on the right, $x-z$ slices with $y = 0$. The streamwise-aligned vortices are greatly amplified as they are advected.

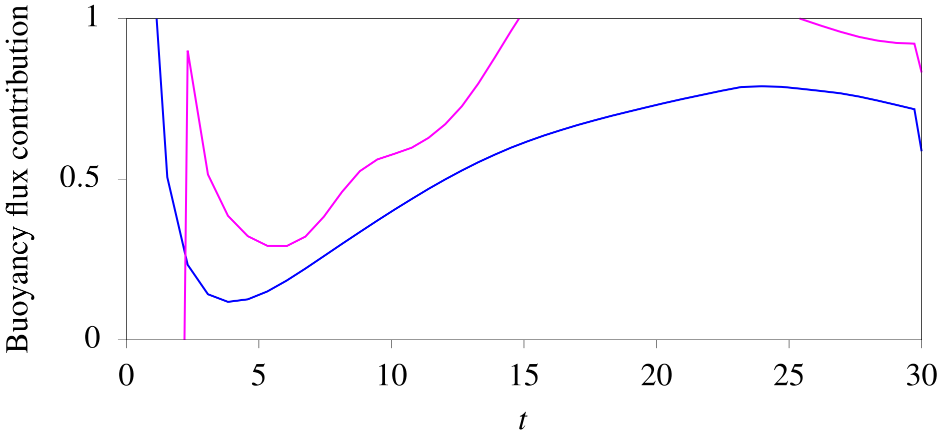

Fig. 5.5 A measure of the relative importance of convection in the energy change. The values on the vertical axis are $\int Ri_b b' w' \,\mathrm{d}V / \frac{d}{\mathrm{d}t} \int \left(\|\mathbf{u}'\|^2 + Ri_b b'^2\right) \mathrm{d}V$, i.e. the proportion of total energy change contributed by the buoyancy flux. This measure can be both greater than one and less than zero depending on other contributions to the energy change. These are for the $T = 30$ optimals (see figure 5.2d). Blue: the 3D optimal computed with $L_y = 0.4$. Pink: the 2D optimal, using $L_y = 0.1$. In both cases, convective effects make a significant impact on the energy growth of the perturbation (see figure 5.6).

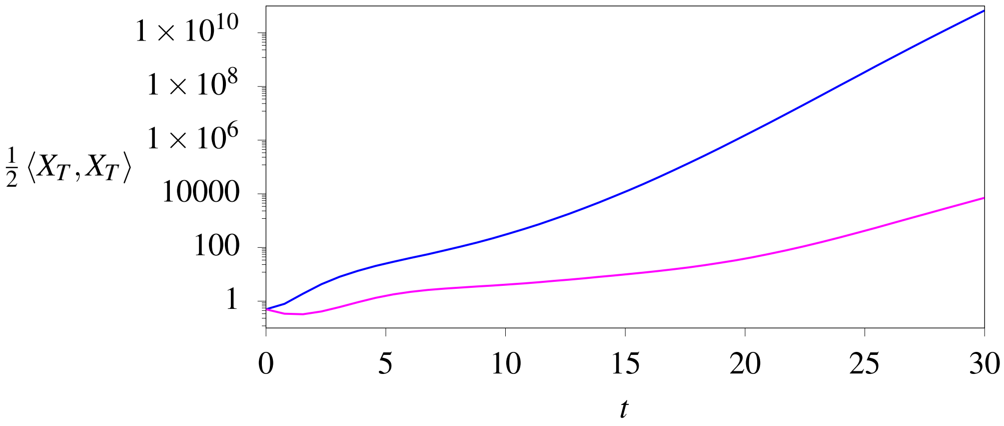

Fig. 5.6 The evolution of the energy for the $T = 30$ optimals (see figure 5.2d). Blue: the 3D optimal computed with $L_y = 0.4$. Pink: the 2D optimal, using $L_y = 0.1$. Both display exponential growth over the time interval, but the 3D is amplified significantly more.

5.4 Conclusion

Our results provide an explanation of the early phase of the simulations described by Howland et al. (2020). For target time $T = 20$, around which time the DNS of Howland et al. (2020) begins to break down into turbulence for the matching parameter values, we see a clear optimal wavelength which matches that found in the DNS (figure 5.2c). The magnitude of the amplification we found, with more than 10^6 times the energy of the original disturbance at $t = 20$, indicates why streamwise rolls are apparent in the simulations: if the initial disturbance has any component of this wavenumber, it is so massively amplified it will necessarily be visible as the simulation progresses. As turbulence develops as a result of this energy growth, the rolls break down and are no longer visible.

We have shown that both spanwise-independent and fully three-dimensional perturbations are able to exploit negative buoyancy gradients which arise in the background flow as the internal wave is amplified near the critical layer, despite the high value of Ri_b which was used. The 3D optimal at the ideal spanwise wavelength of around 0.4 (with $T = 30$) was found to be many orders of magnitude more energetic than the equivalent 2D optimal.

An obvious next step is to repeat the computations at a lower bulk Richardson number Ri_b, which would have the effect of reducing the gradient Richardson numbers within the flow and thereby make shear instabilities, rather than the convective instabilities and transient mechanisms we have observed, more likely.

This study can easily be extended to explore other parameters. The wave steepness s and wavevector $\mathbf{k}$ can both be varied to see the effect. Howland et al. (2020) investigated different s and saw some differences, but those results could be illuminated by repeating our work at the same parameters. Of particular interest is the Prandtl number Pr. We postulate that since the calculations are linear, this will have little effect, as was seen in chapter 4, but there is nevertheless nonlinear interaction with the background flow, so it is worth investigating. This study has focussed on the case of a shear and wave aligned in the same 2D plane, but for a wave coming in obliquely we may well have a qualtitatively different background flow evolution, and thus the optimal perturbations could be quite different. In this oblique case, shear instabilities in particular would be altered. All pertubations were applied at $t = 0$, when the background state is an exact superposition of wave and shear. It would be possible, and perhaps of interest, to instead apply the perturbation at a later time, when the background flow has already evolved in a complex and nonlinear manner. This may give different behaviour, for the same initial pertubation amplitude, if for example, the background flow has already developed a statically unstable region.

Appendix 5.A Derivation of the adjoint equations

Recalling the definitions of the state vectors and operators, equation (5.4) may be rewritten as

$$\begin{aligned}\mathscr{L} = {} & \frac{1}{2}\frac{1}{L_xL_yL_z}\int\left(\mathbf{u}'_T\cdot\mathbf{u}'_T + Ri_b b'_T b'_T\right)\mathrm{d}V + \lambda\left(\frac{1}{2}\frac{1}{L_xL_yL_z}\int\left(\mathbf{u}'_0\cdot\mathbf{u}'_0 + Ri_b b'_0 b'_0\right)\mathrm{d}V - \frac{1}{2}\right)\\ & + \int_0^T \mathrm{d}t\,\frac{1}{L_xL_yL_z}\int\mathrm{d}V\left[\tilde{\mathbf{u}}\cdot\left(\frac{\partial\mathbf{u}'}{\partial t} + \mathbf{u}\cdot\nabla\mathbf{u}' + \mathbf{u}'\cdot\nabla\mathbf{u} + \nabla p' - Ri_b b'\mathbf{e}_z - \frac{1}{Re}\nabla^2\mathbf{u}'\right)\right.\\ & \left. + Ri_b\tilde{b}\left(\frac{\partial b'}{\partial t} + \mathbf{u}\cdot\nabla b' + \mathbf{u}'\cdot\nabla b - \frac{1}{RePr}\nabla^2 b'\right) + \tilde{p}\left(\nabla\cdot\mathbf{u}'\right)\right], \qquad (5.10)\end{aligned}$$

where the adjoint state $\left(\tilde{\mathbf{u}},\tilde{b}\right)$ is now treated as a time-varying Lagrange multiplier state which enforces the evolution of $(\mathbf{u}',b')$ from $\left(\mathbf{u}'_0,b'_0\right)$ to $(\mathbf{u}'_T,b'_T)$ according to (5.3), including the addition of an adjoint pressure $\tilde{p}$ to enforce incompressibility.

Computing the variations of (5.10) with respect to $\mathbf{u}'$, b' and p' we are now able to derive the adjoint equations:

$$\frac{\delta\mathscr{L}}{\delta\mathbf{u}'} = -\frac{\partial\tilde{\mathbf{u}}}{\partial t} - \mathbf{u}\cdot\nabla\tilde{\mathbf{u}} + \tilde{\mathbf{u}}\cdot(\nabla\mathbf{u})^T - \frac{1}{Re}\nabla^2\tilde{\mathbf{u}} + Ri_b\tilde{b}\nabla b - \nabla\tilde{p}, \qquad (5.11)$$

$$\frac{\delta\mathscr{L}}{\delta b'} = -Ri_b\tilde{w} - Ri_b\frac{\partial\tilde{b}}{\partial t} - Ri_b\mathbf{u}\cdot\nabla\tilde{b} - Ri_b\frac{1}{Re}Pr\nabla^2\tilde{b}, \qquad (5.12)$$

$$\frac{\delta\mathscr{L}}{\delta p'} = -\nabla\cdot\tilde{\mathbf{u}}. \qquad (5.13)$$

Equating these expressions with zero quickly gives (5.6).

Chapter 6

Conclusion

6.1 Summary

This thesis has explored some aspects of stratified shear instabilities, particularly motivated by modern issues in oceanography, but from a theoretical and idealised perspective. All four chapters loosely relate to the following question: does the Miles-Howard criterion – the use of $Ri = 1/4$ as a stability boundary – have a theoretical justification when applied in problems of abyssal ocean mixing? Of course, none of this work attempts to check whether it is actually useful in practice, and it could empirically work without a mathematical justification. Nevertheless, the Miles-Howard theorem, from which the criterion is derived, requires several strict restrictions in order to be proven. When these restrictions are relaxed, we have explored whether the criterion is still relevant. Chapters 2, 3 and 4 focused in particular on whether instability, in a loosely defined sense, is possible in stratified shear flows when the minimum Richardson number $Ri_m > 1/4$.

Chapter 2 focused on the most obvious limitation of applying any theorem based on linear stability theory: that in reality no perturbations are infinitesimal, and a finite sized perturbation can lead to complex, chaotic and turbulent behaviours even when the background state is linearly stable. This is the case, for example, in the classical fluid dynamical problem of pressure-driven pipe flow, which is linearly stable (Meseguer and Trefethen, 2003) and yet was famously studied by Reynolds as a simple example of transition and turbulence.

In the chapter, we presented the first direct state tracking and bifurcation analysis in a simple unbounded stratified shear flow, subject to Kelvin-Helmholtz instability. With the introduction of an artificial forcing – as is also implicitly done for any linear stability analysis of this class of viscous flows – we made steady the background flow and tracked the states that arise as a result of the pitchfork bifurcation, with the aim of determining whether this bifurcation is subcritical or supercritical, at $Pr = 1$. It has previously been shown to be supercritical for $Pr < 1$ and subcritical for $Pr > 1$; in the transition between these we described a complex degenerate dynamical system, which did indeed show finite-amplitude, Kelvin-Helmholtz-like billow states to exist above $Ri_m = 1/4$, therefore directly demonstrating that the Miles-Howard criterion does not guarantee simple dynamics in the stable regime.

However, the finite-amplitude states found in chapter 2 extended only very slightly into the linearly stable regime, and therefore the results are of limited relevance to practical geophysical applications; these results are certainly not evidence that KHI-like behaviour can exist significantly above $Ri_b = 1/4$ at $Pr = 1$, though the work of Kaminski et al. (2017) seems to imply it can. The chapter nevertheless presented an interesting application of the state tracking and bifurcation tracking tools which are relatively unknown to this community, and paved the way for the more novel results of chapter 4.

Serendipitously, in the process of chapter 2 we additionally discovered what we have come to call the viscous Holmboe instability, which was studied systematically and described in detail in chapter 3. Since VHI is only present when viscosity is introduced, this instability gives an ideal opportunity to explore another of the Miles-Howard theorem's restrictions, that the flow is inviscid. Although VHI was found in a well-studied model flow, the Holmboe model, it does not exist in the inviscid case, and is very slowly growing once viscosity is introduced. This may explain why it has not been described before, as it could appear to be merely numerical noise at sufficiently high *Re*.

Crucially we found that, for much of parameter space, VHI has no critical layer, which sets it apart from all inviscid instabilities of simple stratified shear flows. This fact clearly demonstrates that the wave overreflection interpretation of shear instabilities must be incomplete, since this relies on the existence of a critical layer, and yet in many other respects the viscous Holmboe instability is similar to classical shear instabilities and so one would expect the physical mechanisms to be the same. In particular, the system still has a density interface and two vorticity interfaces, and the resonant interaction of these, which has been proposed as a different physical interpretation of shear instabilities, could certainly apply in this case. Why a sharp density interface leads to instability in the inviscid limit but viscosity is necessary with a broader interface remains an open question. We demonstrated, through an asymptotic analysis, that the viscous Holmboe instability is a viscous destabilisation of a neutral wave at infinite *Re*, but exactly how this comes about is unclear.

Though we found that VHI exists with broad density interfaces, it is incredibly weak compared with HWI with sharper density interfaces. We were able to demonstrate that it can manifest nonlinearly in carefully controlled situations, but overall VHI is not likely to be found in geophysical situations, and is mainly of academic interest through the light it sheds on other instabilities. VHI was indeed found to exist in regions for which the Miles-Howard criterion would predict stability, but again, does not violate the criterion in a way of practical importance to oceanography.

Chapter 4 revisited the results of chapter 2, but now with $Pr \neq 1$. Despite the relatively small range of Pr considered, $0.7 \leq Pr \leq 7$, very large differences in the dynamical system were found, which was hinted at by the results of weakly-nonlinear studies by Churilov and Shukhman (1987) and others. When considering temperature stratified flows in the oceans, for which $Pr \approx 7$, this model showed significant nonlinear behaviour for $Ri_m > 1/4$, and indeed as high as $Ri_m = 0.65$. Most intriguingly, we found states with half the wavelength of the most unstable mode at the bifurcation point, a wavelength for which there is no linear stability for any value of Ri_m. Direct numerical simulations of an unforced version of the same flow recreated these results, from which we conclude that the structures are not merely a consequence of the artificial forcing. With a qualitatively very similar appearance to classical Kelvin-Helmholtz billows, these structures must presumably form based on the same physical mechanism which gives rise to Kelvin-Helmholtz instability, but nevertheless, for some reason, does not give an instability of the background flow in this case. Unlike in chapters 2 and 3, at $Pr = 7$, which is the relevant case for oceanography, we not only predicted in a theoretical sense but also demostrated using DNS significant KHI-like behaviour well into regions of parameter space for which the Miles-Howard criterion predicts stability. If this behaviour persists in three dimensions it could be of enormous relevance to shear instability in the oceans.

Chapter 5 takes a broader perspective, asking whether we should be thinking about shear instabilities at all. In the specific case of an internal wave approaching a critical layer, where the amplitude is expected to grow and the wave to break, we showed that the dominant energy growth mechanism is a convective one rather than a shear instability. This very closely matched the DNS results of Howland et al. (2020), who nevertheless observed billows reminiscent of KHI later on in the same simulations. Those results suggest that KHI may still be relevant at later times, but we confirmed and distilled the initial instability as a three-dimensional, convective one. Indeed, we showed that even when finding the maximal energy gain at very short target times, the fastest growing three-dimensional structure is highly reminiscent of streamwise-aligned convective rolls near the critical layer, which grow faster than the two dimensional, structure which exploits the Orr mechanism and spanwise convective rolls. At longer target times (on timescales comparable to those observed by Howland et al. (2020)), the 3D optimal gives nearly a factor of 10^7 more energy growth than the 2D optimal. This certainly explains why, so long as initial perturbations exist with sufficiently low wavenumber, streamwise convective rolls are observed in the DNS.

If a convective instability is indeed the primary mechanism for internal wave breaking, a Richardson number test like the Miles-Howard criterion is not at all relevant, rather a criterion based on the local Rayleigh number should be adopted – but of course, this criterion would only ever be satisfied on very small scales, as large scale unstable stratifications do not persist.

6.2 Extensions

Chapters 2, 3 and 4 are restricted to the two-dimensional dynamics that arise from a one-dimensional background flow. Though KHI is an entirely two-dimensional instability, HWI has been found to be three-dimensional in certain circumstances (Smyth and Peltier, 1990). Furthermore, several authors, culminating in Mashayek and Peltier (2012a,b), have catalogued the secondary instabilities which exist on a Kelvin-Helmholtz billow, including many important three-dimensional ones. This, and much DNS evidence, shows that a third dimension is crucial to understand the dynamics following the initial rollup of a billow in KHI. Therefore, there would be great benefit in extending the work of chapters 2 and 4 into three dimensions and tracking the resulting branches, to better understand the dynamics. This would require significantly more compute power, but this is by no means infeasible: the bifurcation analysis was performed on a single CPU of 18 cores, with multiple CPUs used to trace multiple branches concurrently. With a 3D flow, parallelisation becomes more efficient, and this could be scaled up to multiple CPUs used together to trace each branch.

Looking further ahead, the Reynolds number and/or Prandtl number of the calculations could be increased by orders of magnitude to match physical values in the oceans, and even higher Re in the atmosphere. There is accumulating evidence that the nature of the instabilites investigated changes dramatically when $Re \gtrsim 4000$ (Mashayek and Peltier, 2013; Mashayek et al., 2013). It is certainly infeasible to do this using iterative timestepping methods within the next decade or so without access to enormous computational resources and carefully optimised code, but simple DNS studies have shown that the behaviour does indeed increase in complexity (Rahmani et al., 2014; Salehipour et al., 2015), and so when possible, this will be worthwhile.

In chapters 2 and 4 of this thesis we have examined the nonlinear behaviour of Kelvin-Helmholtz instability, and in chapter 3 we studied the linear behaviour of Holmboe instability (and its viscous counterpart). One natural extension would be a bifurcation analysis of HWI and tracking of the exact coherent structures thereof. The nonlinear behaviour of HWI has been studied using DNS (Smyth and Winters, 2003; Alexakis, 2009; Carpenter et al., 2010a; Salehipour et al., 2015) and is has been argued that it could be of great significance in oceanography (Gregg et al., 2018a). Since HWI is a propagating instability, with a non-zero phase speed, the resulting exact coherent structures from the bifurcation, which in this case is a Hopf bifurcation, are periodic orbits. The tracking of periodic orbits is certainly possible using a timestepping approach very similar to that employed in chapters 2 and 4 (it would not be possible to extend a method which directly solves for steady state solutions to the differential equations), but would necessarily be more computationally intensive. The principal model shear flow subject to HWI, the Hazel model, introduces an additional parameter R, the height ratio of the shear layer to the density interface. Tracking of states as both Ri_b and R vary would be of interest. It is conceivable that, nonlinearly, HWI dominates in regimes where the primary linear instability is KHI, or vice versa. This would alter our understanding of such flows in practical GFD applications.

One initial aim of this PhD project was to use *nonlinear* direct-adjoint looping to study shear instabilities. Nonlinear DAL allows one to interrogate, over finite time intervals and for fixed initial perturbation energy, which disturbances maximise a given quantity, such as energy growth. This in turn allows the distillation and examination of the mechanisms and dynamics which govern a flow, as well as more direct applications such as optimisation and control in engineering problems. A combination of code bugs and lack of interesting results (which may have been due to the bugs) meant that this was sidelined in favour of the results presented in the preceding chapters, but this remains of much interest. Several different questions now present themselves for exploration with this technique.

Nonlinear DAL could be applied to determine which mechanisms give the most energy growth (or the most mixing or other relevant metrics) in shear flows which are susceptible to both KHI and HWI. This would add evidence to the arguments about their relative importance in oceanography. In particular, in regions of parameter space where VHI exists, we have a linear instability, which one would normally expect to dominate for sufficiently long target times, but in this case it is so weak that other mechanisms not associated with a linear instability could become important.

Chapter 4 highlighted the importance of carefully considering the value of Pr in nonlinear calculations, in contrast to previous work nonlinear direct-adjoint looping in stratified flows (Eaves and Caulfield, 2015; Kaminski et al., 2017; Marcotte and Caulfield, 2018). With $Pr > 2.3$, it would be of particular interest to see whether the dominant mechanism for energy growth is that of the wavelength predicted by the linear instability, or half this wavelength, as both structures were found to exist in chapter 4. Furthermore, chapter 4 showed complex behaviour in the subcritical $Ri_b > 0.25$ regime, and it would be of great interest if these dynamics were shown to be efficient at mixing when the Miles-Howard criterion implies stability. Necessarily when questions of mixing arise, three-dimensional calculations must be employed, though breakdown to full turbulence means that DAL cannot be relied upon (Pringle et al., 2012), so care would have to be taken in this case.

In chapter 5 we employed linear DAL, but this could easily be extended to the nonlinear version. Indeed, the main difference normally required, the use of checkpointing and reading back the direct field when the adjoint evolution is computed, is also necessary in the case of an evolving background flow, and so is already implemented. It would, however, require the use of a full resolution grid in the spanwise direction, since the Fourier decoupling argument would no longer apply. Introducing nonlinearity in this work would allow use to investigate not only the primary instability mechanism, which we identified as a three-dimensional convective structure, but also the breakdown of this via secondary instabilities. The work which inspired the chapter, Howland et al. (2020), highlighted the development of KH-like billows *after* the initial convective behaviour, which we would hope to capture through nonlinear DAL. By varying the objective function, we could determine whether the convection, the KHI or the transient Orr mechanism is best at optimising energy growth, mixing etc. One problem to be overcome would be the choice of initial perturbation magnitude, which is usually applied as a constraint in DAL. When nonlinearity is introduced, the magnitude has a material impact on the results, and a value would have to be chosen with some geophysical justification.

6.3 Outlook

Ultimately, one assumes that computers will become sufficiently powerful that it is trivial to perform very high resolution DNS, so that any specific physical scenario, as well as large scale climate and ocean modelling, can be calculated with ease. This may seem to remove the need to use algorithmic approaches on idealised models, such as those presented in this thesis. Even when this becomes possible however, idealised situations are still useful to distill the physics, in order to understand the mechanisms at play. However, such computing power is almost inconceivable at the time of writing.

In a shorter time frame, over the next decade or so, the use of machine learning is expected to expand in almost all areas of science, including physical oceanography. Instead of carefully devising parameterisations for abyssal ocean turbulence, on scales too small to be captured by ocean simulations, one could simulate, at very high resolution, a large number of instances of flows, for example near the generation and breaking of internal gravity waves. One could then train a deep neural network to recognise the different situations and output the required metrics such as mixing. This is an immensely powerful tool, but it has the significant disadvantage that it does not enable human understanding of the governing processes, but rather acts as a ‘black box’ which just outputs a number. This, and the fact that neural networks perform badly when tested on data very different from that on which they have been trained, mean that this approach will not be so helpful in predicting extreme events and changes of behaviour that may be expected as the climate changes. For this reason, theoretical, mathematically grounded work like this thesis will remain important for many years to come.

References

Alexakis, A. (2005). On Holmboe's instability for smooth shear and density profiles. *Phys. Fluids*, 17(8):084103.

Alexakis, A. (2007). Marginally unstable Holmboe modes. *Phys. Fluids*, 19(5):054105.

Alexakis, A. (2009). Stratified shear flow instabilities at large Richardson numbers. *Phys. Fluids*, 21(5):054108.

Alford, M. H. and Pinkel, R. (2000). Observations of overturning in the thermocline: The context of ocean mixing. *J. Phys. Oceanogr.*, 30(5):805–832.

Arratia, C., Caulfield, C. P., and Chomaz, J.-M. (2013). Transient perturbation growth in time-dependent mixing layers. *J. Fluid Mech.*, 717:90–133.

Baines, P. G. and Mitsudera, H. (1994). On the mechanism of shear flow instabilities. *J. Fluid Mech.*, 276:327–342.

Baker, M. A. and Gibson, C. H. (1987). Sampling turbulence in the stratified ocean: statistical consequences of strong intermittency. *J. Phys. Oceanogr.*, 17(10):1817–1836.

Betchov, R. and Szewczyk, A. (1963). Stability of a shear layer between parallel streams. *Phys. Fluids*, 6(10):1391–1396.

Bewley, T. R. (2012). *Numerical Renaissance: simulation, optimization, and control.* Renaissance Press.

Booker, J. R. and Bretherton, F. P. (1967). The critical layer for internal gravity waves in a shear flow. *J. Fluid Mech.*, 27(3):513–539.

Boyd, J. P. (2001). *Chebyshev and Fourier spectral methods*. Courier Corporation.

Brown, S. N., Rosen, A. S., and Maslowe, S. A. (1981). The evolution of a quasi-steady critical layer in a stratified viscous shear layer. *Proc. Royal Soc. A*, 375(1761):271–293.

Browning, K. (1971). Structure of the atmosphere in the vicinity of large-amplitude Kelvin-Helmholtz billows. *Q. J. R. Meteorol. Soc.*, 97(413):283–299.

Cairns, R. A. (1979). The role of negative energy waves in some instabilities of parallel flows. *J. Fluid Mech.*, 92:1–14.

Carpenter, J., Tedford, E., Rahmani, M., and Lawrence, G. (2010a). Holmboe wave fields in simulation and experiment. *J. Fluid Mech.*, 648:205.

Carpenter, J. R., Balmforth, N. J., and Lawrence, G. A. (2010b). Identifying unstable modes in stratified shear layers. *Phys. Fluids*, 22(5):054104.

Carpenter, J. R., Tedford, E. W., Heifetz, E., and Lawrence, G. A. (2013). Instability in stratified shear flow: Review of a physical interpretation based on interacting waves. *Appl. Mech. Rev.*, 64(6). 060801.

Caulfield, C. P. (1994). Multiple linear instability of layered stratified shear flow. *J. Fluid Mech.*, 258:255–285.

Caulfield, C. P. and Peltier, W. R. (2000). The anatomy of the mixing transition in homogeneous and stratified free shear layers. *J. Fluid Mech.*, 413:1–47.

Caulfield, C. P., Peltier, W. R., Yoshida, S., and Ohtani, M. (1995). An experimental investigation of the instability of a shear flow with multilayered density stratification. *Phys. Fluids*, 7(12):3028–3041.

Chandler, G. J. and Kerswell, R. R. (2013). Invariant recurrent solutions embedded in a turbulent two-dimensional Kolmogorov flow. *J. Fluid Mech.*, 722:554–595.

Chandrasekhar, S. (1961). *Hydrodynamic and Hydromagnetic Stability*. International series of monographs on physics. Clarendon Press.

Churilov, S. M. (2019). Holmboe instability beyond the Boussinesq approximation revisited. *Phys. Fluids*, 31(9):094104.

Churilov, S. M. and Shukhman, I. G. (1987). Nonlinear stability of a stratified shear flow: a viscous critical layer. *J. Fluid Mech.*, 180:1–20.

Churilov, S. M. and Shukhman, I. G. (1996). The nonlinear critical layer resulting from the spatial or temporal evolution of weakly unstable disturbances in shear flows. *J. Fluid Mech.*, 318:189–221.

Corbett, P. and Bottaro, A. (2000). Optimal perturbations for boundary layers subject to stream-wise pressure gradient. *Phys. Fluids*, 12(1):120–130.

Crowe, M. N. and Taylor, J. R. (2019). The evolution of a front in turbulent thermal wind balance. part 2. numerical simulations. *J. Fluid Mech.*, 880:326–352.

Defina, A., Lanzoni, S., and Susin, F. M. (1999). Stability of a stratified viscous shear flow in a tilted tube. *Phys. Fluids*, 11(2):344–355.

Dijkstra, H. A., Wubs, F. W., Cliffe, A. K., Doedel, E., Dragomirescu, I. F., Eckhardt, B., Gelfgat, A. Y., Hazel, A. L., Lucarini, V., Salinger, A. G., et al. (2014). Numerical bifurcation methods and their application to fluid dynamics: analysis beyond simulation. *Commun. Comput. Phys.*, 15(1):1–45.

Drazin, P. G. (1958). The stability of a shear layer in an unbounded heterogeneous inviscid fluid. *J. Fluid Mech.*, 4(2):214–224.

Eaves, T. and Caulfield, C.-c. P. (2015). Disruption of SSP/VWI states by a stable stratification. *J. Fluid Mech.*, 784:548–564.

Eaves, T. S. and Balmforth, N. J. (2019). Instability of sheared density interfaces. *J. Fluid Mech.*, 860:145–171.

Eaves, T. S. and Caulfield, C. P. (2017). Multiple instability of layered stratified plane Couette flow. *J. Fluid Mech.*, 813:250–278.

Eckhardt, B., Schneider, T. M., Hof, B., and Westerweel, J. (2007). Turbulence transition in pipe flow. *Annu. Rev. Fluid Mech.*, 39:447–468.

Edwards, W. S., Tuckerman, L. S., Friesner, R. A., and Sorensen, D. C. (1994). Krylov methods for the incompressible Navier-Stokes equations. *J. Comput. Phys.*, 110(1):82–102.

Fukao, S., Luce, H., Mega, T., and Yamamoto, M. K. (2011). Extensive studies of large-amplitude Kelvin–Helmholtz billows in the lower atmosphere with VHF middle and upper atmosphere radar. *Q. J. Roy. Meteorol. Soc.*, 137(657):1019–1041.

Garcia, R. V. (1956). Barotropic waves in straight parallel flow with curved velocity profile. *Tellus*, 8(1):82–93.

Gregg, M., D'Asaro, E., Riley, J., and Kunze, E. (2018a). Mixing efficiency in the ocean. *Annu. Rev. Mar. Sci.*, 10:443–473.

Gregg, M. C., D'Asaro, E. A., Riley, J. J., and Kunze, E. (2018b). Mixing efficiency in the ocean. *Annu. Rev. Mar. Sci.*, 10:443–473.

Grossmann, S., Lohse, D., and Sun, C. (2016). High–reynolds number Taylor-Couette turbulence. *Annu. Rev. Fluid Mech.*, 48.

Haines, P. E., Hewitt, R. E., and Hazel, A. L. (2011). The Jeffery-Hamel similarity solution and its relation to flow in a diverging channel. *J. Fluid Mech.*, 687:404–430.

Hazel, P. (1972). Numerical studies of the stability of inviscid stratified shear flows. *J. Fluid Mech.*, 51(1):39–61.

Heifetz, E. and Guha, A. (2018). A generalized action-angle representation of wave interaction in stratified shear flows. *J. Fluid Mech.*, 834:220–236.

Heifetz, E. and Guha, A. (2019). Normal form of synchronization and resonance between vorticity waves in shear flow instability. *Phys. Rev. E*, 100:043105.

Hogg, A. M. and Ivey, G. N. (2003). The Kelvin-Helmholtz to Holmboe instability transition in stratified exchange flows. *J. Fluid Mech.*, 477:339–362.

Holmboe, J. (1960). Unpublished lecture notes.

Holmboe, J. (1962). On the behavior of symmetric waves in stratified shear layers. *Geophys. Publ.*, 24:37.

Howard, L. N. (1961). Note on a paper of John W. Miles. *J. Fluid Mech.*, 10(4):509–512.

Howland, C. J., Taylor, J. R., and Caulfield, C. P. (2018). Testing linear marginal stability in stratified shear layers. *J. Fluid Mech.*, 839.

Howland, C. J., Taylor, J. R., and Caulfield, C. P. (2020). Shear-induced breaking of internal gravity waves. *arXiv e-prints*, page arXiv:2007.09942.

Jones, C. A. (1977). The onset of shear instability in stars. *Geohpys. Astrophys. Fluid Dyn.*, 8(1):165–184.

Kaminski, A. K., Caulfield, C. P., and Taylor, J. R. (2014). Transient growth in strongly stratified shear layers. *J. Fluid Mech.*, 758.

Kaminski, A. K., Caulfield, C. P., and Taylor, J. R. (2017). Nonlinear evolution of linear optimal perturbations of strongly stratified shear layers. *J. Fluid Mech.*, 825:213–244.

Keller, H. B. (1977). Numerical solution of bifurcation and nonlinear eigenvalue problems. In Rabinowitz, P. H., editor, *Applications of Bifurcation Theory*, pages 359–384. Academic Press.

Klaassen, G. P. and Peltier, W. R. (1985). Evolution of finite amplitude Kelvin-Helmholtz billows in two spatial dimensions. *J. Atmos. Sci.*, 42(12):1321–1339.

Kunze, E., Williams III, A., and Briscoe, M. G. (1990). Observations of shear and vertical stability from a neutrally buoyant float. *J. Geophys. Res. Oceans*, 95(C10):18127–18142.

Kutz, J. N., Brunton, S. L., Brunton, B. W., and Proctor, J. L. (2016). *Dynamic Mode Decomposition*. Society for Industrial and Applied Mathematics, Philadelphia, PA.

Landahl, M. (1980). A note on an algebraic instability of inviscid parallel shear flows. *J. Fluid Mech.*, 98(2):243–251.

Lasserre, J. B. (2001). Global optimization with polynomials and the problem of moments. *SIAM J. Optim.*, 11(3):796–817.

Lindzen, R. S. (1988). Instability of plane parallel shear flow (toward a mechanistic picture of how it works). *Pure Appl. Geophys.*, 126(1):103–121.

Lohse, D. and Xia, K.-Q. (2010). Small-scale properties of turbulent Rayleigh-Bénard convection. *Annu. Rev. Fluid Mech.*, 42.

Lombard, P. N. and Riley, J. J. (1996). Instability and breakdown of internal gravity waves. i. linear stability analysis. *Physics of Fluids*, 8(12):3271–3287.

Lott, F. and Teitelbaum, H. (1992). Nonlinear dissipative critical level interaction in a stratified shear flow: Instabilities and gravity waves. *Geophys. Astrophys. Fluid Dyn.*, 66(1-4):133–167.

Luchini, P. (2000). Reynolds-number-independent instability of the boundary layer over a flat surface: optimal perturbations. *J. Fluid Mech.*, 404:289–309.

Mack, S. and Schoeberlein, H. (2004). Richardson number and ocean mixing: Towed chain observations. *J. Phys. Oceanogr.*, 34(4):736–754.

Mallier, R. (2003). Stuart vortices in a stratified mixing layer: the Holmboe model. *J. Eng. Math.*, 47(2):121–136.

Marcotte, F. and Caulfield, C. P. (2018). Optimal mixing in two-dimensional stratified plane poiseuille flow at finite péclet and richardson numbers. *J. Fluid Mech.*, 853:359–385.

Mashayek, A., Caulfield, C., and Peltier, W. (2013). Time-dependent, non-monotonic mixing in stratified turbulent shear flows: implications for oceanographic estimates of buoyancy flux. *J. Fluid Mech.*, 736:570–593.

Mashayek, A. and Peltier, W. (2012a). The 'zoo'of secondary instabilities precursory to stratified shear flow transition. part 1 shear aligned convection, pairing, and braid instabilities. *J. Fluid Mech.*, 708:5.

Mashayek, A. and Peltier, W. (2012b). The 'zoo'of secondary instabilities precursory to stratified shear flow transition. part 2 the influence of stratification. *J. Fluid Mech.*, 708:45.

Mashayek, A. and Peltier, W. (2013). Shear-induced mixing in geophysical flows: does the route to turbulence matter to its efficiency? *J. Fluid Mech.*, 725:216–261.

Mashayek, A. and Peltier, W. R. (2011). Three-dimensionalization of the stratified mixing layer at high Reynolds number. *Phys. Fluids*, 23(11):111701.

Maslowe, S. A. (1973). Finite-amplitude Kelvin-Helmholtz billows. *Bound.-Layer Meteorol.*, 5(1):43–52.

Maslowe, S. A. (1977). Weakly nonlinear stability theory of stratified shear flows. *Q. J. Royal Meteorol. Soc.*, 103(438):769–783.

Maslowe, S. A. (1986). Critical layers in shear flows. *Annu. Rev. Fluid Mech.*, 18(1):405–432.

Mellor, G. L. and Yamada, T. (1982). Development of a turbulence closure model for geophysical fluid problems. *Reviews of Geophysics*, 20(4):851–875.

Meseguer, A. and Trefethen, L. N. (2003). Linearized pipe flow to reynolds number 10^7. *J. Comput. Phys.*, 186(1):178–197.

Mezić, I. (2013). Analysis of fluid flows via spectral properties of the koopman operator. *Annu. Rev. Fluid Mech.*, 45:357–378.

Miles, J. (1986). Richardson's criterion for the stability of stratified shear flow. *The Phys. Fluids*, 29(10):3470–3471.

Miles, J. W. (1961). On the stability of heterogeneous shear flows. *J. Fluid Mech.*, 10(4):496–508.

Miles, J. W. (1963). On the stability of heterogeneous shear flows. Part 2. *J. Fluid Mech.*, 16(2):209–227.

Miller, R. L. and Lindzen, R. S. (1988). Viscous destabilization of stratified shear flow for $Ri > 1/4$. *Geophys. Astrophys. Fluid Dyn.*, 42(1-2):49–91.

Mkhinini, N., Dubos, T., and Drobinski, P. (2013). On the nonlinear destabilization of stably stratified shear flow. *J. Fluid Mech.*, 731:443–460.

Nagata, M. (1990). Three-dimensional finite-amplitude solutions in plane Couette flow: bifurcation from infinity. *J. Fluid Mech.*, 217:519–527.

Net, M. and Sánchez, J. (2015). Continuation of bifurcations of periodic orbits for large-scale systems. *SIAM J. Appl. Dyn. Syst.*, 14(2):674–698.

Parker, J. P., Caulfield, C. P., and Kerswell, R. R. (2019). Kelvin-Helmholtz billows above Richardson number $1/4$. *J. Fluid Mech.*, 879:R1.

Parker, J. P., Caulfield, C. P., and Kerswell, R. R. (2020). The viscous Holmboe instability for smooth shear and density profiles. *J. Fluid Mech.*, 896:A14.

Parrilo, P. A. (2003). Semidefinite programming relaxations for semialgebraic problems. *Math. Program.*, 96(2):293–320.

Polzin, K. (1996). Statistics of the Richardson number: Mixing models and finestructure. *J. Phys. Oceanogr.*, 26(8):1409–1425.

Pouliquen, O., Chomaz, J. M., and Huerre, P. (1994). Propagating Holmboe waves at the interface between two immiscible fluids. *J. Fluid Mech.*, 266:277–302.

Preusse, M., Peeters, F., and Lorke, A. (2010). Internal waves and the generation of turbulence in the thermocline of a large lake. *Limnol. Oceanogr.*, 55(6):2353–2365.

Pringle, C. C., Willis, A. P., and Kerswell, R. R. (2012). Minimal seeds for shear flow turbulence: using nonlinear transient growth to touch the edge of chaos. *J. Fluid Mech.*, 702:415.

Rahmani, M., Lawrence, G., and Seymour, B. (2014). The effect of Reynolds number on mixing in Kelvin–Helmholtz billows. *J. Fluid Mech.*, 759:612–641.

Rahmani, M., Seymour, B. R., and Lawrence, G. A. (2016). The effect of Prandtl number on mixing in low Reynolds number Kelvin-Helmholtz billows. *Phys. Fluids*, 28(5):054107.

Saad, Y. and Schultz, M. H. (1986). GMRES: A generalized minimal residual algorithm for solving nonsymmetric linear systems. *SIAM J. Sci. Comput.*, 7(3):856–869.

Salehipour, H., Caulfield, C. P., and Peltier, W. R. (2016). Turbulent mixing due to the Holmboe wave instability at high Reynolds number. *J. Fluid Mech.*, 803:591–621.

Salehipour, H., Peltier, W. R., and Mashayek, A. (2015). Turbulent diapycnal mixing in stratified shear flows: the influence of Prandtl number on mixing efficiency and transition at high Reynolds number. *J. Fluid Mech.*, 773:178–223.

Salinger, A. G., Bou-Rabee, N. M., Pawlowski, R. P., Wilkes, E. D., Burroughs, E. A., Lehoucq, R. B., and Romero, L. A. (2002). LOCA 1.0 Library of Continuation Algorithms: theory and implementation manual. *Sandia National Laboratories, SAND2002-0396.*

Sánchez, J. and Net, M. (2016). Numerical continuation methods for large-scale dissipative dynamical systems. *Eur. Phys. J. Spec. Top.*, 225(13):2465–2486.

Schmid, P. J. (2007). Nonmodal stability theory. *Annu. Rev. Fluid Mech.*, 39:129–162.

Schmid, P. J. (2010). Dynamic mode decomposition of numerical and experimental data. *J. Fluid Mech.*, 656:5–28.

Schmid, P. J. and Henningson, D. S. (2001). *Stability and transition in shear flows*. Applied Mathematical Sciences (Springer-Verlag New York Inc.).

Schneider, T. M., Eckhardt, B., and Yorke, J. A. (2007). Turbulence transition and the edge of chaos in pipe flow. *Phys. Rev. Lett.*, 99(3):034502.

Shi, J., Tong, C., Zheng, J., Zhang, C., and Gao, X. (2019). Kelvin-Helmholtz billows induced by shear instability along the north passage of the Yangtze river estuary, china. *J. Mar. Sci. Eng.*, 7(4):92.

Smyth, W. and Moum, J. (2013). Marginal instability and deep cycle turbulence in the eastern equatorial pacific ocean. *Geophys. Res. Lett.*, 40(23):6181–6185.

Smyth, W. D. and Carpenter, J. R. (2019). *Instability in Geophysical Flows*. Cambridge University Press.

Smyth, W. D., Klaassen, G. P., and Peltier, W. R. (1988). Finite amplitude Holmboe waves. *Geophys. Astrophys. Fluid Dyn.*, 43(2):181–222.

Smyth, W. D. and Moum, J. N. (2012). Ocean mixing by Kelvin-Helmholtz instability. *Oceanography*, 25(2):140–149.

Smyth, W. D., Nash, J. D., and Moum, J. N. (2019). Self-organized criticality in geophysical turbulence. *Sci. Rep.*, 9(1):3747.

Smyth, W. D. and Peltier, W. R. (1989). The transition between Kelvin-Helmholtz and Holmboe instability: an investigation of the overreflection hypothesis. *J. Atmospheric Sci.*, 46(24):3698–3720.

Smyth, W. D. and Peltier, W. R. (1990). Three-dimensional primary instabilities of a stratified, dissipative, parallel flow. *Geophys. Astrophys. Fluid Mech.*, 52(4):249–261.

Smyth, W. D. and Peltier, W. R. (1991). Instability and transition in finite-amplitude Kelvin-Helmholtz and Holmboe waves. *J. Fluid Mech.*, 228:387–415.

Smyth, W. D. and Winters, K. B. (2003). Turbulence and Mixing in Holmboe Waves. *J. Phys. Oceanogr.*, 33(4):694–711.

Squire, H. B. (1933). On the stability for three-dimensional disturbances of viscous fluid flow between parallel walls. *Proc. Royal Soc. A*, 142(847):621–628.

Stamper, M. A. and Taylor, J. R. (2017). The transition from symmetric to baroclinic instability in the Eady model. *Ocean Dyn.*, 67(1):65–80.

Strogatz, S. H. (2014). *Nonlinear dynamics and chaos: with applications to physics, biology, chemistry, and engineering*. CRC Press.

Sun, J., Nappo, C. J., Mahrt, L., Belušić, D., Grisogono, B., Stauffer, D. R., Pulido, M., Staquet, C., Jiang, Q., Pouquet, A., et al. (2015). Review of wave-turbulence interactions in the stable atmospheric boundary layer. *Rev. Geophys*, 53(3):956–993.

Taylor, G. I. (1931). Effect of variation in density on the stability of superposed streams of fluid. *Proc. Royal Soc. Lond. A*, 132(820):499–523.

Taylor, J. R. (2008). *Numerical simulations of the stratified oceanic bottom layer*. PhD thesis.

Taylor, J. R. and Ferrari, R. (2009). On the equilibration of a symmetrically unstable front via a secondary shear instability. *J. Fluid Mech.*, 622:103–113.

Thorpe, S. and Liu, Z. (2009). Marginal instability? *J. Phys. Oceanogr.*, 39(9):2373–2381.

Thorpe, S. A. (2005). *The Turbulent Ocean*. Cambridge University Press.

Thorpe, S. A., Smyth, W. D., and Li, L. (2013). The effect of small viscosity and diffusivity on the marginal stability of stably stratified shear flows. *J. Fluid Mech.*, 731:461–476.

Troitskaya, Y. I. (1991). The viscous-diffusion nonlinear critical layer in a stratified shear flow. *J. Fluid Mech.*, 233:25–48.

Umurhan, O. M. and Heifetz, E. (2007). Holmboe modes revisited. *Phys. Fluids*, 19(6):064102.

Van Haren, H. and Gostiaux, L. (2010). A deep-ocean Kelvin-Helmholtz billow train. *Geophys. Res. Lett.*, 37(3).

Witzke, V., Silvers, L. J., and Favier, B. (2015). Shear instabilities in a fully compressible polytropic atmosphere. *Astron. Astrophys.*, 577:A76.

Wray, A. A. (1986). Very low storage time-advancement schemes. Technical report, Internal Report, Moffett Field, CA, NASA-Ames Research Center.

Wunsch, C. and Ferrari, R. (2004). Vertical mixing, energy, and the general circulation of the oceans. *Annu. Rev. Fluid Mech.*, 36:281–314.

Yih, C.-S. (1955). Stability of two-dimensional parallel flows for three-dimensional disturbances. *Wart. Appl. Math.*, 12:434–435.

Appendix A

The design and validation of Stratiflow

Stratiflow is the direct numerical simulation code, and the various high level algorithms which sit on top of it, written for, and as part of, this PhD. It was specifically designed for handling stratified shear flows in two and three dimensions. The code itself is entirely new, written in C++, using the matplotlibcpp (https://github.com/lava/matplotlib-cpp) and FFTW (http://www.fftw.org/) external libraries for plotting and Fourier transforms respectively, with OpenMP multithreading. The design is object-oriented and modular, so that the DNS code can be modified without altering the Newton solver, or vice versa, for example. Multiple executables can be compiled at the same time for different purposes, such as straightforward simulation, Arnoldi iteration or simply measuring metrics of saved states. The code is designed so that different cases can be run without recompiling the code (except for changes in grid size, which for efficiency reasons is hard-coded at compile time). The latest version of the code is available on GitHub (https://github.com/Jezz0r/Stratiflow).

The DNS code evolved over the course of the PhD, but essentially two versions were used. In chapters 2, 3 and 4, the streamwise (and, where used, the spanwise) direction is periodic and handled pseudospectrally, switching between a Fourier modal and spatially nodal representation as necessary. The vertical direction in these chapters, which is finite with stress-free, insulating boundaries some distance above and below the shear, is handled with finite differences. This was chosen, over a Chebyshev pseudospectral method, because of the ability to concentrate gridpoints near the centre of the domain, which is particularly useful for situations studied which model unbounded flows, where boundary effects are unimportant. In chapter 5, a different version of the code, which uses a Fourier pseudospectral representation in all three directions, was employed. Here we present a validation against a reference case for the doubly-periodic version, the triply-periodic case just replicates this code in the final direction.

The design of the solver is based heavily on that described in Bewley (2012). The temporal discretisation uses a third-order Runge-Kutta-Wray (RKW3) algorithm (Wray, 1986) which requires relatively low memory usage for the accuracy of the algorithm. The viscous terms are handled implicitly using the Crank-Nicolson method at each RKW3 substep, the pressure is implicit via a projection method, and nonlinear and forcing terms are handled explicitly, all as described by Bewley (2012).

The vertical discretisation makes use of 'quasi-second-order' derivatives, i.e. schemes which would be exactly second-order on a uniform grid, but a non-uniform grid are strictly only first order. This is done so that mass, momentum and energy are all explicitly conserved numerically. The vertical velocity is stored on a grid which is staggered with respect to the other variables, to avoid checkerboarding artifacts. In all cases, homogeneous Dirichlet boundary conditions are applied to the vertical velocity, and homogeneous Neumann boundary conditions are applied to the other variables. In the case of a linear background buoyancy stratification, this is handled via a body force rather than being captured in the variables, and where necessary is added back for visualisation. The spectral dimensions employ a 'two-thirds rule' (Boyd, 2001) for filtering, to remove aliasing artifacts which arise from nonlinear terms, though this is disabled on the spanwise direction in chapter 5, as there are no nonlinear terms in this linearised version.

Stratiflow was validated against DIABLO (Taylor, 2008), a FORTRAN code also based upon the algorithms given in Bewley (2012), which has been used in a number of publications, both in simple stratified shear flows (Kaminski et al., 2014, 2017; Howland et al., 2018) and other areas of physical oceanography (e.g. Taylor and Ferrari, 2009; Stamper and Taylor, 2017; Crowe and Taylor, 2019). Though the timestepping algorithms are designed to be the same between Stratiflow and DIABLO, there are a number of differences in the test cases. The DIABLO reference was run using a fixed small timestep, whereas Stratiflow uses its own adaptive timestepping. Although both codes use finite differences in the vertical direction, the precise grid is different, with Stratiflow using the gridpoints described in chapter 4. Another key difference is that in Stratiflow, background one-dimensional velocity and buoyancy profiles are handled separately from the perturbation flow fields, so that these can be held steady or allowed to diffuse as necessary.

The test flow used for validation was chosen arbitrarily as an easy-to-implement initial condition which gives complex flow evolution. The initial conditions are:

$$\begin{aligned}\mathbf{u} &= \tanh z\,\mathbf{e}_x,\\ b &= z + \cos(2y)\cos(0.5x)\operatorname{sech} z.\end{aligned}$$

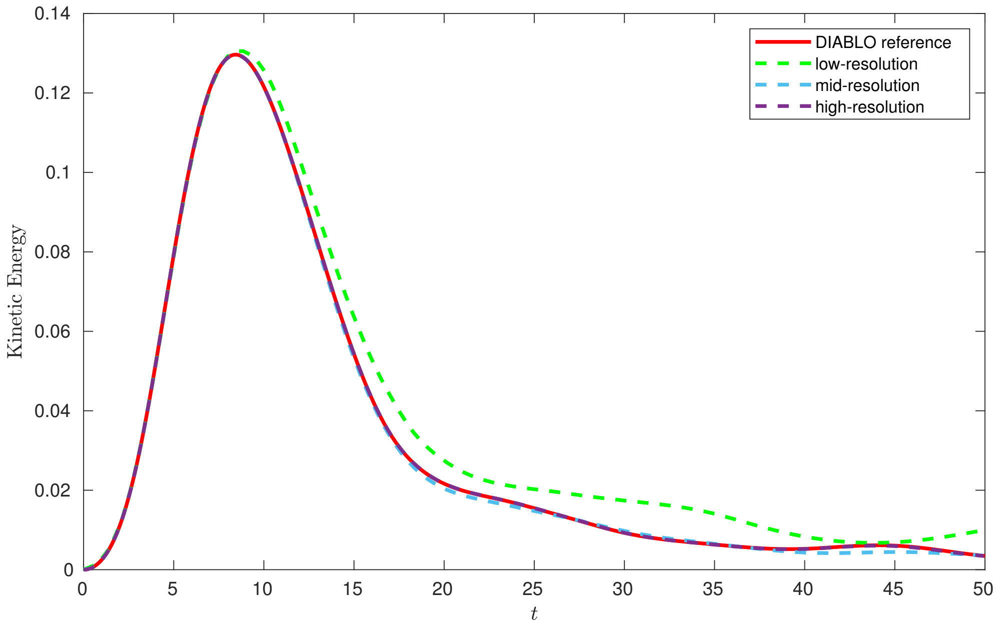

Fig. A.1 Comparison of the kinetic energy (with the one-dimensional component removed) between Stratiflow test cases and the DIABLO reference. The variability in the latter half of the simulations shows the complex nature of the flow here, but nevertheless, the high-resolution case is indistinguishable from the reference.

This can be viewed as the Drazin model (see chapters 2 and 4) with a large finite-amplitude perturbation in the buoyancy field. The flow parameters used are as follows: $Re = 1000$, $L_x = 4\pi$, $L_z = 10$, $L_y = \pi$, $Ri = 0.1$, $Pr = 1.5$. It is important here to use $Pr \neq 1$, since values of unity can hide code bugs. At these values, the basic flow is unstable to KHI, though the dynamics are largely caused by the perturation. The flows were simulated to $t = 50$, during which time there is an initial high-energy ‘roll-up’ and subsequent complex (and probably chaotic) behaviour.

For the DIABLO reference case, we used $N_x = 256$, $N_y = 64$ and $N_z = 256$ (using the notation followed throughout this thesis, rather than the DIABLO convention which has y and z exchanged), and a fixed timestep of 0.005, which gives a CFL number much lower than strictly necessary. Stratiflow was run at $(N_x, N_y, N_z) = (64, 16, 64)$, $(128, 32, 128)$, and $(256, 64, 256)$, which we will call respectively low-, mid- and high-resolution, with the variable timestepping, based on a CFL condition, as used in the rest of the thesis.

Figure A.1 shows a comparison of the results. The metric used, for ease of comparison between the different codes, is the kinetic energy of the flow with the one-dimensional means

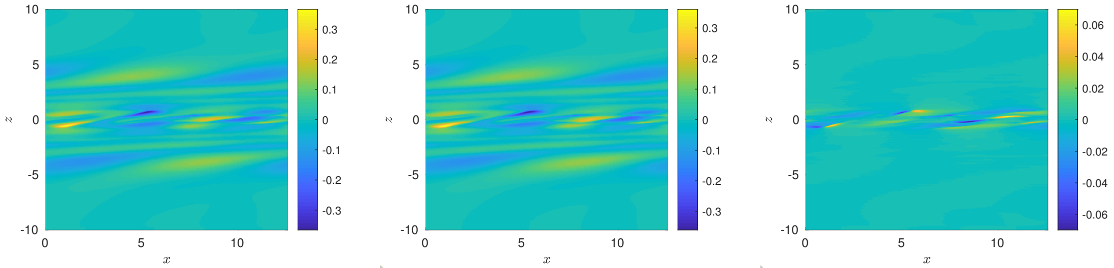

Fig. A.2 Comparison of the buoyancy fields (with the one-dimensional component removed) at $t = 50$. Left: DIABLO reference. Centre: High-resolution Stratiflow. Right: Difference.

subtracted, i.e.

$$\frac{1}{L_x L_y}\int_0^{L_x} \mathrm{d}x \int_0^{L_y} \mathrm{d}y \int_{-L_z}^{L_z} \mathrm{d}z \frac{1}{2}\left((u-U)^2+(v-V)^2+(w-W)^2\right),$$

where $U(z) = \frac{1}{L_x L_y}\int_0^{L_x} \mathrm{d}x \int_0^{L_y} \mathrm{d}y\, u(x,y,z)$ etc. Though this metric does not include the buoyancy field or the background profiles, the tight coupling between these variables in the equations means that if this metric agrees, the others certainly will also. The high-resolution results are indistinguishable from the DIABLO reference, despite the complex nature of the flow, and the differences in the DNS algorithms. The mid-resolution run shows some differences late in the simulation but broadly agrees. Even the low-resolution results, which is on a much coarser grid than any used in the preceding chapters, captures the general behaviour of the flow.

Figure A.2 shows a comparison of the buoyancy field, at the end of the simulation, between the high-resolution run and the reference. Visually, the two would seem to be identical, but upon subtracting them, relatively large errors (up to 20 percent) are apparent in the field. Here, for comparison, both results have been linearly reinterpolated from their non-uniform grids on to a grid which is uniformly spaced in z. In areas of high gradient in the field, this reinterpolation can introduce large differences, which appears to be what is happening in the figure.

Overall, Stratiflow shows good agreement with the mature DIABLO code, in a complex, three-dimensional case, and therefore can certainly be trusted in the simpler two-dimensional cases, often at higher resolution, which are discussed in the thesis.

Two other versions of the DNS were developed. A linearised version, which removes nonlinear interactions between the perturbation and itself, was validated against very low amplitude perturbations in the full nonlinear DNS. The adjoint equations, as discussed in chapter 5, were implemented in their own solver (which shares most of the code with the main solver). This is harder to validate, though we are confident the implementation is correct, as the power-iteration algorithm converges and the expected objective functional obeys the expected convergence properties. Therefore, we deduce that the adjoint code we have implemented is indeed the adjoint of the main code.

Appendix B

Koopman analysis of isolated fronts and solitons[1]

---

[1] This chapter is a slightly modified version of Parker, J. P. & Page, J., Koopman analysis of isolated fronts and solitons. To appear in *SIAM Journal on Applied Dynamical Systems*.

Abstract

A Koopman decomposition of a complex system leads to a representation in which nonlinear dynamics appear to be linear. The existence of a linear framework with which to analyse nonlinear dynamical systems brings new strategies for prediction and control, while the approach is straightforward to apply to large datasets using dynamic mode decomposition (DMD). However, it can be challenging to connect the output of DMD to a Koopman analysis since there are relatively few analytical results available, while the DMD algorithm itself is known to struggle in situations involving the propagation of a localised structure through the domain. Motivated by these issues, we derive a series of Koopman decompositions for localised, finite-amplitude solutions of classical nonlinear PDEs for which transformations to linear systems exist. We demonstrate that nonlinear travelling wave solutions to both the Burgers and KdV equations have *two* Koopman decompositions; one of which converges upstream and another which converges the other downstream of the soliton or front. These results are shown to generalise to the interaction of multiple solitons in the KdV equation. The existence of multiple expansions in space and time has a critical impact on the ability of DMD to extract Koopman eigenvalues and modes – which must be performed within a temporally and spatially localised window to correctly identify the separate expansions. We provide evidence that these features may be generic for isolated nonlinear structures by applying DMD to a moving breather solution of the sine-Gordon equation.

B.1 Introduction

Dynamic mode decomposition (DMD), invented by Schmid (2010), has emerged as an increasingly popular *linear* tool with which to analyse *nonlinear* dynamical systems. The DMD algorithm yields a representation in which the state of the system is expressed as a superposition of fixed coherent structures (DMD modes) with an exponential dependence on time. DMD has primarily been applied in fluid mechanics (e.g. Schmid et al., 2010; Jovanović et al., 2014; Kutz et al., 2016) but is also increasingly being used in other areas, for example in neuroscience (Brunton et al., 2016a). While the output of the DMD algorithm is straightforward to interpret, it has additional theoretical significance owing to a connection with the Koopman operator (Koopman, 1931; Mezić, 2005) for the underlying dynamical system. Through this connection, DMD modes can be shown to be related to simple invariant solutions of the system (e.g. equilibria, periodic orbits Mezic, 2017; Page and Kerswell, 2018, 2020). The objective of this paper is to establish some generic rules for applying DMD to spatially-extended nonlinear systems by deriving analytical Koopman decompositions for the state variable in some classical integrable nonlinear PDEs.

The Koopman operator (Koopman, 1931) is a linear operator acting on the space of observables for nonlinear systems, allowing us to perform spectral decompositions in the usual way (Rowley et al., 2009; Mezić, 2013). The resulting Koopman decompositions (or expansions) of observables, and in particular the state of the system, cast the evolution as a sum of spatial Koopman modes with exponential temporal behaviour. This is possible via a projection of the observable of interest onto Koopman *eigenfunctions* (strictly speaking, eigenfunctionals, though we follow the standard nomenclature here), scalar functionals of the state of the system which have a 'linear' evolution despite the underlying nonlinear dynamics. In this perspective, the fixed Koopman modes assume a secondary importance despite their physical significance, and can be regarded as the coefficients in the expansion (Rowley et al., 2009; Mezić, 2013). In a series of important contributions, various authors have identified strict requirements under which DMD is capable of performing a Koopman mode decomposition (Rowley et al., 2009; Tu et al., 2014; Williams et al., 2015; Brunton et al., 2016b; Rowley and Dawson, 2017).

The DMD algorithm is straightforward to apply to very complex systems since it requires only a sequence of snapshot pairs as input. However, it is often difficult to verify that the low-rank dynamics identified in DMD correspond to a Koopman decomposition due to a lack of analytical results beyond ODE model problems (e.g. Bagheri, 2013; Brunton et al., 2016b; Rowley and Dawson, 2017). Some of these ODE results have allowed extraction of Koopman modes in more complex nonlinear PDEs, e.g. the Stuart-Landau equation describes the transient collapse of unstable flow past a cylinder onto a limit cycle, and this connection allowed Bagheri (2013) to find the corresponding Koopman modes for the velocity field. Certain nonlinear PDEs can also be rendered linear under a transformation of the state variable which allows for identification of Koopman eigenvalues (e.g. Page and Kerswell, 2018; Kutz et al., 2018; Nakao and Mezić, 2020). Page and Kerswell (2018) exploited the linearising transform to derive a full Koopman decomposition for the velocity field in the Burgers equation. In this work we exploit a similar feature in the KdV equation to derive Koopman decompositions there.

Beyond DMD, a variety of alternative methods to extract Koopman decompositions have been proposed. For example, Sharma et al. (2016) have found a connection between Koopman modes and the ‘response modes’ of the resolvent operator. In statistically stationary flows, Arbabi and Mezić (2017) have demonstrated an approach motivated by signal processing to allow for extraction of Koopman modes and eigenfunctions. Other approaches involve altering the snapshots on which DMD is applied, by adding additional functionals (observables) of the state of the system (Williams et al., 2015) or by ‘stacking’ snapshots of the state equispaced-in-time along the trajectory to form a single large observable (Brunton et al., 2017).

However, despite this progress there are still open questions as to how Koopman and DMD should be applied to systems which transit between multiple simple invariant solutions (Brunton et al., 2016b; Page and Kerswell, 2019). In fact, Koopman analysis applied to a simple ODE with a pair of fixed points (Page and Kerswell, 2019) has shown that each simple invariant solution has an associated Koopman expansion. Each expansion is convergent up to a crossover point along the heteroclinic connection between the fixed points. This introduces a critical constraint on DMD, which to function as a proxy for Koopman must be performed on an observation window in which there is a single valid decomposition. In addition, it is known that the DMD algorithm struggles when applied to localised travelling waves (e.g. Kutz et al., 2016) both in providing a low rank approximation to the dynamics and in extrapolating beyond the observation window. Our analysis of the KdV equation suggests that these two behaviours may be related, as we show that localised nonlinear waves possess multiple Koopman decompositions, each of which converges in different regions of space-time. For DMD to extract the different expansions, observations must be restricted in both time and space to a region where a single expansion holds.

The remainder of this paper is structured as follows. In section B.2 we introduce the Koopman operator and derive a pair of Koopman decompositions for a travelling-front solution of the Burgers equation. In section B.3 we perform a similar analysis for a one-soliton solution of the KdV equation, before using the inverse scattering transform to derive Koopman eigenfunctions, eigenvalues and modes for general (non-dispersive) solutions to the KdV equation, establishing the need for potentially many different Koopman decompositions in a generic case. The consequences of these decompositions for DMD are examined in section B.4, and an observable that can robustly determine Koopman eigenvalues and modes is defined. We then apply DMD to find Koopman decompositions of the sine-Gordon equation, where the analytical decomposition is unknown. Finally, concluding remarks are provided in section B.5.

B.2 Koopman decompositions of nonlinear dynamics

In this paper we will consider nonlinear PDEs of the form

$$\partial_t u = F(u), \tag{B.1}$$

for some F, with time forward map $f^t(u) = u + \int_0^t F(u)\mathrm{d}t'$. At a given time, $u : \mathbb{R} \to \mathbb{R}$ describes the current state of the system, and is a member of the relevant Sobolev solution space W for the given PDE.

The (one parameter family of) Koopman operator(s) $\mathscr{K}^t$ acts on the vector space of all nonlinear functionals g well defined on the solution space of the PDE, so that $g : W \to \mathbb{R}$. Such functionals are often termed 'observables'. The Koopman operator acts by shifting observables along a trajectory of eq. (B.1),

$$\mathscr{K}^t g(u) := g(f^t(u)). \tag{B.2}$$

This perspective is useful due to the linearity of the Koopman operator. In particular, the eigenfunctions of $\mathscr{K}^t$ are scalar observables with an exponential dependence on time,

$$\mathscr{K}^t \varphi_\lambda(u) = \varphi_\lambda(f^t(u)) := \varphi_\lambda(u)e^{\lambda t}, \tag{B.3}$$

and therefore constitute a coordinate system for representing arbitrary observables in which the nonlinear evolution *appears* to be linear,

$$\mathscr{K}^t g(u) = g(f^t(u)) = \sum_{n=0}^{\infty} \varphi_{\lambda_n}(u)e^{\lambda_n t}\hat{g}_n, \tag{B.4}$$

where $\hat{g}_n$ are Koopman modes for the observable g.

Often the desire is to find a representation like eq. (B.4) for the function describing the state itself, u, so that for equation eq. (B.1),

$$u(x) = \sum_{n=0}^{\infty} \varphi_{\lambda_n}(u)\hat{u}_n(x). \tag{B.5}$$

In this notation, u is viewed as a family of observables *parameterised* by x.

Though $u \in W$, there is no guarantee that the Koopman modes $\hat{u}_n : \mathbb{R} \to \mathbb{R}$ satisfy the smoothness conditions for W or that such a sum will converge for all of $\mathbb{R}$. The recent work by Page and Kerswell (2019) demonstrated that separate Koopman decompositions eq. (B.5) can be constructed around simple invariant solutions of eq. (B.1), and in general multiple decompositions will be required for a given trajectory as it wanders between unstable exact solutions. In this work our focus is on spatially localised dynamics, which typically require multiple Koopman decompositions in both time *and* space to represent the full nonlinear evolution.

B.2.1 Motivating example: a front in the Burgers equation

The Burgers equation was considered by Page and Kerswell (2018), who used the Cole-Hopf transformation to derive a Koopman decomposition for the state variable u. In that study, only trajectories running down to the trivial solution were considered. Here, our focus is on travelling waves. The Burgers equation is defined by,

$$F(u) := -u\partial_x u + \nu \partial_x^2 u, \tag{B.6}$$

and supports a variety of equilibria and travelling wave solutions (Benton and Platzman, 1972). We consider boundary conditions $u(x \to -\infty) = U_\infty$ and $u(x \to \infty) = 0$, which admits a solution of a right-propagating front

$$u(x,t) = c\left[1 - \tanh\left(\frac{c}{2\nu}(x - ct)\right)\right], \tag{B.7}$$

where the propagation speed $c := U_\infty/2$.

In the approach of Page and Kerswell (2018), Koopman eigenfunctions for the Burgers equation were obtained by exploiting the Cole-Hopf transformation and performing a Koopman mode decomposition (KMD) of the linearising variable. A KMD for the velocity field was then found by inverting this transformation. While such an approach should also be possible here, we instead derive the KMD(s) for the propagating front via a Laplace transform approach (Page and Kerswell, 2019). This approach is more appropriate here, as it identifies regions in the $x-t$ plane where a particular KMD is convergent.

In Page and Kerswell (2018) it was shown that the Koopman eigenvalues of the Burgers equation are all real. We adopt the following ansatz for the velocity field:

$$u(x,t) = \int_{-\infty}^{\infty} v(-\lambda;x)\varphi_{-\lambda}(u)e^{-\lambda t}\mathrm{d}\lambda, \tag{B.8}$$

where $v(\lambda;x)$ is a Koopman mode *density* for the observable u, which is parameterised by x. In dynamical systems evolving on an attractor, our approach can be modified by assuming λ to be purely imaginary. In this approach, the Koopman mode density is simply the Fourier transform of the state variable (Mezić, 2013).

Equation eq. (B.8) is a bilateral Laplace transform with time as the transform variable. The Koopman mode density can be obtained by inverting the transform by integration along a Bromwich contour in the complex-t plane,

$$\begin{aligned} v(-\lambda;x)\varphi_{-\lambda}(u) &= \frac{1}{2\pi i}\int_{\gamma-i\infty}^{\gamma+i\infty} u(x,t)e^{\lambda t}\mathrm{d}t \\ &= \frac{c}{\pi i}\int_{\gamma-i\infty}^{\gamma+i\infty} \frac{e^{\lambda t}}{1+\exp\left[\frac{c}{\nu}(x-ct)\right]}\mathrm{d}t. \end{aligned} \tag{B.9}$$

For this inversion to be possible, u must have a valid analytic continuation into the complex plane, which is the case for this example. We note that we are using the time variable of the dynamical system as the transform variable in the Laplace transform, which is the opposite of the usual approach.

For unilateral Laplace transforms, convergence is assured by selecting γ to lie to the right of the singularities of the integrand. For the bilateral transform, γ can be selected to the right or left of the singularities (the contour then closed to the left or right respectively) provided that the Koopman mode density vanishes below or above a critical value of λ respectively (Page and Kerswell, 2019). This results in two possible Koopman mode densities. In practice, one is associated with exponentially decaying Koopman eigenvalues, the other with exponential growth.

The inversion integrand eq. (B.9) has simple poles at $t_n = x/c + i\pi(2n+1)\nu/c^2$, $n \in \mathbb{Z}$. The inversion can therefore be accomplished by selecting either $\gamma > x/c$ and closing to right or $\gamma < x/c$ and closing to the left, a choice which yields a convergent KMD either upstream ($x < ct$) or downstream ($x > ct$) of the front. The solution procedure is almost identical for both cases, and we discuss only the upstream calculation in detail.

For the upstream expansion, $\gamma > x/c$, we close the contour in a large semicircle to the *left*. The contribution to the integral from the semicircular contour vanishes for $\lambda > -c^2/\nu$, hence the corresponding Koopman mode density has support for $\lambda \in (-c^2/\nu,\infty)$ and the upstream KMD is

$$u(x,t) = \int_{-c^2/\nu}^{\infty} v_-(-\lambda;x)\varphi_{-\lambda}(u)e^{-\lambda t}\mathrm{d}\lambda, \tag{B.10}$$

where

$$\begin{aligned} v_-(-\lambda;x)\varphi_{-\lambda}(u) &= \frac{c}{\pi i}\oint_C \frac{e^{\lambda t}}{1+\exp\left[\frac{c}{\nu}(x-ct)\right]}\mathrm{d}t \\ &= 2c\sum_{n=-\infty}^{\infty} \operatorname{Res}\left(\frac{e^{\lambda t}}{1+\exp\left[\frac{c}{\nu}(x-ct)\right]}, t_n\right), \end{aligned} \tag{B.11}$$

where C is the closed contour built from the Bromwich contour and the large semicircle. Evaluating the residues at the poles, we find

$$\begin{aligned} v_-(-\lambda;x)\varphi_{-\lambda}(u) &= 2c\sum_{n=-\infty}^{\infty}\frac{\nu}{c^2}\exp\left[\lambda\left(\frac{x}{c}+i\pi(2n+1)\frac{\nu}{c^2}\right)\right] \\ &= \frac{2\nu}{c}(-1)^{\lambda\nu/c^2}\exp\left(\frac{\lambda x}{c}\right)\sum_{k=-\infty}^{\infty}\delta\left(k-\frac{\lambda\nu}{c^2}\right), \end{aligned} \tag{B.12}$$

using the identity for generalised functions $\sum_n e^{2\pi int} = \sum_k \delta(k-t)$. Inserting the upstream density in eq. (B.10) yields the upstream KMD,

$$u(x,t) = 2c\sum_{k=0}^{\infty}(-1)^k\exp\left[\frac{kc}{\nu}(x-ct)\right], \tag{B.13}$$

valid for $x < ct$, with Koopman eigenvalues $-kc^2/\nu$.

A similar approach with $\gamma < x/c$ yields

$$v_+(-\lambda;x)\varphi_{-\lambda}(u) = -\frac{2\nu}{c}(-1)^{\lambda\nu/c^2}\exp\left(\frac{\lambda x}{c}\right)\sum_{k=-\infty}^{\infty}\delta\left(k-\frac{\lambda\nu}{c^2}\right), \tag{B.14}$$

with the KMD for the velocity downstream

$$\begin{aligned} u(x,t) &= \int_{-\infty}^{0} v_+(-\lambda;x)\varphi_{-\lambda}(u)e^{-\lambda t}\mathrm{d}\lambda \\ &= -2c\sum_{k=1}^{\infty}(-1)^k\exp\left[-\frac{kc}{\nu}(x-ct)\right], \end{aligned} \tag{B.15}$$

valid for $x > ct$. Both the downstream expansion eq. (B.15) and the upstream expansion eq. (B.13), truncated at $N = 10$ terms, are overlayed onto the true travelling front solution in figure fig. B.1. The loss of convergence in both expansions at $x - ct = 0$ is clear.

There is a simple dynamical systems interpretation to the results above: under the ansatz of travelling-wave dynamics $u = f(x-ct)$, the Burgers equation with these boundary conditions reduces to a simple one-dimensional (nonlinear) ordinary differential equation $f' = \frac{1}{2\nu}f^2 - \frac{c}{\nu}f$. The front depicted in fig. B.1 is a heteroclinic connection between the (unstable) trivial solution at $f = 0$ and the (stable) equilibrium $f = U_\infty = 2c$. The pair of Koopman decompositions found above thus corresponds to expansions about these two equilibria, which both breakdown at the same "crossover point" in state space (see also Page and Kerswell, 2019). These equilibria have one-dimensional linear subspaces, and the associated Koopman decompositions begin with eigenvalues corresponding to these

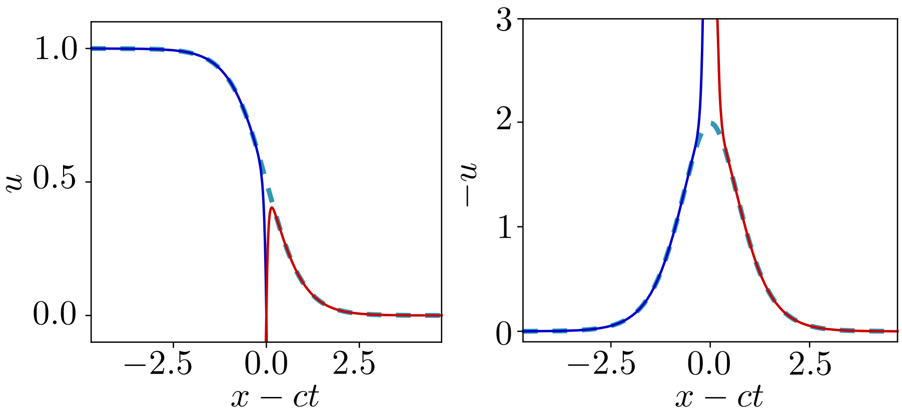

Fig. B.1 Simple travelling wave solutions to the Burgers (left) and KdV (right) equations visualised in a co-moving frame along with the respective upstream (blue) and downstream (red) Koopman expansions. Series are truncated at $N = 10$ in all cases.

unstable/stable linear dynamics, $\mp c^2/\nu$. The higher order terms in the expansion then correspond to integer powers of the associated Koopman eigenfunction.

B.3 Koopman decomposition of Korteweg-de-Vries equation

The Korteweg-de-Vries (KdV) equation is the canonical and simplest example of a nonlinear dispersive wave equation. It is defined by

$$F(u) := -\partial_x^3 u + 6u\partial_x u. \tag{B.16}$$

The term $\partial_x^3 u$ makes this a dispersive wave equation, and $u\partial_x u$ is a nonlinear self-advection term. Equation eq. (B.16) naturally arises as the inclusion of simple nonlinearity in a number of wave phenomena, including internal waves in a stratified fluid. We consider the KdV equation on the real line with boundary conditions $u \to 0$ as $x \to \pm\infty$.

In an early example of the numerical solution of PDEs, Zabusky and Kruskal (1965) simulated the KdV equation and discovered the rich behaviour of so-called ‘solitons’. These exact coherent structures of the PDE are strongly stable. They can interact with one another and preserve their form post-interaction. The behaviour of solitons led to the development of the inverse scattering transform (IST), which can be used to analytically solve KdV as well as a number of other, more complicated, so-called ‘integrable’ equations.

B.3.1 Single-soliton solution

The canonical one-soliton solution to KdV is given by

$$u(x,t) = -2\operatorname{sech}^2(x-4t), \tag{B.17}$$

which is a simple travelling wave propagating to the right. Note that $u < 0$, which is the case for all soliton solutions of eq. (B.16).

We will follow the methodology outlined for the front in the Burgers equation in section B.2.1 and assume that the Koopman eigenvalues required to described the evolution of eq. (B.17) are real. This assumption will be justified section B.3.3, where we derive the Koopman eigenfunctions required to describe arbitrary soliton evolutions.

Expressing the evolution as an integral over a Koopman mode *density* (see section B.2.1), $v(\lambda;x)$,

$$-2\operatorname{sech}^2(x-4t) = \int_{-\infty}^{\infty} v(-\lambda;x)\varphi_{-\lambda}(u)e^{-\lambda t}\mathrm{d}\lambda. \tag{B.18}$$

This Laplace transform (transform variable t) can be inverted in the normal way to give

$$\begin{aligned} v(-\lambda;x)\varphi_{-\lambda}(u) &= \frac{1}{2\pi i}\int_{\gamma-i\infty}^{\gamma+i\infty} -2\operatorname{sech}^2(x-4t)\,e^{\lambda t}\mathrm{d}t \\ &= -\frac{1}{\pi i}\int_{x-4\gamma-i\infty}^{x-4\gamma+i\infty} \frac{e^{\lambda(x-\xi)/4}}{\left(e^{\xi}+e^{-\xi}\right)^2}\mathrm{d}\xi, \end{aligned} \tag{B.19}$$

where $\xi := x-4t$. Similar to the Burgers equation example presented in section B.2.1, we can close the contour for this integral in two different directions, yielding a pair Koopman decompositions which hold upstream/downstream of the soliton.

Closing the contour to the left, we label the Koopman modes as v_+, with $v_+(\lambda;x) = 0$ for $\lambda > 2$. Then eq. (B.18) becomes

$$-2\operatorname{sech}^2(x-4t) = \int_{-\infty}^{2} v_+(-\lambda;x)\varphi_{-\lambda}(u)e^{-\lambda t}\mathrm{d}\lambda. \tag{B.20}$$

Equation eq. (B.19) has second order poles at $\xi_n = i\pi(2n+1)/2$, $n \in \mathbb{Z}$. The residue theorem gives, for $\lambda < 2$,

$$\begin{aligned} v_+(-\lambda;x)\varphi_{-\lambda}(u) &= -2\sum_{n=-\infty}^{\infty} \operatorname{Res}\left(\frac{e^{\lambda(x-\xi)/4}}{\left(e^{\xi}+e^{-\xi}\right)^2}, i\pi(2n+1)/2\right) \\ &= -\lambda e^{\lambda x/4}e^{-i\pi\lambda/8}\sum_{k=-\infty}^{\infty}\delta\left(8k-\lambda\right). \end{aligned} \tag{B.21}$$

Substituting this into eq. (B.20), we find a decomposition

$$-2\operatorname{sech}^2(x-4t) = \sum_{k=1}^{\infty} 8k(-1)^k e^{-2kx} e^{8kt}. \tag{B.22}$$

This expansion involves Koopman eigenvalues $\{8k : k \in \mathbb{N}\}$, with corresponding Koopman modes e^{-2kx}. In this derivation, it is not possible to determine the Koopman eigenfunctions $\{\varphi_\lambda(u)\}$ in their general form.

Equation eq. (B.22) is a convergent expansion for $x > 4t$, i.e. downstream of the peak of the soliton. Analogous behaviour was seen in the front solution to Burgers equation (e.g. eq. (B.13)), which suggests that the need for multiple Koopman decompositions to describe nonlinear wave evolution is generic. The upstream expansion for the one soliton solution to KdV can be obtained by closing the contour to the right, which yields

$$2\operatorname{sech}^2(x-4t) = \sum_{k=1}^{\infty} 8k(-1)^k e^{2kx} e^{-8kt}, \tag{B.23}$$

which could also be anticipated from symmetry. The upstream expansion is convergent for $x < 4t$ and involves Koopman eigenvalues $\{-8k : k \in \mathbb{N}\}$ – temporally decaying modes.

Similar to the Burgers equation, there is a simple dynamical systems interpretation to these results which rests on the fact that Koopman expansions appear to be defined about simple invariant solutions of the governing equation, and connecting orbits between such solutions contain a crossover point where one expansion fails and another takes over. Supposing that $u = f(x - ct)$ for some c, the KdV equation with $u \to 0$ as $x \to \infty$ boundary conditions reduces to the two-dimensional ODE

$$f' = g, \tag{B.24a}$$

$$g' = 3f^2 + cf, \tag{B.24b}$$

where we have defined $g = f'$. For $c > 0$, this system has a centre at $f = -c/3$, $g = 0$, which does not satisfy our boundary conditions, and a saddle point at $f = 0$, $g = 0$, the trivial zero solution of KdV. The one soliton solution for this particular value of c is a homoclinic orbit from the latter fixed point back to itself, encircling the centre at $f = -c/3$. The crossover point at $x = ct$ divides the trajectory into a ‘repelling’ and an ‘attracting’ section. The Koopman expansions for these sections of the orbit are built from eigenfunctions which are integer powers of the Koopman eigenfunctions associated with the linear subspace around $u = 0$ and have eigenvalues $\pm\sqrt{c}$ (i.e. $\pm c^{3/2}$ in the lab frame)

These effects have interesting consequences for describing more complex dynamics – soliton interactions – in terms of Koopman expansions. In order to generalise the approach above, we will use the inverse scattering transform (e.g. Drazin and Johnson, 1989) to derive Koopman eigenfunctions for the KdV equation in their general form, which will allow us to examine these more interesting situations.

B.3.2 Inverse scattering method

The inverse scattering method is one the most celebrated results of twentieth century mathematics. It can be used to solve a variety of nonlinear PDEs, including the nonlinear Schrödinger equation and the sine-Gordon equation (Ablowitz et al., 1974). In the inverse scattering approach, the solution to the nonlinear PDE, $u(x,t)$, is treated as a potential in a linear scattering problem in which time appears parametrically. It can be shown that the scattering data (the eigensolutions of the scattering problem) evolve *linearly* as $u(x,t)$ evolves according to its nonlinear evolution equation. Therefore, the scattering data can be obtained for all time from the initial condition $u(x,0)$ alone. The solution to the nonlinear PDE at any time can then be extracted from the scattering data via an inverse scattering transform, which amounts to the solution of a linear integral equation. The existence of a linearising transform allows us to derive Koopman eigenfunctions, which can then be used to construct Koopman decompositions for the state variable itself.

Here we concentrate on the specific case of KdV, for which the inverse scattering method was first developed (Gardner et al., 1967). Throughout, we follow the notation and conventions of Drazin and Johnson (1989). Let $u_0(x)$ be some initial condition for the KdV equation on the real line, with $u_0(x) \to 0$ as $x \to \pm\infty$. The time evolution can then be obtained as follows:

1. Solve the eigenvalue Sturm-Liouville scattering problem $\psi_{xx} + (\lambda - u_0)\psi = 0$. The eigenvalue spectrum has a discrete negative part $\lambda = -\kappa_n^2$ for $n = 1, 2, \ldots, N$, and a continuous positive part $\lambda = k^2$. The eigenvalues and their corresponding eigenfunctions are called the 'scattering data'.

2. It is then possible to predict how the scattering data will evolve as u evolves from u_0 according to the KdV equation. In particular, it is sufficient to consider the 'reflection coefficient' $b(k)$ for the continuous spectrum and $\{c_n\}$ for the discrete spectrum. These are defined by requiring that the eigenfunctions $\psi \sim e^{-ikx} + b(k)e^{ikx}$ or $\psi \sim c_n e^{-\kappa_n x}$ as $x \to \infty$. The latter (discrete) case is normalised so that $\int_{-\infty}^{\infty} \psi^2 \mathrm{d}x = 1$.

The scattering data evolve according to the linear equations

$$\frac{\mathrm{d}b}{\mathrm{d}t} = 8ik^3 b, \tag{B.25a}$$

$$\frac{\mathrm{d}c_n}{\mathrm{d}t} = 4\kappa_n^3 c_n, \tag{B.25b}$$

as the potential $u(x)$ evolves according to the KdV equation.

3. Given the scattering data at initial time, one can then calculate $u(x,t)$ at some future time t through 'inverse scattering', which amounts to solving the Marchenko equation,

$$K(x,z,t) + F(x+z,t) + \int_x^\infty K(x,y,t)F(y+z,t)\mathrm{d}y = 0, \tag{B.26}$$

for K, where

$$F(x,t) = \sum_{n=1}^{N} c_n^2 \exp\left(8\kappa_n^3 t - \kappa_n x\right) + \frac{1}{2\pi}\int_{-\infty}^{\infty} b(k)\exp\left(8ik^3 t + ikx\right)\mathrm{d}x.$$

In all but the simplest cases, this must be done numerically. The velocity is then obtained via $u(x,t) = -2\left(\partial_x K(x,z,t)|_{z=x} + \partial_z K(x,z,t)|_{z=x}\right)$.

B.3.3 Koopman eigenpairs of the KdV equation

With the inverse scattering transform in mind, we now define a family of observables $c_\kappa(u)$, where κ is a positive real number, on the state space for the unbounded KdV equation. The value of $c_\kappa(u)$, a real number, can be computed as follows: First, determine whether the ordinary differential equation $\psi_{xx} - (\kappa^2 + u(x))\psi = 0$ has a non-trivial, square-integrable solution, with ψ decaying exponentially as $x \to \pm\infty$. If it does, the solution is made unique by requiring $\int_{-\infty}^{\infty} \psi^2 \mathrm{d}x = 1$. In the limit $x \to \infty$, $\psi \sim Ae^{-\kappa x}$ for some A, which allows us to define $c_\kappa(u) = A$. If there is no solution to the Sturm-Liouville problem, define $c_\kappa(u) = 0$. Although this does not give a closed-form, explicit expression for c_κ in terms of u, it defines a functional valid for any state in the solution space of the equation.

Due to their linear evolution equations eq. (B.25b), it is clear that the scattering data are Koopman eigenfunctions of the nonlinear KdV equation,

$$\mathscr{K}^t c_\kappa(u) = c_\kappa(f^t(u)) = e^{4\kappa^3 t} c_\kappa(u), \tag{B.27}$$

i.e. $c_\kappa(u) = \varphi_{\lambda_\kappa}(u)$, the Koopman eigenfunction with Koopman eigenvalue $\lambda_\kappa = 4\kappa^3$.

We note that the same approach can be used to construct a family of Koopman eigenfunctions with purely imaginary Koopman eigenvalues from the reflection coefficients $b(k)$ associated with the continuous spectrum of the scattering problem. Because of difficulties solving the integral equation in cases where $b(k) \neq 0$, we consider only ‘reflectionless potentials’ where $b(k) \equiv 0$.

Since the scattering data are sufficient to reconstruct the whole solution to the KdV equation, we therefore assume that these Koopman eigenpairs, and their products, as discussed below, are sufficient to find decompositions.

B.3.4 Single-soliton revisited

Before examining soliton interactions, we will first revisit the one soliton solution of the KdV equation considered in section B.3.1,

$$u(x,0) = -2\,\mathrm{sech}^2 x, \tag{B.28}$$

and use knowledge of the Koopman eigenfunctions and the inverse scattering approach to construct the Koopman decompositions. From our family of Koopman eigenfunctions c_κ, only $c_1(u)$ is non-zero in this case, with $c_1(u_0) = \sqrt{2}$, and there is no continuous spectrum in the scattering problem. However, note that c_κ can be raised to any power a to give a Koopman eigenfunction with Koopman eigenvalue $4a\kappa^3$ (Mezić, 2013).

Initially, we introduce as an ansatz a Koopman decomposition using only positive integer powers of $c_1(u)$ – i.e. one associated with exponential growth in time. We will see that this approach yields the upstream expansion eq. (B.22) found via the Laplace transform approach in section B.3.1. Rather than seeking a decomposition for $u(x)$ directly, we first decompose $K(x,z)$, the solution to the Marchenko equation described in section B.3.2. With our ansatz, we write

$$K(u;x,z) = \sum_{n=1}^{\infty} \hat{K}_n(x,z) c_1^n(u) = \sum_{n=1}^{\infty} \hat{K}_n(x,z) c_1^n(u_0) e^{4nt}, \tag{B.29}$$

where $c_1^n(u_0) = 2^{n/2}$. Note the change in notation to reflect that K is an observable of the state, u, parameterised by x and z. The Marchenko equation eq. (B.26) now reads

$$\sum_{n=1}^{\infty} \hat{K}_n(x,z) c_1^n(u_0) e^{4nt} + 2e^{8t-x-z} + \int_x^{\infty} \sum_{n=1}^{\infty} \hat{K}_n(x,y) c_1^n(u_0) e^{4nt} 2e^{8t-y-z} \mathrm{d}y = 0.$$

Examining the z dependence of the terms, it is apparent that $\hat{K}_n(x,z) = \hat{L}_n(x)e^{-z}$ for some $\hat{L}_n(x)$. We can therefore perform the integration, to give

$$\sum_{n=1}^{\infty} \hat{L}_n(x)c_1^n(u_0)e^{4nt} + 2e^{8t-x} + \sum_{n=1}^{\infty} \hat{L}_n(x)c_1^n(u_0)e^{(8+4n)t-2x} = 0.$$

Comparing coefficients of e^{4pt}, we have

$$\hat{L}_p(x)c_1^p(u_0) + \hat{L}_{p-2}(x)c_1^{p-2}(u_0)e^{-2x} = \begin{cases} -2e^{-x}, & p = 2, \\ 0, & \text{otherwise.} \end{cases}$$

Assuming that the Koopman modes associated with the exponentially decaying eigenfunctions not included in the ansatz ($c_1^{-n}(u_0)$) are zero, $\hat{L}_n(x) = 0$ for $n < 0$, this recurrence may be solved directly to give

$$\hat{L}_n(x) = \begin{cases} 0, & n \text{ odd,} \\ (-1)^{n/2}2^{1-n/2}e^{-(n-1)x}, & n \text{ even.} \end{cases} \tag{B.30}$$

The resulting Koopman decomposition for K is then

$$K(u;x,z) = \sum_{n=1}^{\infty} (-1)^n 2^{1-n} e^{-(2n-1)x-z} c_1^{2n}(u_0)e^{8nt}, \tag{B.31}$$

and a Koopman decomposition for u can be obtained from $u = -2\left(\partial_x K|_{z=x} + \partial_z K|_{z=x}\right)$, giving

$$\begin{aligned} u(x,t) &= \sum_{n=1}^{\infty} (-1)^n 2^{3-n} e^{-2nx} c_1^{2n}(u_0)e^{8nt}, \\ &= \sum_{n=1}^{\infty} (-1)^n 8n e^{-2n(x-4t)}. \end{aligned} \tag{B.32}$$

This is a Koopman decomposition, using Koopman eigenfunctions $c_1^{2n}(u)$ with Koopman eigenvalues $8n$, and Koopman modes $\hat{u}_{2n}(x) = 8n(-1/2)^n e^{-2nx}$.

Equation eq. (B.32) matches that found in section B.3.1 using the inverse Laplace transform eq. (B.22). To find the second Koopman expansion, valid downstream of the soliton, we would begin with the ansatz,

$$K(u;x,z) = \sum_{n=1}^{\infty} \hat{K}_n(x,z)c_1^{-n}(u), \tag{B.33}$$

i.e. an expansion in exponentially decaying Koopman eigenfunctions.

In summary, we have used the inverse scattering transform approach to identify Koopman eigenfunctions and eigenvalues of the KdV equation and shown how different sets of eigenfunctions are required in different regions of space-time to express localised nonlinear wave evolution in the form of a Koopman decomposition. We now extend this approach to examine more complex dynamics involving soliton interactions, where the number of possible Koopman decompositions increases dramatically. Selecting the appropriate decomposition for a given region of the $x-t$ plane depends on the relative positions of all solitons.

B.3.5 Multiple solitons

The method presented in section B.3.4 can be generalised to an arbitrary but finite number of solitons, so long as the initial condition has no continuous spectrum in the scattering problem. To demonstrate the approach, we examine in detail the interaction of two solitons.

With two solitons, we now have two non-zero scattering eigenvalues κ_1 and κ_2, with corresponding Koopman eigenfunctions $c_{\kappa_1}(u)$ and $c_{\kappa_2}(u)$ and Koopman eigenvalues $4\kappa_1^3$ and $4\kappa_2^3$. The eigenfunctions $c_{\kappa_1}(u)$ and $c_{\kappa_1}(u)$ can be raised to arbitrary powers to produce further Koopman eigenfunctions, but we can now also multiply them (Mezić, 2013). As was found in the one-soliton case, only even powers are required, since c_κ^2 rather than c_κ appears in the Marchenko equation. The possible combinations of $c_{\kappa_1}(u)$ and $c_{\kappa_2}(u)$ thus yield a set of Koopman eigenfunctions of the form

$$c_{\kappa_1}^{2j}(u)c_{\kappa_1}^{2k}(u), \qquad (j,k) \in \mathbb{Z}^2,$$

with corresponding Koopman eigenvalues $4\kappa_1^3 \cdot 2j + 4\kappa_2^3 \cdot 2k = 8(\kappa_1^3 j + \kappa_2^3 k)$. If κ_1 and κ_2 are both rational numbers then the Koopman eigenvalues will be degenerate, an effect that has also been observed in Koopman decompositions of the Burgers equation (Page and Kerswell, 2018).

With two scattering eigenvalues, the Marchenko equation eq. (B.26) becomes

$$\begin{aligned} K(x,z,t) + c_{\kappa_1}^2 \exp\left(8\kappa_1^3 t - \kappa_1(x+z)\right) + c_{\kappa_2}^2 \exp\left(8\kappa_2^3 t - \kappa_2(x+z)\right) \\ + \int_x^\infty K(x,y,t) c_{\kappa_1}^2 \exp\left(8\kappa_1^3 t - \kappa_1(y+z)\right) \mathrm{d}y \\ + \int_x^\infty K(x,y,t) c_{\kappa_2}^2 \exp\left(8\kappa_2^3 t - \kappa_2(y+z)\right) \mathrm{d}y = 0. \end{aligned} \tag{B.34}$$

The z-dependence of the terms in eq. (B.34) implies $K(x,z,t)$ is of the form

$$K(x,z,t) = L^{(1)}(x,t)e^{-\kappa_1 z} + L^{(2)}(x,t)e^{-\kappa_2 z}, \tag{B.35}$$

which reduces eq. (B.34) to a pair of coupled equations:

$$\begin{aligned} L^{(1)}(x,t) + c_{\kappa_1}^2 e^{8\kappa_1^3 t - \kappa_1 x} + \frac{1}{2\kappa_1} L^{(1)}(x,t) c_{\kappa_1}^2 e^{8\kappa_1^3 t - 2\kappa_1 x} & \\ + \frac{1}{\kappa_1 + \kappa_2} L^{(2)}(x,t) c_{\kappa_1}^2 e^{8\kappa_1^3 t - (\kappa_1+\kappa_2)x} = 0, & \end{aligned} \tag{B.36}$$

$$\begin{aligned} L^{(2)}(x,t) + c_{\kappa_2}^2 e^{8\kappa_2^3 t - \kappa_2 x} + \frac{1}{\kappa_1 + \kappa_2} L^{(1)}(x,t) c_{\kappa_1}^2 e^{8\kappa_1^3 t - (\kappa_1+\kappa_2)x} & \\ + \frac{1}{2\kappa_2} L^{(2)}(x,t) c_{\kappa_1}^2 e^{8\kappa_1^3 t - 2\kappa_2 x} = 0. & \end{aligned} \tag{B.37}$$

We propose Koopman decompositions for the observables $L^{(1)}$ and $L^{(2)}$ of the form

$$L^{(1,2)}(u;x) = \sum_j \sum_k \hat{L}_{j,k}^{(1,2)}(x,z) c_{\kappa_1}^{2j}(u_0) c_{\kappa_1}^{2k}(u_0) e^{8(\kappa_1^3 j + \kappa_2^3 k)t}. \tag{B.38}$$

As found in the single soliton case, the range of values over which we sum j and k, or equivalently whether the expansion is constructed using exponentially growing or decaying modes (or a combination), implicitly selects a region of space-time in which the expansion converges.

Substituting eq. (B.38) into eq. (B.36) and comparing coefficients of exponentials (assuming no degeneracy) yields the recurrence relations

$$\begin{aligned} \hat{L}_{j,k}^{(1)} + \frac{1}{2\kappa_1} \hat{L}_{j-1,k}^{(1)} e^{-2\kappa_1 x} + \frac{1}{\kappa_1 + \kappa_2} \hat{L}_{j-1,k}^{(2)} e^{-(\kappa_1+\kappa_2)x} & \\ = \begin{cases} -e^{-\kappa_1 x}, & j = 1, k = 0, \\ 0, & \text{otherwise}, \end{cases} & \end{aligned} \tag{B.39}$$

$$\begin{aligned} \hat{L}_{j,k}^{(2)} + \frac{1}{\kappa_1 + \kappa_2} \hat{L}_{j,k-1}^{(1)} e^{-(\kappa_1+\kappa_2)x} + \frac{1}{2\kappa_2} \hat{L}_{j-1,k}^{(2)} e^{-2\kappa_2 x} & \\ = \begin{cases} -e^{-\kappa_2 x}, & j = 0, k = 1, \\ 0, & \text{otherwise}. \end{cases} & \end{aligned} \tag{B.40}$$

With some rearrangement, these can be solved straightforwardly for j and k either increasing or decreasing, and various boundary conditions are therefore possible. The solutions are too complicated to include here, but can be found using a computer algebra system. As described previously in the one soliton calculation, the Koopman decomposition for the pair of observables $L^{(1,2)}(u;x)$ can be converted into a Koopman decompositions for $K(u;x,z)$ via equation eq. (B.35), before the decomposition for the velocity is obtained from $u(x,t) = -2\left(\partial_x K(x,z,t)|_{z=x} + \partial_z K(x,z,t)|_{z=x}\right)$ (Drazin and Johnson, 1989).

The various possible boundary conditions, which we now discuss in more detail, are based on the interpretation of an isolated soliton as a homoclinic orbit. The two-soliton decompositions are somewhat analogous to what one would expect for trajectories shadowing two orthogonal homoclinic orbits connected to the origin, each with a crossover point. In that scenario we anticipate three decompositions: one using (products of) the attracting eigenfunctions of both orbits (downstream of both solitons); one using the eigenfunctions associated with the repelling halves of each homoclinic orbit (upstream of both solitons); one using the eigenfunctions of the attracting half of one orbit and the repelling half of the other (between the solitons). This analogy is not quite complete as the origin is not a fixed point – there is no frame in which the dynamics are steady. Furthermore, the expansion between the solitons will change when the faster structure overtakes the slower, yielding a fourth Koopman decomposition. However, we will see that these intuitive arguments do result in a set of four Koopman decompositions that together describe the entire spatio-temporal dynamics.

First, we seek an expansion valid downstream of both solitons by assuming that $\hat{L}^{(1)}_{j,k}$ and $\hat{L}^{(2)}_{j,k}$ are zero for $j < 0$ and $k < 0$, or equivalently seek to build a solution using only temporally growing modes. The velocity field resulting from this solution for $L^{(1,2)}$ is reported in fig. B.2 (the red curves) for a particular choice of κ_1 and κ_2 which is discussed further below.

On the other hand, if both $\hat{L}^{(1)}_{j,k}$ and $\hat{L}^{(2)}_{j,k}$ are assumed to be zero for $j > 0$ and $k > 0$, an expansion is obtained which converges upstream of both solitons and involves only temporally decaying modes. This decomposition is also show in fig. B.2 (blue curves). Note that, for both the temporally decaying and growing expansions, the inclusion of products of the Koopman eigenfunctions allows the ‘linear’ Koopman decompositions to represent the dynamics upstream and downstream of the solitons during their interaction. As shown in fig. B.2, these expansions apply both before and after the faster soliton overtakes the slower.

The more interesting case is the expansion between the solitons. One possibility is to assume $\hat{L}^{(1)}_{j,k} = 0$ and $\hat{L}^{(2)}_{j,k} = 0$ for $j < 0$ but $k > 0$. This amounts to a decomposition involving growing modes associated with the κ_1 eigenvalue (i.e. those that describe the evolution upstream of soliton 1) but decaying modes associated with the κ_2 eigenvalue (describing the evolution downstream of soliton 2). An example of this expansion, which describes the evolution between the solitons up to (and including part of) their interaction, is shown in fig. B.2 (green curves). The products in the Koopman expansion of the form $c^{j}_{\kappa_1}(u)c^{k}_{\kappa_2}(u)$

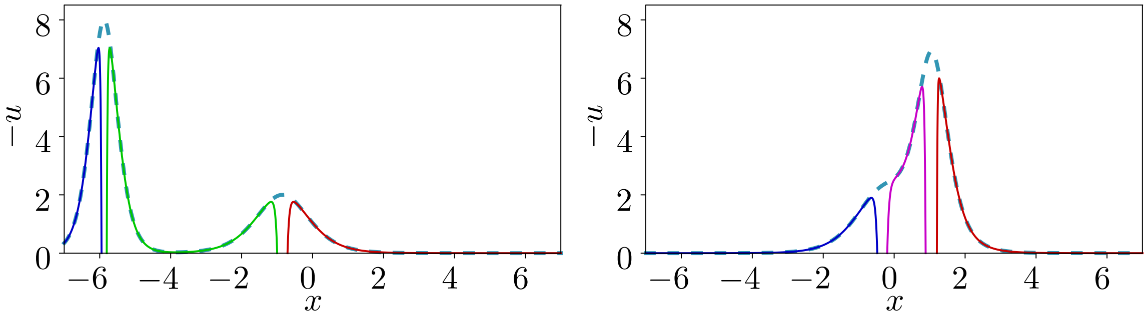

(a) $t = -0.35$ (c) $t = 0.05$

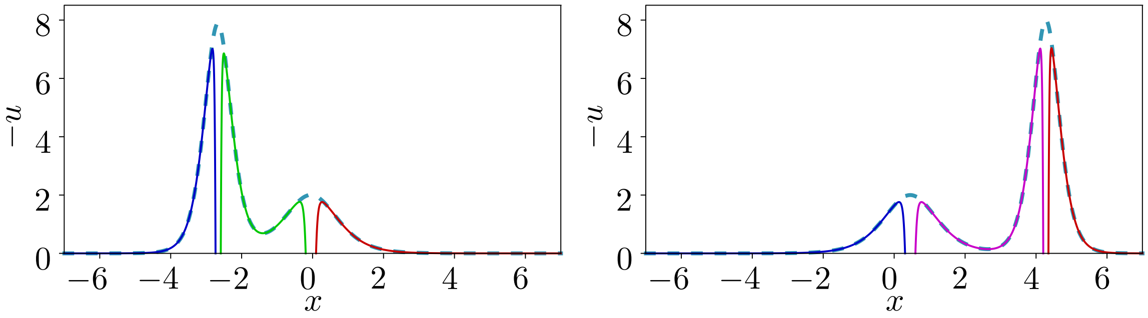

(b) $t = -0.15$ (d) $t = 0.25$

Fig. B.2 Truncated Koopman decompositions with 10 modes for the 2-soliton solution eq. (B.42) (shown as dashed line), at different times. For $t < 0$, the decomposition with Koopman eigenfunctions $c_1^j c_2^k$ with $j \leq 0$ and $k \geq 0$ (in green) must be used between the solitons, whereas $k \geq 0$ and $j \leq 0$ (in pink) does not converge, and is completely off the scale of the plot. The reverse is true for $t > 0$. The $j \leq 0$, $k \leq 0$ expansion (blue) and $j \geq 0$, $k \geq 0$ (red) are needed at all times, upstream and downstream, respectively, of both solitons.

allow for a 'linear' representation of the strongly nonlinear dynamics between the solitons as they interact.

However, as the faster soliton approaches the slower, the region of space in which this decomposition holds shrinks and eventually vanishes. For a Koopman decomposition which holds between the solitons post-interaction, it is necessary to instead assume $\hat{L}^{(1)}_{j,k} = 0$ and $\hat{L}^{(2)}_{j,k} = 0$ for $j > 0$ and $k < 0$, i.e. an ansatz using the unstable eigenvalues for the κ_2 soliton and the stable eigenvalues associated with the κ_1 soliton. This expansion is shown in pink in fig. B.2.

The particular two soliton interaction reported in fig. B.2 is the 'classical' two soliton solution (see e.g. Drazin and Johnson, 1989) defined by the initial condition,

$$u(x,0) = -6\,\mathrm{sech}^2 x, \tag{B.41}$$

for which the KdV equation has the known analytical solution,

$$u(x,t) = -12\frac{3+4\cosh(2x-8t)+\cosh(4x-64t)}{(3\cosh(x-28t)+\cosh(3x-36t))^2}. \tag{B.42}$$

This solution is particularly useful when assessing the crossover between the multiple Koopman decompositions owing to the fact that the initial condition eq. (B.41) corresponds to the temporal "midpoint" in the interaction between the two solitons which separate as $t \to \pm\infty$. In fact, precisely when $t = 0$, neither of the interior decompositions (the green and pink curves in fig. B.2) are valid, and they are nowhere pointwise convergent to a finite value (not shown). When t is very small, a very large number of terms is required for the expansions to well approximate the true solution near the solitons.

Another consequence of using the solution defined by eq. (B.42) is the occurrence of degeneracy in the Koopman eigenvalues. The scattering problem for this potential gives discrete eigenvalues of $\kappa_1 = 1$ and $\kappa_2 = 2$. These values correspond to Koopman eigenvalues $4\kappa_1^3 = 4$ and $4\kappa_2^3 = 32$ and normalisation coefficients (Koopman eigenfunctions) $c_1(u_0) = \sqrt{6}$ and $c_2(u_0) = 2\sqrt{3}$ respectively (Drazin and Johnson, 1989). The fact that the two Koopman eigenvalues are both proportional to perfect cubes, coupled with allowance for both exponentially decaying and growing modes, causes the degeneracy. For example, the combinations $(j,k) = (0,2)$ (eigenfunction $c_2^4(u)$) and $(j,k) = (8,1)$ (eigenfunction $c_1^{16}(u)c_2^2(u)$) both share the eigenvalue 128. In the degenerate case, the recurrence relations presented above eqs. (B.39) and (B.40) are now only one possible solution to the Marchenko equation. However, considering the nondegenerate situation with $\kappa_1 = 1$ and $\kappa_2 = 2+\varepsilon$ as $\varepsilon \to 0$, which does not become invalid, implies that our solution is the correct one.

To summarise, we have demonstrated that four Koopman decompositions are required to describe the interaction of a pair of solitons in the KdV equation. Each expansion is convergent in a particular region of space-time, either: (i) upstream of both solitons, (ii) downstream of both solitons, (iii) between the solitons with the slower wave upstream of the faster or (iv) between the solitons with the faster wave upstream of the slower. There is a simple logic to selecting the eigenfunctions required for any given expansion: Alone, any individual soliton has a pair of Koopman decompostions; an expansion describing the solution upstream of the soliton requires exponentially growing eigenfunctions while temporally decaying eigenfunctions are needed downstream. In the two-soliton interaction, this continues to apply. However, products of the two sets of eigenfunctions must also be included to account for interaction between the solitons.

The approach outlined above naturally extends to arbitrary numbers of solitons, where construction of a Koopman decomposition at any point in space requires products of all the growing eigenfunctions for any solitons downstream of that point and all of the decaying eigenfunctions from the upstream solitons. For N solitons, this would involve the solution of N recurrence relations similar to eqs. (B.39) and (B.40) simultaneously. The existence of multiple Koopman decompositions which partition the spatiotemporal domain to describe the full solution to a nonlinear PDE has important consequences for DMD, which we now examine.

B.4 Dynamic mode decomposition

Dynamic mode decomposition (DMD) can be an effective way to extract Koopman eigenvalues, modes and eigenfunctions from numerical data. A rigorous connection between Koopman decompositions and DMD has been established under certain conditions (Williams et al., 2015; Rowley and Dawson, 2017). The key requirements are (i) that the Koopman eigenfunctions can be expressed as a linear combination of the elements of the DMD observable vector, $\{g_i(u)\}$, and (ii) that sufficient data is available.

A variety of methods have been proposed to augment DMD and aid its ability to extract Koopman eigenfunctions from data. For example, in 'extended' DMD, the observable vector g is built from a dictionary of functionals of the state. For the nonlinear PDEs considered in this paper, we will see that standard DMD (where the observable is simply the state variable itself, $g_i = u(x = x_i)$), is sufficient to perform numerical Koopman decompositions, provided that the observations are restricted to a particular region of space-time where a single Koopman decomposition holds.

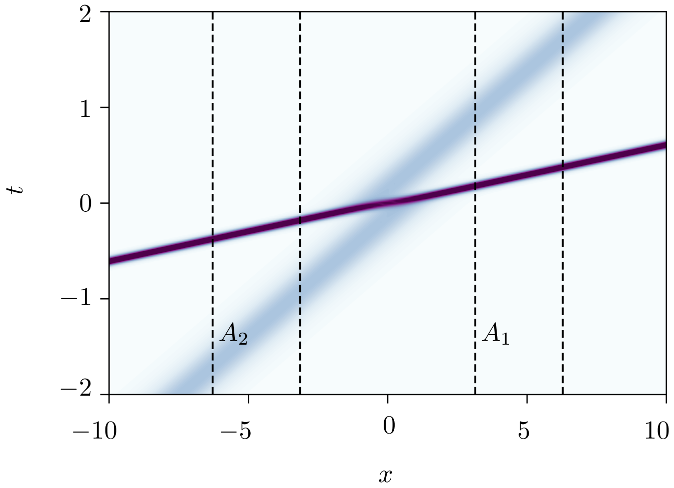

Fig. B.3 Two soliton solution to the KdV equation eq. (B.41) visualized with contours of $-u$. Dashed lines identify DMD observation windows $A_1 = (\pi, 2\pi)$ and $A_2 = (-2\pi, -\pi)$.

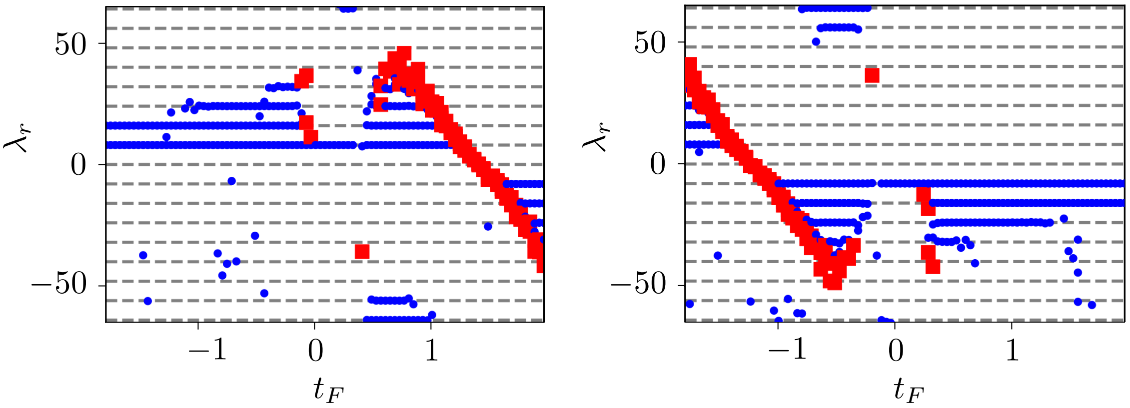

Fig. B.4 Real part of eigenvalues obtained in DMD calculations with a windowed observable $g(u) = \mathbf{u}(x \in A_i)$ against the end time, t_F, of each DMD computation. Each DMD calculation is performed within a time window of length $T_w = 0.4$ with snapshots available at a resolution of $\delta t = 0.005$. The DMD timestep separating snapshots is $\delta t_{DMD} = 0.01$ and $M = 50$ snapshot pairs are used. Left: observation window A_1. Right: observation window A_2. Note that blue circles identify purely real eigenvalues, red squares are complex conjugate pairs.

As a first example, consider the two-soliton KdV dynamics in fig. B.3. The parameters match those considered in §3. Two groups of DMD calculations are considered with a windowed observable

$$g(u) = \mathbf{u}(x \in A_j), \tag{B.43}$$

where the elements of $\mathbf{u}$ are observations of the state u at the grid points, $(\mathbf{u})_i := u(x = x_i)$, and the choices for the window A_j are identified in fig. B.3. The DMD methodology is as described in (Tu et al., 2014).

For each of the two observation windows A_j, we perform many DMD calculations over short time intervals $T_w = 0.2$. The real parts of the eigenvalues obtained in these calculations are reported in fig. B.4, as a function of the final time of each individual DMD computation. For the window A_1, while $t_F \lesssim 0$, the DMD identifies eigenvalues $\lambda_n = 8n,\ n \in \mathbb{N}$. This corresponds to the analytical prediction for the Koopman decomposition upstream of both solitons, where the set of Koopman eigenvalues required to correctly describe the time evolution is the product of the unstable eigenvalues associated with each individual soliton.

Near $t_F = 0$, complex-conjugate pairs of eigenvalues (shown in red in fig. B.4) emerge and DMD is unable to find a robust representation that remains consistent between subsequent calculations. This behaviour coincides with the observation window viewing regions of the solution which are expressed in terms of multiple Koopman decompositions; namely the top of the faster soliton is included in the observation window. In this case, DMD is unable to build a consistent linear representation for the dynamics.

When $0.5 \lesssim t_F \lesssim 1$, the observation windows occupy a region of space-time between the two solitons, and the DMD algorithm is able to correctly identify the exponentially growing and decaying eigenvalues required in one of the central Koopman decompositions. As well as the exponentially growing terms associated with being upstream of the slower soliton, $\lambda_n = 8n,\ n \in \mathbb{N}$, the rapidly decaying eigenvalue $\lambda_n = -64$ is also obtained. This is the slowest-decaying eigenvalue associated with being downstream of the faster soliton. Note that the other visible decaying eigenvalue ($\lambda_n = -56$) in this region is associated with the product of the first unstable Koopman eigenfunction associated with the slower soliton and the first stable Koopman eigenfunction connected with the faster wave, $\varphi_8(u)\varphi_{-64}(u)$ (see §3). Other decaying eigenvalues $\lambda_n = -8n\ n \in \mathbb{N}$ are also anticipated based on interactions $\varphi_8^j \varphi_{-64}^k$, though these terms are all much smaller in amplitude and are not picked up by the DMD. These results are quickly contaminated with pairs of complex-conjugate modes that are associated with the appearance of the second crossover point – the top of the slower soliton – in the observation window. Finally, towards the end of the later-time DMD calculations for window A_1, DMD starts to recover the purely decaying Koopman eigenvalues associated with the expansion downstream of both solitons.

Similar behaviour is observed for observation window A_2, which also shows evidence of three expansions. In this instance, the eigenvalues identified between the solitons are similar to those seen for window A_1, but appear to be flipped about $\lambda_r = 0$ as the observation window is upstream of the faster solution and downstream of the slower wave. Therefore, while the upstream-of-both and downstream-of-both results are unchanged, the Koopman decomposition between the the two solitons involves the product of the unstable eigenvalues associated with the faster soliton and the stable eigenvalues of the slower pulse, i.e. the opposite of window A_1.

These observations suggest that the use of a spatially-restricted observable is a sensible choice in nonlinear problems involving spatially-localised dynamics. This observable choice will allow individual Koopman eigenvalues and modes to be extracted by avoiding the inclusion of crossover points between multiple decompositions, for which DMD is unable to build a consistent linear operator. In order to demonstrate the utility of such an approach, we examine a solution of the sine-Gordon equation,

$$\partial_t^2 u = \partial_x^2 u - \sin u, \tag{B.44}$$

which arises in a variety of physical situations, including the propagation of dislocations through a crystal and as a unitary theory for elementary particles (Scott et al., 1973). Though analytical solution of the sine-Gordon equation is possible via the inverse scattering method (Ablowitz et al., 1973), we do not attempt to analytically find Koopman decompositions. Instead, we will use the rules of thumb developed above for KdV to use DMD to identify Koopman eigenvalues.

As an example, we focus on the moving breather solution (Drazin and Johnson, 1989),

$$u_b(x,t) = 4\arctan\left[\frac{\sqrt{1-l^2}}{l}\frac{\sin(\gamma l(t - Vx))}{\cosh(\gamma\sqrt{1-l^2}(x - Vt))}\right], \tag{B.45}$$

where $\gamma := 1/\sqrt{1-l^2}$. This solution is shown in fig. B.5 for $l = V = 1/2$, and is a localised relative periodic orbit.

Based on our analysis of both the Burgers and KdV equations, we anticipate the existence of a pair of Koopman decompositions upstream/downstream of the breather in terms of exponentially decaying/growing eigenvalues respectively. In order to extract these representations, we conduct a pair of DMD computations with our observations restricted to windows upstream or downstream of the breather (marked in fig. B.5).

The output of these calculations is reported in fig. B.6. As anticipated, the calculations produce robust results both upstream and downstream of the oscillating pulse in terms of

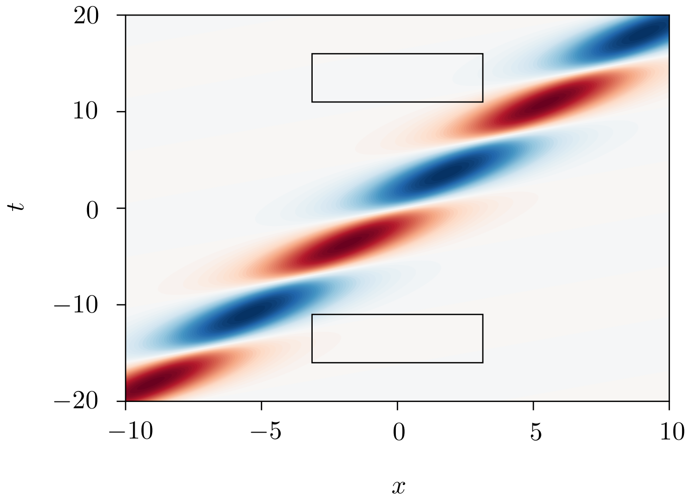

Fig. B.5 Moving breather solution to the sine-Gordon equation eq. (B.45). Contours of u, with the observation windows for the DMD calculations in fig. B.6 identified by black boxes.

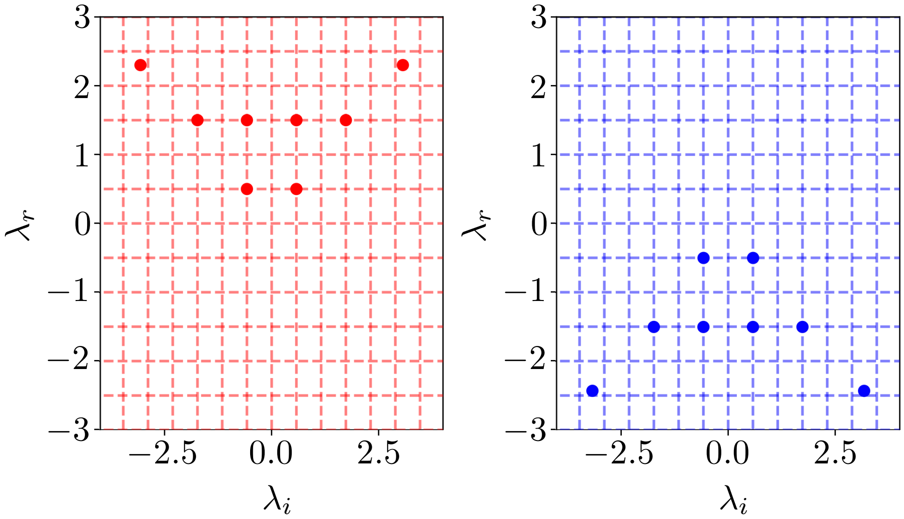

Fig. B.6 DMD applied to the sine-Gordon upstream (left) and downstream (right) of the breather (see fig. B.5). In each calculation the observable is the state vector for $x \in (-\pi, \pi)$ and the time window length $T_w = 5$. $M = 400$ snapshot pairs are used with $\delta t = 0.1$.

(temporal) exponential growth and decay. Note that, unlike the Burgers and KdV equations, the eigenvalues are complex. The upstream and downstream spectra are related via a reflection through $\lambda_r = 0$.

In the one soliton solution of KdV, we demonstrated in a reduced dynamical system that the soliton may be regarded as a homoclinic connection from the zero state to itself, with a crossover point in the middle. We can interpret the results of the calculation on the sine-Gordon dynamics similarly: in a co-moving coordinate, the moving breather may be interpreted as a homoclinic orbit about the trivial solution $u = 0$, and the DMD calculations identify the Koopman decompositions associated with the 'repelling' and 'attracting' halves of this trajectory.

B.4.1 Periodic computational domains

All of the problems studied so far in this work have been classical analytical solutions of integrable nonlinear PDEs on infinite domains. However, studies of localised solutions to more complex systems (e.g. the Navier-Stokes equations (Schneider et al., 2010)) are conducted in large periodic computational domains. As pointed out by Sharma et al. (2016), Koopman decompositions for exact coherent structures in spatially-periodic problems naturally take the form of travelling waves and the (temporal) Koopman eigenvalues should all be purely imaginary. This should be contrasted with the Koopman decompositions presented in this paper, which have all involved Koopman eigenvalues with non-zero real part.

To examine the connection between the assertions of Sharma et al. (2016) and the analytical Koopman decompositions derived in this paper, we consider again the one-soliton solution to the KdV equation (see section B.3.1 and section B.3.4). Here, we supply the soliton $u = -2\mathrm{sech}^2 x$ as an initial condition in a numerical simulation where the KdV equation is solved numerically on a periodic domain of length 8π. A Fourier transform is applied in x; the nonlinear terms are evaluated in physical space before the transform is applied. For time advancement, explicit Adams-Bashforth is used for the nonlinear terms and implicit Crank-Nicolson is used for the dispersive term. The domain is long enough such that the error between the periodic numerical simulation and the true one-soliton solution, $\|u_{per} - u_{sol}\|_2 / \|u_{sol}\|_2$, is about 4×10^{-4} after $\gtrsim 3$ flow-through times.

In fig. B.7 we report the results of two sets of DMD calculations on this one soliton KdV evolution. In the first, a single computation, we perform standard DMD on the full state vector (i.e. over the entire spatial domain) for a time window spanning many flow-through times. As anticipated, the DMD eigenvalues are all purely imaginary and are multiples of a fundamental harmonic $\omega = 1$ (on this domain the flow-through time of the isolated soliton is $T = 2\pi$). The DMD modes (not shown) are Fourier modes.

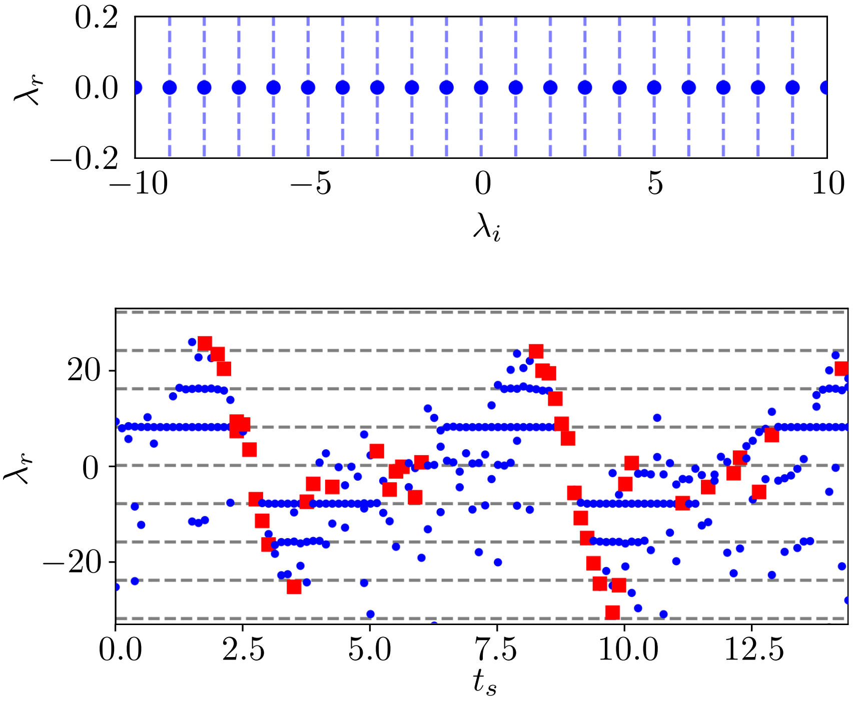

Fig. B.7 Two alternative DMD computations for the ‘one soliton’ solution of the KdV equation evolving in a periodic computational domain of length $L = 8\pi$. Top: full (unwindowed) state observable, $g = \mathbf{u}$, observed over a time window $T_w = 15$ with $M = 400$ snapshot pairs. Vertical dashed lines identify multiples of the first non-zero frequency ($\omega = 1$). Bottom: windowed state observable, $g = \mathbf{u}(x \in A)$, where $A = (7\pi/2, 4\pi)$. Multiple DMD computations are performed with time window length $T_w = 0.2$ and the real part of the DMD eigenvalues are plotted against the start time of their respective DMD calculation. $M = 40$ snapshot pairs are used. Throughout, $\delta t = 0.0125$.

In the second set of calculations, we adopt the approach we have advocated for the infinite domains. We perform DMD on a windowed observable $g(u) = \mathbf{u}(x \in A)$, where $A = (7\pi/2, 4\pi)$, conducting a sequence of DMD calculations on short time windows $T_w = 0.2$. The real part of the eigenvalues obtained in each calculation are shown in the lower panel of fig. B.7. As the soliton repeatedly passes through the domain, the DMD calculations continually pick up the upstream/downstream eigenvalues associated with the solution on an unbounded domain (i.e. one of $\lambda_n = \pm 8n$, $n \in \mathbb{N}$).

In this problem the “correct” decomposition is the one involving purely imaginary eigenvalues, regardless of domain length (as long as it remains finite). This can be demonstrated explicitly by considering the periodic ‘cnoidal’ solutions of the KdV equation (Korteweg and de Vries, 1895),

$$u(x,t) = A - Bm\,\mathrm{cn}^2\left(C(x-ct)\right), \tag{B.46}$$

where cn is the Jacobi elliptic cosine function with modulus $m \in [0,1]$, and we require $\frac{B}{2C^2} = 1$ and $c = -2(3A - 2Bm + 2C^2)$ to be a solution to KdV (Drazin and Johnson, 1989). Equation eq. (B.46) is a right-moving travelling wave with phase speed c, and is spatially periodic with period $2K/C$, where $K = K(m)$ is the complete elliptic integral of the first kind (Abramowitz and Stegun, 1965). Concentrating on the special case $A = -\frac{2}{3}\left(1 + (1-2m)p\right)$, $B = 2p$ and $C = \sqrt{p}$, where $p := 1/\sqrt{1-m+m^2}$, in the limit as $m \to 0$, eq. (B.46) becomes the small-amplitude solution to the linearised KdV, a pure cosine. As $m \to 1$ however, the peaks become repeated copies of the one-soliton solution, very widely separated in x: on any finite spatial interval at fixed t, eq. (B.46)→eq. (B.17) as $m \to 1$.

The Fourier series for eq. (B.46) can be calculated using the series for dn^2 given by Oberhettinger (1973) and the identity $\mathrm{dn}^2(x) = 1 - m + m\,\mathrm{cn}^2(x)$, giving

$$u(x,t) = A - B\left(\frac{E}{K} + m - 1\right) - \frac{2B\pi^2}{K^2}\sum_{n=1}^{\infty}\frac{nq^n}{1-q^{2n}}\cos\left(\frac{n\pi C}{K}\{x-ct\}\right), \tag{B.47}$$

where E is the complete elliptic integral of the second kind, and $q(m) = e^{-\pi K(1-m)/K(m)}$ is the ‘nome’ (Abramowitz and Stegun, 1965).

Viewing eq. (B.47) as a Koopman mode decomposition by writing the cosine in terms of exponentials, we identify Koopman eigenvalues $in\pi cC/K$ for $n \in \mathbb{Z}$. These are purely imaginary (or zero), as anticipated from periodicity, and should be contrasted to the purely real Koopman eigenvalues found for the single soliton in isolation eq. (B.17).

Despite the correspondence between the one-soliton solution to KdV and the limiting form of the periodic cnoidal wave, the isolated soliton Koopman decomposition is not obtained in the large-domain limit due to the fact that an *infinite* domain is required to obtain the scattering data that define the Koopman eigenfunctions. Furthermore, in contrast to Koopman decompositions constructed in section B.3 for solitons on infinite domains, the Koopman modes and eigenvalues obtained in this periodic example are dependent on the domain length rather than being purely tied to the soliton itself. There are additional numerical issues too – the periodic Koopman decomposition can be difficult to obtain in the large-domain limit since very many Fourier modes are required to resolve the evolution (see Appendix).

The striking difference between the periodic Koopman decomposition and the decomposition for a truly localised structure is somewhat disconcerting, since simulations of localised structures are often conducted on large periodic domains under the assumption that the true isolated structure is well approximated. However, the windowed DMD results reported in fig. B.7 indicate that the Koopman decompositions for the localised structure can still be obtained in periodic computations by using a spatially localised observable. The reason for this is clear if we return to the simplified system describing travelling wave solutions to KdV, eq. (B.24). There is a continuous family of periodic orbits around the centre – the cnoidal waves – contained within a homoclinic orbit from the saddle, which corresponds to the one-soliton solution. The periodic configuration described here corresponds to one of these periodic orbits. As $m \to 0$, the orbits are close to the centre, and as $m \to 1$, the orbits approximate the homoclinic orbit, but with finite period. DMD on the short time windows identifies the eigenvalues of the nearby homoclinic orbit, instead of the much longer periodic orbit it is actually computed on.

These results suggest that the two alternative strategies for DMD are both equally valid, depending on what the computation is designed to find: (i) the ‘standard’ approach using the full state vector which will identify purely imaginary, domain-dependent Koopman eigenvalues (if the structure is allowed to pass through the entire domain) and (ii) the windowed observable which can identify the growing/decaying Koopman eigenvalues associated with upstream/downstream expansions for a truly localised structure.

B.5 Conclusions

In this paper, we have derived Koopman decompositions in a number of problems involving the propagation and interaction of isolated structures, namely a front in the Burgers equation and solitons in the KdV equation. The results indicate that isolated nonlinear waves require two Koopman decompositions to describe their evolution, which converge either upstream of downstream of the structure. In many-soliton interactions, multiple Koopman decompositions are required, and selecting the convergent expansion at any point requires knowledge of the relative positions of all solitons (i.e. whether they are upstream or downstream of the observation point).

We proposed a simple modification to the standard DMD methodology that allows allows the algorithm to identify the individual Koopman decompositions around the isolated structures. This approach was used to identify the various Koopman decompositions in a two-soliton interaction solution of KdV, before we applied it to the sine-Gordon equation where the analytical eigenvalues are at present unknown. The results suggest that the need for multiple Koopman decompositions to cover the full spatio-temporal domain may be a generic feature of nonlinear PDEs.

Further work is required to assess the extent to which these results extend to more complex systems, such as the full Navier-Stokes equations. As a starting point, the windowing approach could be applied to some of the known localised relative periodic solutions in pipe flow (Avila et al., 2013). In addition, our analysis of the KdV equation was restricted to pure soliton evolution – i.e. dispersive effects were absent. The inclusion of dispersion will introduce a continuous spectrum of purely imaginary Koopman eigenvalues. It would be of interest to know how the presence of these effects impacts the capability of DMD to identify the eigenvalues associated with the coherent structures, and whether some of the recent proposed modifications to the algorithm, such as augmenting the observable with other functionals, can help.

B.6 Appendix: Further details on the cnoidal wave

In this appendix we briefly discuss the behaviour of the Koopman decomposition for the cnoidal wave eq. (B.47) in the large-domain limit.

In the limit $m \to 1$, the elliptic integral $K(1-m) \to \pi/2$, so $q \sim e^{-\pi^2/2K}$ and

$$K \sim -\frac{\pi^2}{2\log q}. \tag{B.48}$$

Therefore the nth Fourier coefficient from eq. (B.47) obeys

$$-\frac{2B\pi^2}{K^2}\frac{nq^n}{1-q^{2n}} \sim -\frac{8B(\log q)^2}{\pi^2}\frac{nq^n}{1-q^{2n}}. \tag{B.49}$$

Since $q \to 1$ as $m \to 1$, we expand with $\varepsilon = 1-q$ to give

$$-\frac{2B\pi^2}{K^2}\frac{nq^n}{1-q^{2n}} \sim -\frac{8B(-\varepsilon)^2}{\pi^2}\frac{n}{2n\varepsilon} \to 0. \tag{B.50}$$

Since every Fourier coefficient approaches 0 as $m \to 1$, but the cnoidal wave peaks tend to a fixed height of -2, an increasing number of Fourier modes (which are Koopman modes here) must be used to approximate the solution. This means that for very isolated solitons in a periodic domain, a large number of DMD modes will be required.

B.7 References

Ablowitz, M. J., Kaup, D. J., Newell, A. C., and Segur, H. (1973). Method for solving the sine-Gordon equation. *Phys. Rev. Lett.*, 30(25):1262.

Ablowitz, M. J., Kaup, D. J., Newell, A. C., and Segur, H. (1974). The inverse scattering transform-Fourier analysis for nonlinear problems. *Stud. Appl. Math.*, 53(4):249–315.

Abramowitz, M. and Stegun, I. A. (1965). *Handbook of mathematical functions: with formulas, graphs, and mathematical tables*, volume 55. Courier Corporation.

Arbabi, H. and Mezić, I. (2017). Study of dynamics in post-transient flows using Koopman mode decomposition. *Phys. Rev. Fluids*, 2:124402.

Avila, M., Mellibovsky, F., Roland, N., and Hof, B. (2013). Streamwise-localized solutions at the onset of turbulence in pipe flow. *Phys. Rev. Lett*, 110(22):224502.

Bagheri, S. (2013). Koopman-mode decomposition of the cylinder wake. *J. Fluid Mech.*, 726:596–623.

Benton, E. R. and Platzman, G. W. (1972). A table of solutions of the one-dimensional Burgers equation. *Quart. Appl. Math.*, 30:195–212.

Brunton, B. W., Johnson, L. A., Ojemann, J. G., and Kutz, J. N. (2016a). Extracting spatial–temporal coherent patterns in large-scale neural recordings using dynamic mode decomposition. *J. Neurosci. Methods*, 258:1–15.

Brunton, S. L., Brunton, B. W., Proctor, J. L., Kaiser, E., and Kutz, J. N. (2017). Chaos as an intermittently forced linear system. *Nat. Commun.*, 8(1):19.

Brunton, S. L., Brunton, B. W., Proctor, J. L., and Kutz, J. N. (2016b). Koopman invariant subspaces and finite linear repesentations of nonlinear dynamical systems for control. *PLOS ONE*, 11(2).

Drazin, P. G. and Johnson, R. S. (1989). *Solitons: an introduction*. Cambridge University Press, 1 edition.

Gardner, C. S., Greene, J. M., Kruskal, M. D., and Miura, R. M. (1967). Method for solving the Korteweg-deVries equation. *Phys. Rev. Lett.*, 19(19):1095.

Jovanović, M. R., Schmid, P. J., and Nichols, J. W. (2014). Sparsity-promoting dynamic mode decomposition. *Phys. Fluids*, 26:024103.

Koopman, B. O. (1931). Hamiltonian Systems and Transformations in Hilbert Space. *Proc. Nat. Acad. Sci.*, 17(5):315–318.

Korteweg, D. D. J. and de Vries, D. G. (1895). Xli. on the change of form of long waves advancing in a rectangular canal, and on a new type of long stationary waves. *The London, Edinburgh, and Dublin Philosophical Magazine and Journal of Science*, 39(240):422–443.

Kutz, J. N., Brunton, S. L., Brunton, B. W., and Proctor, J. L. (2016). *Dynamic Mode Decomposition: Data-Driven Modeling of Complex Systems*. SIAM, 1 edition.

Kutz, J. N., Proctor, J., and Brunton, S. (2018). Applied Koopman theory for partial differential equations and data-driven modeling of spatio-temporal systems. *Complexity*, 2018.

Mezić, I. (2005). Spectral properties of dynamical systems, model reduction and decompositions. *Nonlinear Dynam.*, 41:309–325.

Mezić, I. (2013). Analysis of fluid flows via spectral properties of the Koopman operator. *Ann. Rev. Fluid Mech.*, 45:357–378.

Mezic, I. (2017). Koopman operator spectrum and data analysis.

Nakao, H. and Mezić, I. (2020). Spectral analysis of the Koopman operator for partial differential equations.

Oberhettinger, F. (1973). *Fourier expansions: a collection of formulas*. Academic Press.

Page, J. and Kerswell, R. R. (2018). Koopman analysis of Burgers equation. *Phys. Rev. Fluids*, 3:071901.

Page, J. and Kerswell, R. R. (2019). Koopman mode expansions between simple invariant solutions. *Journal of Fluid Mechanics*, 879:1–27.

Page, J. and Kerswell, R. R. (2020). Searching turbulence for periodic orbits with dynamic mode decomposition. *Journal of Fluid Mechanics*, 886:A28.

Rowley, C. W. and Dawson, S. T. M. (2017). Model reduction for flow analysis and control. *Ann. Rev. Fluid Mech.*, 49:387–417.

Rowley, C. W., Mezić, I., Bagheri, S., Schlatter, P., and Henningson, D. S. (2009). Spectral analysis of nonlinear flows. *J. Fluid Mech.*, 641:115–127.

Schmid, P. J. (2010). Dynamic mode decomposition of numerical and experimental data. *J. Fluid Mech.*, 656:5–28.

Schmid, P. J., Li, L., Juniper, M. P., and Pust, O. (2010). Applications of the dynamic mode decomposition. *Theor. Comput. Fluid Dyn.*, 25:249–259.

Schneider, T. M., Gibson, J. F., and Burke, J. (2010). Snakes and Ladders: Localized Solutions of Plane Couette Flow. *Phys. Rev. Lett*, 104(1):104501.

Scott, A. C., Chu, F., and McLaughlin, D. W. (1973). The soliton: A new concept in applied science. *Proc. IEEE*, 61(10):1443–1483.

Sharma, A. S., Mezić, I., and McKeon, B. J. (2016). Correspondence between Koopman mode decompositions, resolvent mode decomposition and invariant solutions of the Navier-Stokes equations. *Phys. Rev. Fluids*, 1:032402(R).

Tu, J. H., Rowley, C. W., Luchtenburg, D. M., Brunton, S. L., and Kutz, J. N. (2014). On dynamic mode decomposition: theory and applications. *J. Comput. Dynam.*, 1(2):391–421.

Williams, M. O., Kevrekidis, I. G., and Rowley, C. W. (2015). A data-driven approximation of the Koopman operator: Extending dynamic mode decomposition. *J. Nonlinear Sci.*, 25(6):1307–1346.

Zabusky, N. J. and Kruskal, M. D. (1965). Interaction of “solitons” in a collisionless plasma and the recurrence of initial states. *Phys. Rev. Lett.*, 15:240–243.

Appendix C

A sum-of-squares optimisation method for studying the double pendulum[1]

---

[1] This chapter is a slightly modified version of a paper in preparation with D. Goluskin and G. M. Vasil.

Abstract

We propose a method, exploiting sum-of-squares optimisation of polynomials, to study the behaviour of chaotic trajectories in the double simple pendulum, given stationary initial conditions. We find open subsets of the initial condition space for which the double pendulum is guaranteed not to 'flip' within a given time period. This provides guidance for how similar methods may be applied to more complex systems of ordinary differential equations.

> The study of complex and chaotic dynamical systems using computational methods usually involves direct numerical solution of the governing differential equations. This involves not only the discretisation of time, introducing errors, but also the discretisation of state space. This paper takes an alternative, complementary approach of computationally studying the governing equations by rearranging them into polynomial form and applying polynomial sum-of-squares optimisation.

C.1 Introduction

A chaotic dynamical system is defined by sensitivity to initial conditions, such that a small change at one time leads to a large change at a later time. This defining characteristic means that understanding the behaviour of such systems is hard. Despite knowing exactly the governing ordinary (or partial) differential equations of a chaotic system, any numerical solution of the equations must be treated with caution, since numerical errors will necessarily lead to large errors in the final result. Not only this, but when trying to understand the behaviour of sets of initial conditions, one must discretise the set over a sample of solution trajectories. As the dynamics are chaotic, it is not always clear that other trajectories starting within the set will not diverge drastically from those studied.

For these reasons, when dealing with chaotic systems, it may be useful to study the equations directly rather than individual numerical solutions. For example, in the case of Hamiltonian systems, such as the double pendulum studied herein, it is enlightening to find conserved quantities of the dynamics and consider the foliation of phase space that this causes.

Recent advances in computing power and algorithms mean that it is now possible to computationally study polynomial dynamical systems. There are many methods which require the finding of a function on phase space satisfying certain equality and inequality constraints, for example Lyapunov functions in stability analysis. In looking for such functions, we may restrict ourselves to polynomials; the inequality constraints will then amount to finding one or more non-negative polynomials. In general this is hard, but it is sufficient to find polynomial sums-of-squares (SOS), which is computationally tractable. For an in-depth explanation, see **?**. Multiple software packages are now available both to convert the SOS program into a semidefinite program (SDP), and to solve the SDP. In principle, this can be performed analytically to make proofs of SOS rigorous, but the large number of coefficients to be determined makes this practically impossible for all but the simplest cases.

The method employed in this paper, which can be used for any polynomial dynamical system for which one is interested in the time until which a certain criterion is met, is closely related to the method described in Henrion and Korda (2013).The method works by finding a (polynomial) function, the 'barrier function', increasing along trajectories, which is greater than a certain value on an initial set, but is always less than a certain value on a 'target' set. If such a function can be found, no trajectory starting from the initial set may enter the target set. We call this the barrier function method.

As an example of this method, we study the double pendulum. As a Hamiltonian system with no long-time attractor, the methods using SOS to find bounds mentioned above are not useful. Though the system has two Hamiltonian degrees of freedom, it is very easy to visualise and understand, but the chaotic nature means it is nevertheless an interesting system. Despite the fact it is often used as an example of a chaotic system in introductory texts, it has been the subject of relatively little serious study. Poincaré sections, periodic orbits and Lyapunov exponents were found by Stachowiak and Okada (2006). Through some substitutions and tricks, which can be applied to more complex systems, we are able to transform the governing equations into a polynomial system which enables application of the barrier function method. A fractal pattern has been observed and studied Heyl (2008); Palace and Emmert (2016); Elinson (2013) in diagrams showing the time until the first flip for different initial conditions. The barrier function method then allows us to determine, for finite target times, which regions of this fractal do and do not flip.

The paper proceeds as follows: in section C.2.1, we present the general barrier function method, formulated as a SOS program; in section C.2.2 we derive the polynomial governing equations for the double pendulum system; in section C.2.3 we define the flip time and the problem to be studied; in section C.2.4 we give the full SOS program for this system; in section C.3 we give the results of our calculations; and in section C.4 we discuss these results and possible future applications of the method.

C.2 Problem formulation

C.2.1 Barrier function method

Suppose we have a dynamical system in one variable x,

$$\frac{dx}{dt} = f(x). \tag{C.1}$$

To guarantee that trajectories starting in some initial set given by $g(x) \leq 0$ do not enter a target set $h(x) = 0$ within a time T, it is sufficient to find a function $V(x,t)$ such that

$$\frac{\partial V}{\partial t} + f(x)\frac{\partial V}{\partial x} \geq 0 \quad \text{when} \quad 0 \leq t \leq T, \tag{C.2a}$$

$$V > 0 \quad \text{when} \quad t = 0,\ g(x) \leq 0, \tag{C.2b}$$

$$V \leq 0 \quad \text{when} \quad 0 \leq t \leq T,\ h(x) = 0. \tag{C.2c}$$

The first inequality states that the time derivative of the function moving along a trajectory is positive, and therefore V increases in time. These inequalities are only required to hold over the restricted sets given, rather than all values of x and t (as is the case for polynomial SOS). With the introduction of some auxiliary functions, the inequalities can be converted to inequalities ofver all space by the following method (variously known as the S-procedure or weighted SOS).For example, if σ_1 is a non-negative function and σ_2 is an arbitrary function,

$$-V - \sigma_1(x,t)t(T-t) - \sigma_2(x,t)h(x) \geq 0 \quad \forall x,t \tag{C.3}$$

implies (C.2c). If f, g and h are polynomials then these conditions can be formulated as a sum-of-squares optimisation program.

It is straightforward, if notationally clunky, to extend this method to systems of more than one variable, and to arbitrary semialgebraic initial and target sets. We note also that h could be a function of time, in general.

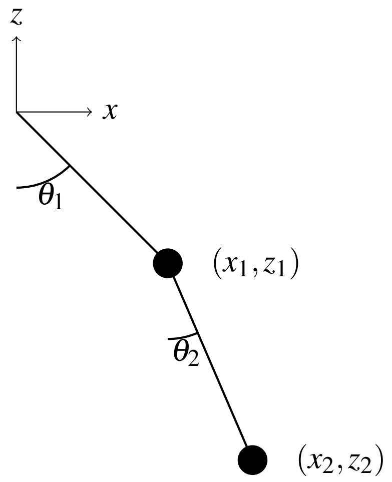

Fig. C.1 The conventions used for the double simple pendulum in this work.

C.2.2 The double pendulum polynomial system

The double simple pendulum, shown in figure C.1, of two equal unit masses, connected by light, frictionless, rigid rods, is described by the Lagrangian

$$\begin{aligned}\mathscr{L} =& \frac{1}{2}\left(\dot{x_1}^2 + \dot{z_1}^2 + \dot{x_2}^2 + \dot{z_2}^2\right) - z_1 - z_2 \\ & - \frac{1}{2}\tau_1\left(x_1^2 + z_1^2 - 1\right) \\ & - \frac{1}{2}\tau_2\left((x_2 - x_1)^2 + (z_2 - z_1)^2 - 1\right).\end{aligned} \tag{C.4}$$

Here, the masses are located at (x_1, z_1) and (x_2, z_2), the dots denote time derivatives, and τ_1 and τ_2 are Langrange multipliers which constrain the length of the rods, but also function as the tension in the rods.

The usual Euler-Lagrange equations Landau and Lifshitz (1969) give

$$\begin{aligned}\ddot{x_1} &= -\tau_1 x_1 + \tau_2(x_2 - x_1), \\ \ddot{x_2} &= -\tau_2(x_2 - x_1), \\ \ddot{z_1} &= -1 - \tau_1 z_1 + \tau_2(z_2 - z_1), \\ \ddot{z_2} &= -1 - \tau_2(z_2 - z_1), \\ 1 &= x_1^2 + z_1^2, \quad 1 = (x_2 - x_1)^2 + (z_2 - z_1)^2.\end{aligned} \tag{C.5}$$

Though the right-hand sides of these equations are polynomial expressions, the equations are second order and so we would have to introduce four velocity variables to apply the barrier function method. The ‘flip condition’ (see section C.2.3) is also difficult to implement in these variables. For these reasons, we choose to make a change of variables to the angles θ_1 and θ_2, as per figure C.1, and their respective angular velocities ω_1 and ω_2. This removes the need for the length constraints. We could have used these variables initially, which would have eliminated the tensions and resulted in more complicated trigonometric expressions, but the present method allows a polynomial formulation. We arrive at a first order system in four dynamical variables and two Lagrange multipliers

$$\begin{aligned}\dot{\theta}_1 &= \omega_1, \qquad \dot{\theta}_2 = \omega_2,\\ \dot{\omega}_1 &= \tau_2 \sin(\theta_2 - \theta_1) - \sin\theta_1,\\ \dot{\omega}_2 &= -\tau_1 \sin(\theta_2 - \theta_1),\end{aligned} \tag{C.6}$$

with two constraints

$$\begin{aligned}0 &= \tau_1 - \cos(\theta_2 - \theta_1)\tau_2 - \omega_1^2 - \cos\theta_1,\\ 0 &= 2\tau_2 - \cos(\theta_2 - \theta_1)\tau_1 - \omega_2^2.\end{aligned} \tag{C.7}$$

Several methods are available for handling trigonometric functions within SOS programs. We make use of the substitutions $c_1 = \cos\theta_1$, $s_1 = \sin\theta_1$, $c_2 = \cos(\theta_2 - \theta_1)$ and $s_2 = \sin(\theta_2 - \theta_1)$. Using the more obvious variables $\cos\theta_2$ and $\sin\theta_2$ would result in polynomials of degree 3. We arrive at a system in six dynamical variables

$$\begin{aligned}&\dot{\omega}_1 = s_2\tau_2 - s_1, \quad \dot{\omega}_2 = -s_2\tau_1,\\ &\dot{c}_1 = -\omega_1 s_1, \quad \dot{s}_1 = \omega_1 c_1,\\ &\dot{c}_2 = -(\omega_2 - \omega_1)s_2, \quad \dot{s}_2 = (\omega_2 - \omega_1)c_2,\end{aligned} \tag{C.8}$$

and we now have four constraints, including the normalisation of the sines and cosines,

$$c_1^2 + s_1^2 = 1, \qquad c_2^2 + s_2^2 = 1, \tag{C.9}$$

$$\tau_1 - c_2\tau_2 - \omega_1^2 - c_1 = 0, \quad 2\tau_2 - c_2\tau_1 - \omega_2^2 = 0. \tag{C.10}$$

The total energy of the system is given by

$$E = 3 - 2c_1 - c_2c_1 + s_2s_1 + \omega_1^2 + \frac{1}{2}\omega_2^2 + c_2\omega_1\omega_2, \tag{C.11}$$

which is a conserved quantity, and can be used to reduce the scope of the problem (see section C.2.4).

C.2.3 Definition of time-to-flip

Various different definitions of when the system ‘flips’ are possible, and it is not obvious which best fits one’s intuition. It seems natural that the minimum energy flip is when $\theta_2 = \pi$ and $\theta_1 = 0$. The requirement that the energy be greater than this gives rise to the clear ‘lens’ shape visible in all figures of the θ_1-θ_2 plane. Heyl (2008) and Elinson (2013) define a flip as when either of the rods becomes vertical, so that $\theta_1 = \pm\pi$ or $\theta_2 = \pm\pi$. This is unappealing for our method as there are two different possibilities which would need to be separately tested against. Palace and Emmert (2016) considered only when $\theta_2 = \pm\pi$, so the outer rod is vertical. This is a clean and computationally efficient definition but leads to ‘flips’ which may be counter intuitive, as large amplitude quasi-periodic swings can briefly satisfy this condition before reversing.

We choose to define a flip as when $\theta_2 - \theta_1 = \pm\pi$, which is easy to implement as $c_2 = -1$ with the trigonometric variables. This does however exclude ‘flips’ where both masses together pass above the pivot. Figure C.2 shows the time-to-flip for stationary initial conditions, as a function of the initial angles. This two dimensional slice through phase space makes it possible to use a brute force method for finding trajectories. Despite this, the figure still needs to be relatively low resolution, and noise is apparent from the chaotic nature of the system. The direct solutions used in figure C.2 were calculated in MATLAB by solving (C.6) and (C.7) using the ode45 solver, with an absolute tolerance of 10^{-10} and a relative tolerance of 10^{-7}.

Any sensible definition of a flip should be symmetric under a reflection of the pendulum in the vertical axis: the inversion $\theta_1 \to -\theta_1$ and $\theta_2 \to -\theta_2$, which is clearly satisfied in figure C.2. In our trigonometric variables, this symmetry corresponds to invariance under $s_1 \to -s_1$, $s_2 \to -s_2$, $\omega_1 \to -\omega_1$, $\omega_2 \to -\omega_2$, with the other variables unchanged. Additionally in figure C.2, there is a distinct diagonal line $\theta_2 - \theta_1 = \pi$ (and its symmetric equivalent) for which the flip condition is instantaneously satisfied at $t = 0$. Immediately above this line, the time-to-flip is very low.

C.2.4 Sum-of-squares program

To implement the barrier function method as described in section C.2.1, with six dynamical variables and four constraints, a large number of additional arbitrary polynomials are required. In the following, $\sigma_{1,\dots,6}$ are polynomials in the dynamical variables plus τ_1, τ_2 and t; $\sigma_{7,\dots,9}$ are polynomials in the dynamical variables only; and $\sigma_{10,\dots,14}$ are polynomials in the dynamical variables plus t.

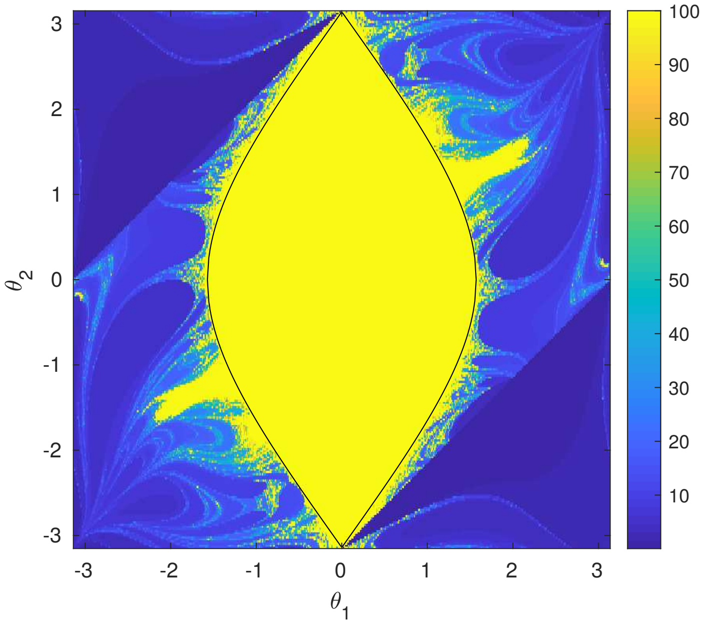

Fig. C.2 Time until first flip (truncated at $t = 100$) for all possible stationary initial conditions. The black curves enclose the region for which flipping is energetically infeasible. Outside this region, a fractal pattern is apparent.

The following expressions are all required to be polynomial sums of squares:

$$\begin{aligned}&\frac{\partial V}{\partial t} + \mathbf{f}\cdot\nabla V - g_1\sigma_1 - g_2\sigma_2 - h_1\sigma_3 - h_2\sigma_4 \\ &\qquad - t(T-t)\sigma_5 - b_E\sigma_6,\end{aligned} \tag{C.12a}$$

$$V|_{t=0} - b_0\sigma_7 - \omega_1^2\sigma_8 - \omega_2^2\sigma_9 - \varepsilon, \tag{C.12b}$$

$$\begin{aligned}&-V - g_1\sigma_{10} - g_2\sigma_{11} \\ &\qquad - t(T-t)\sigma_{12} - b_E\sigma_{13} - (c_2+1)\sigma_{14},\end{aligned} \tag{C.12c}$$

$$\sigma_5, \quad \sigma_6, \quad \sigma_7, \quad \sigma_{12}. \tag{C.12d}$$

Expression (C.12a) enforces V to increase along trajectories of the dynamical system within the time interval $(0,T)$, and incorporates the governing ODEs as well as the necessary constraints. Expression (C.12b) enforces V to be greater than 0 at $t = 0$ when $\omega_1 = \omega_2 = 0$ and $b_0 \geq 0$ (see below). ε is a small constant (10^{-3}) to enforce a strict inequality for (C.12b). Expression (C.12c) enforces V to be less than for equal to 0 when $c_2 = -1$, i.e. the ‘flipped’ state, in the time interval. Since this expression includes the variables c_1, s_1, c_2 and s_2, we must also enforce the normalisation condition here.

The vector $\mathbf{f}$ in (C.12a) is formed of the right hand sides of (C.8), and the operator ∇ represents the first derivative with respect to each of the dynamical variables, so that

$\frac{\partial V}{\partial t} + \mathbf{f} \cdot \nabla V$ is the total derivative of V with respect to t. The constraints (C.9) and (C.10) are imposed by requiring V to increase along trajectories only when $g_1 = g_2 = h_1 = h_2 = 0$, where

$$g_1 = c_1^2 + s_1^2 - 1, \quad g_2 = c_2^2 + s_2^2 - 1, \tag{C.13}$$

and

$$\begin{aligned} h_1 &= \tau_1 - c_2\tau_2 - \omega_1^2 - c_1, \\ h_2 &= 2\tau_2 - c_2\tau_1 - \omega_2^2. \end{aligned} \tag{C.14}$$

Given an upper bound on the energies we are considering, we restrict the scope of the problem by requiring V to decrease only when

$$b_E = E_u - \left(3 - 2c_1 - c_2c_1 + s_2s_1 + \omega_1^2 + \frac{1}{2}\omega_2^2 - \omega_1\omega_2\right) \tag{C.15}$$

is non-negative. This restriction greatly reduces the complexity of the SOS program and means much lower order polynomials are required for the same T. No improvement was found when further enforcing a minimum energy.

The equations so far are invariant under the symmetry action mentioned in section C.2.3. In order to exploit this numerically, we must ensure that the initial region also shares this symmetry. The simplest region to implement, though counter-intuitive when thinking in terms of θ_1 and θ_2, is closed balls in c_1, s_1, c_2, s_2 space, mirrored about the symmetry, giving an indicator function

$$\begin{aligned} b_0 = -\Big(&\big(c_1 - \cos\theta_1^0\big)^2 + \big(s_1 - \sin\theta_1^0\big)^2 \\ &+ \big(c_2 - \cos(\theta_2^0 - \theta_1^0)\big)^2 + \big(s_2 - \sin(\theta_2^0 - \theta_1^0)\big)^2\Big) \\ &\times \Big(\big(c_1 - \cos\theta_1^0\big)^2 + \big(s_1 + \sin\theta_1^0\big)^2 \\ &+ \big(c_2 - \cos(\theta_2^0 - \theta_1^0)\big)^2 + \big(s_2 + \sin(\theta_2^0 - \theta_1^0)\big)^2\Big) \end{aligned} \tag{C.16}$$

These sets manifest as pairs of diagonal ovals in the $\theta_1 - \theta_2$ plane. It can be shown, in an argument analogous to theorem 2 in (**?**), that given a solution V to the SOS program (C.12) which is not invariant under the symmetry transformation, it is possible to find an equivalent one which is. This means that we are able to restrict our problem to consider only V (and $\sigma_{1,\dots,14}$) which are invariant, and so reduce the dimensionality of the problem.

For reasons of numerical conditioning, it was found to be necessary to keep the variables provided to the SOS solver in the range $[-1, 1]$, as has been found by other authors (Goluskin, 2020). This prevents high powers of variables from producing very large values. Clearly c_1, s_1, c_2, and s_2 will automatically satisfy this property. If we consider only those trajectories which start from rest ($\omega_1 = 0$, $\omega_2 = 0$), we must therefore have $E \leq 6$, and by construction, $E \geq 0$. Certainly then, ω_1 and ω_2 must lie within the region with boundary

$$\omega_1^2 + \frac{1}{2}\omega_2^2 + \omega_1\omega_2 = 6. \tag{C.17}$$

By extremising this expression, we find that $|\omega_1| \leq 2\sqrt{3}$ and $|\omega_2| \leq 2\sqrt{6}$. Solving (C.10) for τ_1 and τ_2, we subsequently find $|\tau_1| \leq 50$ and $|\tau_2| \leq 37$. Numerically, we therefore choose to work with the scaled variables $\tilde{\omega}_1 = \frac{\omega_1}{2\sqrt{3}}$, $\tilde{\omega}_2 = \frac{\omega_2}{2\sqrt{6}}$, $\tilde{\tau}_1 = \frac{\tau_1}{50}$ and $\tilde{\tau}_2 = \frac{\tau_2}{37}$. We also use a rescaled time $\tilde{t} = \frac{t}{T}$.

C.3 Results

Initial sets described by balls in $c_1 - s_1 - c_2 - s_2$ space do not obviously lend themselves to a systematic exploration of the $\theta_1 - \theta_2$ plane in which we are interested. We employed the following iterative process to map out the plane:

1. Divide the region $-\pi \leq \theta_1 \leq \pi$, $0 \leq \theta_2 \leq \pi$ into a grid of squares.
2. For each square, using a simple SOS program, find the smallest ball in $c_1 - s_1 - c_2 - s_2$ space which encloses the square.
3. Attempt to guarantee no flips before time T for this ball, using the program given in section C.2.4.
4. If we are unable to guarantee this, subdivide the square into four smaller squares, and repeat from step 2.

This process effectively builds up a quadtree for the entire set of initial conditions.

The programs are implemented in MATLAB, using the YALMIP Löfberg (2004) SOS parser and the Mosek Andersen and Andersen (2000) SDP solver. Each region was run as a separate program. The Mosek solves used 18 Intel Skylake cores, requiring about 60GB of RAM and 8-16 hours of wall time to run per region. It was observed that those regions close to the boundaries between flipping and not flipping required the most Mosek iterations to converge, and so took the longest. Each of the unknown functions to be determined by the program, V and $\sigma_{1,\ldots,14}$, are taken to be polynomials of degree 6 in the state variables multiplied by a polynomial of degree 6 in t. As T is increased and the trajectories become

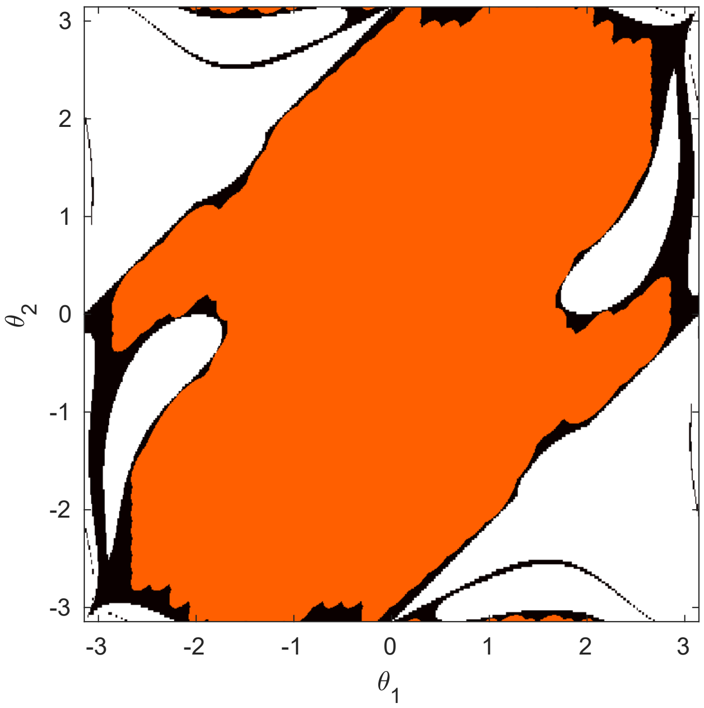

Fig. C.3 Regions guaranteed not to flip before $T = 6$, after two iterations of the grid refinement procedure. Red: guaranteed by barrier function method not to flip. Black: found not to flip by direct numerical solution. White: found to flip by direct numerical solution.

more complex, higher degree polynomials are required to solve the SOS program, but increasing the degree corresponds to increases in the number of unknown coefficients. Both memory usage and computation time scale poorly with the number of coefficients. The number can be approximately halved from 161238 to 81735 by exploiting the symmetry inherent in the system, which means that odd degree terms in the variables s_1, s_2, ω_1 and ω_2 do not appear.

Figure C.3 shows those regions of the stationary initial condition space which we were able to guarantee did not flip before $T = 6$, after three grid refinement iterations. Even on this relatively short time interval, the beginnings of the fractal structure are apparent, with some regions appearing to flip while others do not. Though the regions appear solid from the direct solutions, it is not a priori clear that within the (black) regions which do not flip there are trajectories which do.

Figure C.4 demonstrates this point: here fine filaments are visible which are barely perceptible on figure C.3. At this degree of polynomial, we are able to certify as non-flipping some regions within the broader filament, but not the very fine filament. This is due to the fact that very close to the boundaries of the regions, higher degree polynomials are required

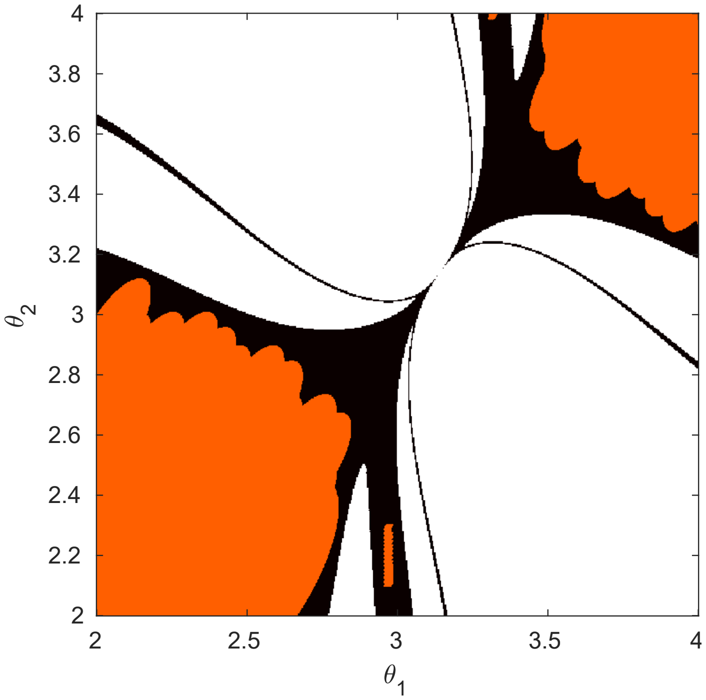

Fig. C.4 Enlargement of region near $\theta_1 = \pi$, $\theta_2 = \pi$, showing the fine filamentation as the fractal begins to develop, visible even at $T = 6$.

to describe trajectories which come very close to flipping but ultimately do not within the finite time window.

C.4 Conclusions

In this work we have performed, to our knowledge, the first application of the barrier function method to a chaotic system. We have been able to guarantee results that were implied by direct solution of the governing equations, namely that specific regions of the initial condition space in the double pendulum system do not ‘flip’ within a certain time. This was computationally very costly, as many individual solutions of the sum-of-squares program were required for the complex shape of the region. In this second degree polynomial system in only 6 variables, it was much more efficient to calculate through brute force a large number of trajectories, even at rather high temporal resolution, than to perform the barrier function method. However, we deliberately constrained our problem to consider only a two-dimensional slice of the initial condition space, so that results could easily be compared against the brute force approach. As the dimensionality of the space one explores increases, brute force methods become prohibitively expensive, as the number of trajectories required increases exponentially. Conversely, it is no more expensive to apply the barrier function method to a 10 dimensional ball than a 2 dimensional one.

Despite the modest results, this study has provided useful insight into the application of SOS methods for dynamical systems. We have introduced some ideas of how to deal with trigonometric functions in such systems, and demonstrated the importance of carefully choosing the variables from which the polynomials are constructed to minimise both the number of variables and the degree of the polynomials.

The field seems still to be a long way from using methods such as the one presented in this paper to analyse physically relevant high-dimensional systems, as more computing power and memory may be needed. Nevertheless, a first order contribution to computation time was found to be the construction of the SDP, which could certainly be optimised.

C.5 Acknowledgments

This work began as a project at the Geophysical Fluid Dynamics program at Woods Hole Oceanographic Institution. The authors wish to thank C. R. Doering, P. J. Morrison and G. Fantuzzi for helpful comments and support.

C.6 References

Andersen, E. D. and Andersen, K. D. (2000). *The Mosek Interior Point Optimizer for Linear Programming: An Implementation of the Homogeneous Algorithm*, pages 197–232. Springer US, Boston, MA.

Elinson, J. (2013). Flip-over threshold for the double pendulum.

Goluskin, D. (2020). Bounding extrema over global attractors using polynomial optimisation. *Nonlinearity*.

Henrion, D. and Korda, M. (2013). Convex computation of the region of attraction of polynomial control systems. *IEEE Transactions on Automatic Control*, 59(2):297–312.

Heyl, J. S. (2008). The double pendulum fractal.

Landau, L. and Lifshitz, E. (1969). *Mechanics*. Course of theoretical physics. Pergamon Press.

Löfberg, J. (2004). Yalmip: A toolbox for modeling and optimization in matlab. In *Proceedings of the CACSD Conference*, volume 3. Taipei, Taiwan.

Palace, M. and Emmert, J. (2016). Hidden fractals in the dynamics of the compound double pendulum.

Stachowiak, T. and Okada, T. (2006). A numerical analysis of chaos in the double pendulum. *Chaos, Solitons & Fractals*, 29(2):417–422.